

A 3.3 mm Survey of Circumstellar Material in ρ Ophiuchus

Mr David Hogg

Submitted by Mr David Hogg to the University of Exeter as a thesis for the degree of Master of Philosophy in Physics, March, 2009.

This thesis is available for Library use on the understanding that it is copyright material and that no quotation from the thesis may be published without proper acknowledgement.

I certify that all material in this thesis which is not my own work has been identified and that no material has previously been submitted and approved for the award of a degree by this or any other University.

Signed:
Mr David Hogg

Date:

Abstract

Millimetre observations of pre-main sequence stars probe the cold dust in the outer regions of the forming star system. It is in these outer regions that planets are thought to form out of the gas and dust within the circumstellar disk. Therefore, by observing young stellar objects at millimetre wavelengths we can determine the characteristics of circumstellar material, and hence, we can infer the possibility of a system forming planets.

In order to characterise the circumstellar environment of pre-main sequence stars, a 3.3 mm survey of continuum dust emission was performed using the OVRO interferometer array. A sample of targets in the nearby star forming region ρ Ophiuchus were selected to encompass the entire range of pre-main sequence evolution, from starless clumps to Class III T Tauri stars. These data were then used to constrain properties of the circumstellar material in these young systems, in particular the dust opacity index, β , and the mass of the material. The value of β is used to study whether grain growth of the dust is occurring in these systems, which is a key stage in some planet formation models. Calculating the mass of the system can indicate whether enough circumstellar material is present to form planets. We also combine these new millimeter observations with literature data to create spectral energy distributions (SEDs), which are then fit in order to determine a best-fit model of the system using the models of Robitaille et al. (2007).

We find that the dust opacity index evolves from a value similar to that of the ISM for the starless clumps ~ 2.3 , to one closer to ~ 0.2 for the Class II objects. This low β could be accounted for by the inclusion of larger grains within the disk, indicating the possibility of grain growth through the evolutionary stages of a young system. For the Class I and Class II sources we find similar trends in β to those found in Andrews & Williams (2007a). An estimate of circumstellar mass assuming a constant dust opacity index was made using the flux of each source. Carrying out this calculation yielded a mean mass of $0.033 M_{\odot}$, with almost 50% of the sources having a mass $> 0.01 M_{\odot}$. A more in depth estimate of mass was also performed using the value newly calculated value of the dust opacity index. The mass estimates indicated many of the sources observed by this survey have the mass of dust available in the system to form planets.

Contents

1	Introduction	13
2	Star Formation	15
2.1	Molecular Clouds	15
2.2	Cloud Core Collapse	16
2.3	Pre-Main Sequence Evolution	17
2.3.1	Theoretical Models	17
2.3.2	Observational Classes	18
2.3.3	Binary Star Formation	21
2.3.4	Low Mass Star and Brown Dwarf Formation	24
2.4	Circumstellar Material	24
2.4.1	Disk Emission	25
2.4.2	Disk Properties	26
2.4.3	Disk Dissipation	27
3	Submm/mm Observations	29
3.1	Atmospheric Windows	29
3.2	Submm/mm Telescopes	29
3.2.1	Single Dish	30
3.2.2	Interferometry	31
3.3	Resolution Limits	34
3.4	Noise & Sensitivity	34
4	Sample & Observations	37
4.1	Ophiuchus	37
4.2	Previous Surveys	37
4.2.1	Non Submm/mm Surveys	37
4.2.2	Submm/mm Surveys	39
4.3	OVRO Sample	40
4.4	OVRO Observations	44
5	Data Reduction	45
5.1	Editing and Calibration	45

5.1.1	Baseline Correcting	45
5.1.2	Data Inspection and Flagging	46
5.1.3	Bandpass Calibration	46
5.1.4	Phase Calibration	47
5.1.5	Flux Calibration	48
5.2	Mapping	48
5.2.1	Fourier Inversion	48
5.2.2	Deconvolution	49
6	OVRO 3mm Fluxes & Upper Limits	51
6.1	Starless	52
6.1.1	A-MM1, A-MM2, A-MM3	53
6.1.2	A-MM7	54
6.1.3	Non-Detected Sources	54
6.2	Class 0	54
6.2.1	IRAS16293	54
6.2.2	LFAM5	56
6.3	Class I	56
6.3.1	CRBR12	57
6.3.2	EL21	58
6.3.3	GY91	58
6.3.4	IRS43	58
6.3.5	L1689S	59
6.3.6	L1709B	59
6.3.7	LFAM26	59
6.3.8	LFAM30	59
6.3.9	YLW2	59
6.3.10	YLW46A	60
6.4	Flat Spectrum	60
6.4.1	L1719B	61
6.4.2	LFAM1	61
6.4.3	Non-Detected Sources	61
6.5	Class II	62
6.5.1	AS205	62
6.5.2	DOAR25	64
6.5.3	DOAR44	64
6.5.4	EL24	64
6.5.5	EL27	64
6.5.6	Flying Saucer	65
6.5.7	GSS26	65
6.5.8	SR21	65
6.5.9	SR4	65

6.5.10	WAOPH6	66
6.5.11	YLW58	66
6.6	Class III	66
6.7	Unknown Class	66
7	Data Analysis	68
7.1	Calculating Dust Opacity	68
7.1.1	Starless	71
7.1.2	Class 0	72
7.1.3	Class I	73
7.1.4	Flat Spectrum	76
7.1.5	Class II	77
7.2	Calculating Dust Masses	80
7.2.1	Starless	82
7.2.2	Class 0	83
7.2.3	Class I	84
7.2.4	Class FS	84
7.2.5	Class II	85
7.2.6	Class III	85
7.3	Comparison with Other Studies	86
8	SED Fitting	87
8.1	Class 0	88
8.1.1	IRAS16293	88
8.1.2	LFAM5	89
8.2	Class I	89
8.2.1	CRBR12	91
8.2.2	EL21	92
8.2.3	GY91	92
8.2.4	IRS43	93
8.2.5	L1689S	94
8.2.6	L1709B	94
8.2.7	LFAM26	94
8.2.8	LFAM30	94
8.2.9	YLW2	94
8.2.10	YLW46A	95
8.3	Flat Spectrum	95
8.3.1	GY11	95
8.3.2	L1719B	95
8.3.3	LFAM1	96
8.3.4	RNO91	97
8.3.5	SR24	97

8.4	Class II	98
8.4.1	AS205	98
8.4.2	DOAR25	98
8.4.3	DOAR44	98
8.4.4	EL24	99
8.4.5	EL27	100
8.4.6	Flying Saucer	101
8.4.7	GSS26	102
8.4.8	SR21	103
8.4.9	SR4	103
8.4.10	WAOPH6	103
8.4.11	YLW58	103
8.5	Class III	104
8.5.1	GY10	104
8.5.2	GY12	105
8.5.3	GY306	105
8.5.4	ISO-Oph 26	105
9	Conclusions	106
9.1	Detections and Fluxes	106
9.2	Dust Opacity Index	107
9.3	Dust Mass	108
9.4	SED Fitting	109
9.5	Further work	109
A	Calibration and Analysis Scripts	112
A.1	Data Reduction Script	112
A.2	Data Analysis Script	113
	Appendices	112
B	Best Fit SED Parameters and Literature data	114
B.1	Starless	114
B.2	Class 0	116
B.3	Class I	119
B.4	Flat Spectrum	122
B.5	Class II	125
B.6	Class III	130

List of Figures

2.1	Schematic diagram and SED of the evolution of a Class 0 star.	19
2.2	Schematic diagram and SED of a Class I star.	20
2.3	Schematic diagram and SED of a Class II star.	21
2.4	Schematic diagram and SED of a Class III star.	22
2.5	Schematic diagram of a T Tauri star including the emission regions.	25
3.1	The atmospheric transmission between 0 GHz and 1000 GHz, which corresponds to a wavelength range of 30 cm to 300 μ m, at Chajnantor in Chile the site of ALMA.	30
3.2	The beam pattern of a circular aperture is shown as a 2-dimensional cross-section.	31
3.3	A two element interferometric system.	32
3.4	The diffraction patterns of both the individual elements of an interferometer and the combined fringe pattern	33
4.1	Optical and millimetre images of the ρ Ophiuchus molecular cloud complex.	38
4.2	Histograms of the key properties of the sample.	40
5.1	Flow diagram charting the steps made in getting the received visibilities into a map of the source brightness.	46
5.2	Two plots of the $u-v$ data showing difference between good uncalibrated data and bad uncalibrated data.	47
5.3	Two plots of the $u-v$ data showing fully calibrated data.	48
5.4	Example of the products of the three stages of taking calibrated $u-v$ data into making a map of a source.	50
6.1	Left: The detection frequency of the survey Right: The mean fluxes throughout the evolutionary classes.	52
6.2	Maps of the starless sources.	53
6.3	Maps of the Class 0 sources.	55
6.4	Maps of the Class I sources, from top left CRBR12, EL21, GY91, IRS43, L1689s and L1709b.	57
6.5	Maps of the Class I sources, from top left LFAM26 LFAM30, YLW2, and YLW46.	58
6.6	Maps of the Flat Spectrum sources, left is L1719B and right is LFAM1.	60

6.7	Maps of the class II sources, from top left AS205, DoAr25, DoAr44, EL24, EL27 and Flying Saucer.	62
6.8	Maps of the class II sources, from top left GSS26, SR21, SR4, WAOph6 and YLW58.	63
7.1	Results incorporating the OVRO data to show how dust opacity index, β , changes across the evolutionary stages.	69
7.2	Cumulative distributions plots of the β value, both including and excluding the upper limits.	70
7.3	The result of the Kolmogorov-Smirnov test to determine whether the Class I sources and the Class II sources could be drawn from the same base distribution.	71
7.4	Top Left: Submm/mm SED of the source IRAS16293A. Top Right: Submm/mm SED of the source IRAS16293B. Bottom: Submm/mm SED of the source LFAM5.	73
7.5	Submm/mm SEDs of the class I sources, from top left from top left CRBR12, EL21, GY91 and IRS43.	74
7.6	Submm/mm SEDs of the Class I sources, from top left L1689S, L1709b, LFAM26, LFAM30, YLW2, and YLW46.	75
7.7	Submm/mm SED of the Flat Spectrum source LFAM1.	76
7.8	Submm/mm SEDs of the class II sources, from top left AS205, DoAr25, DoAr44, EL24 and EL27.	78
7.9	Submm/mm SEDs of the class II sources, from top left GSS26, SR21, SR4, WAOph6 and YLW58.	79
7.10	Left: Results incorporating the OVRO data to show how dust mass changes across the evolutionary stages, when β is assumed to be 1. Right: Results incorporating the OVRO data to show how dust mass changes across the evolutionary stages, when M_d is calculated using the β value from this survey.	81
7.11	Cumulative distributions plots of dust mass, both including and excluding the upper limits.	82
7.12	The result of the Kolmogorov-Smirnov test to determine whether the Class I sources and the Class II sources could be drawn from the same base distribution.	83
8.1	Left: The best fit SEDs including the 3.3 mm point for the Class 0 sources. Right: The best fit SEDs not including the 3.3 mm point for the Class 0 sources. Top: IRAS16293, Bottom: LFAM5.	89
8.2	Left: The best fit SEDs including the 3.3 mm point for the Class I sources. Right: The best fit SEDs not including the 3.3 mm point for the Class I sources. Top: CRBR12, Middle: EL21, Bottom: GY91.	90

8.3	Left: The best fit SEDs including the 3.3 mm point for the Class I sources. Right: The best fit SEDs not including the 3.3 mm point for the Class I sources. Top: IRS43, Middle: L1689S, Bottom: L1709B.	91
8.4	Left: The best fit SEDs including the 3.3 mm point for the Class I sources. Right: The best fit SEDs not including the 3.3 mm point for the Class I sources. Top: LFAM26, Bottom: LFAM30.	92
8.5	Left: The best fit SEDs including the 3.3 mm point for the Class I sources. Right: The best fit SEDs not including the 3.3 mm point for the Class I sources. Top: YLW2, Bottom: YLW46A.	93
8.6	Left: The best fit SEDs including the 3.3 mm point for the Class FS sources. Right: The best fit SEDs not including the 3.3 mm point for the Flat Spectrum sources. Top: GY11, Middle: L1719, Bottom: LFAM1.	96
8.7	Left: The best fit SEDs including the 3.3 mm point for the Class FS sources. Right: The best fit SEDs not including the 3.3 mm point for the Flat Spectrum sources. Top: RNO91, Bottom: SR24.	97
8.8	Left: The best fit SEDs including the 3.3 mm point for the Class II sources. Right: The best fit SEDs not including the 3.3 mm point for the Class II sources. Top: AS205, Middle: DOAR25, Bottom: DOAR44.	99
8.9	Left: The best fit SEDs including the 3.3 mm point for the Class II sources. Right: The best fit SEDs not including the 3.3 mm point for the Class II sources. Top: EL24, Middle: EL27, Bottom: Flying Saucer.	100
8.10	Left: The best fit SEDs including the 3.3 mm point for the Class II sources. Right: The best fit SEDs not including the 3.3 mm point for the Class II sources. Top: GSS26, Middle: SR21, Bottom: SR4.	101
8.11	Left: The best fit SEDs including the 3.3 mm point for the Class II sources. Right: The best fit SEDs not including the 3.3 mm point for the Class II sources. Top: WAOph6, Bottom: YLW58.	102
8.12	The best fit SEDs of the Class III sources. Top left: GY10, top right: GY12, bottom left: GY306 and bottom right: ISO-Oph 26. GY29 is not included as none of the models fitted the data.	104
B.1	The best fit SED's associated parameters of the Class 0 sources.	116
B.2	The best fit SED's associated parameters of the Class I sources, from top CRBR12, EL21, GY91, IRS43, L1689 and LFAM26.	119
B.3	The best fit SED's associated parameters of the Flat Spectrum sources GY11, L1719, LFAM1 and RNO91.	122
B.4	The best fit SED's associated parameters of the class II sources, from top DOAR25, DOAR44, EL24, EL27, Flying Saucer and GSS26.	125
B.5	The best fit SED's associated parameters of the class II sources, from top SR21, SR4, WAOph6 and YLW58.	126
B.6	The best fit SED's associated parameters of the class III sources, from top left GY10, GY12, GY306 and ISO-Oph 26.	130

List of Tables

3.1	Resolution limits at Submm/mm observatories.	35
3.2	Sensitivity limits at Submm/mm observatories.	36
4.1	Table presenting the basic properties of the sample.	41
6.1	Table containing the recovered fluxes and upper limits for the starless objects.	53
6.2	Table containing the recovered fluxes for the Class 0 objects.	54
6.3	Table containing the recovered fluxes for the Class I objects.	56
6.4	Table containing the recovered fluxes and upper limits for the Class FS objects.	60
6.5	Table containing the recovered fluxes for the Class II objects.	63
6.6	Table containing the 3σ flux upper limits for the Class III objects.	66
6.7	Table containing the 3σ flux upper limits for the unknown class objects. . .	67
7.1	Table containing the calculated value and uncertainty of β for the starless objects	72
7.2	Table containing the calculated value and uncertainty of β for the Class 0 objects	72
7.3	Table containing the calculated value and uncertainty of β for the Class I objects	74
7.4	Table containing the calculated value and uncertainty of β for the Class FS objects	76
7.5	Table containing the calculated value and uncertainty of β for the Class II objects	77
7.6	Table containing the dust masses from the standard $\beta = 1$ calculations and the dust masses calculate using each sources β value for the starless objects.	83
7.7	Table containing the dust masses from the standard $\beta = 1$ calculations and the dust masses calculate using each sources β value for the Class 0 objects.	84
7.8	Table containing the dust masses from the standard $\beta = 1$ calculations and the dust masses calculate using each sources β value for the Class I objects.	84
7.9	Table containing the dust masses from the standard $\beta = 1$ calculations and the dust masses calculate using each sources β value for the Flat Spectrum objects.	85

7.10	Table containing the dust masses from the standard $\beta = 1$ calculations and the dust masses calculate using each sources β value for the Class II objects.	85
7.11	Table containing the dust masses from the standard $\beta = 1$ calculations for the Class III objects.	86
B.1	Table containing the literature data for the starless core objects.	115
B.2	Table containing the literature data for observations at $\leq 125 \mu\text{m}$ used to build the SEDs for the Class 0 objects.	117
B.3	Table containing the literature data for observations at $\geq 125 \mu\text{m}$ used to build the SEDs for the Class 0 objects.	118
B.4	Table containing the literature data for observations at $\leq 14.3 \mu\text{m}$ used to build the SEDs for the Class I objects.	120
B.5	Table containing the literature data for observations at $> 14.3 \mu\text{m}$ used to build the SEDs for the Class I objects.	121
B.6	Table containing the literature data for observations at $\leq 8 \mu\text{m}$ used to build the SEDs for the Flat Spectrum objects.	123
B.7	Table containing the literature data for the observations between $10 \mu\text{m}$ and $100 \mu\text{m}$ used to build the SEDs for the Flat Spectrum sources.	124
B.8	Table containing the literature data for the observations at $\leq 2.2 \mu\text{m}$ used to build the SEDs for the Class II objects.	127
B.9	Table containing the literature data for the observations between $3.6 \mu\text{m}$ and $14.3 \mu\text{m}$ used to build the SEDs for the Class II objects.	128
B.10	Table containing the literature data for the observations at $\geq 24 \mu\text{m}$ used to build the SEDs for the Class II objects.	129
B.11	Table containing the literature data used to build the SEDs for the Class III objects.	131

Acknowledgements

To begin with I feel I should thank my parents, for standing by every decision I have ever made and making me feel like giving up on a PhD doesn't necessarily mean I'm second best. I also would like to thank the support systems in place at Exeter university for helping me get through what was a difficult time. It was not an easy decision to change from a PhD to an MPhil but thanks to this support I was able to make an informed decision about my future and from that decision came this thesis. I would also like to thank the staff and fellow PhD students in the department for their advice during the decision period, especially Tracey Hill and Nathan Mayne.

As for the research and writing the thesis itself, I would like to thank my supervisor Jenny Patience for not getting too upset whenever I missed a deadline and also for driving me on to get it finished even when I'd lost faith in my ability to get it done. I know she worked tirelessly behind the scenes to give me the best possible opportunities available to a PhD student in this country. Although I was unable to make full use of them to complete a PhD I know how important and career changing they could have been if I had finished. One of those opportunities was the CARMA summer school, which is where I picked up many of skills necessary to complete this thesis. I would also like to thank Rob de Rosa and Lee Summers for their help in proof reading.

Finally, I would like to thank the STFC and lately the University of Exeter itself for providing funding for me to continue doing this work. Without the additional funding given to me by the university to complete I don't think I would have been able to submit this thesis.

Thanks.

David Hogg
Exeter, Devon, U.K.
30th March 2009

Chapter 1

Introduction

The early stages of star and planet formation remain shrouded in mystery; from our inability to create pre-main sequence models that match the observations to how sub-micron sized particles grow to a sufficient size to form planets. In order to probe these early stages of stellar and planet formation, multi-wavelength observations are required to determine the key properties of a forming star system; i.e. mass of the star and mass of circumstellar gas and dust. This thesis focuses on the cold circumstellar dust around a forming star, and what the properties of this dust can reveal about star and planet formation.

Using the OVRO interferometer array in California a 3.3 mm survey of young stellar objects in the ρ Ophiuchus molecular cloud was performed. This survey was the first millimetre study to probe the full range of pre-main sequence evolution from starless condensations of dust and gas to what are known as Class III objects, those objects nearing the main sequence. The 3.3 mm data are sensitive to the cold dust in the outer disk and envelope of a forming star system. These observations are used to place constraints on the opacity index of the dust in the system, a probe of possible grain growth, and the total mass of the circumstellar material, a diagnostic of whether planets can form. Finally by combining these long wavelength data with shorter wavelength literature data it is possible to fit model spectral energy distributions to the data. Fitting a model can be used to almost completely constrain the properties of the source; from stellar mass to disk radii.

This thesis is organised as follows: Chapter 2 introduces the background theory of star and planet formation and its associated physics. Chapter 3 describes how millimetre telescopes work and in particular the differences between interferometric and single dish observations. Chapter 4 introduces the ρ Ophiuchus molecular cloud and describes other studies of the region. Chapter 4 also introduces the sample of young stellar objects chosen and also give details of the observations. Chapter 5 explains the steps taken in turning the raw interferometric data into calibrated maps of the source brightness. Chapter 6 presents the 3.3 mm fluxes and upper limits derived for each source from its corresponding source brightness map. Chapter 6 also contains more detailed notes on the individual objects in the survey. Chapter 7 contains the data analysis, including calculating the dust opacity

index and the total mass of the circumstellar material using submm/mm literature data and the new 3.3 mm data. Finally in Chapter 8 SED fitting is performed using shorter wavelength literature data to compliment this surveys 3.3 mm data.

Chapter 2

Star Formation

Star formation is a vital process in the evolution of the universe. Stars impact many fundamental properties of a galaxy ranging from chemical enrichment to the formation of planetary systems. Stars produce the metal elements ($Z > 3$) which form the basis of the chemistry of the galaxy. These metal elements in the region surrounding a forming star form the cores of planets in the system.

Star formation proceeds in several stages from the gravitational collapse of molecular clouds culminating in the formation of a young star. Understanding the stages of star formation not only allows us to probe how our own solar system formed but also allows us to predict how other star-planet systems form. This section describes the key processes of star formation from the collapse of a molecular cloud through the infall and outflow of envelope material the subsequent clearing of the envelope and formation of a disk and finally the evolution and dissipation of the disk.

2.1 Molecular Clouds

Stars form in regions of the galaxy called molecular clouds. Molecular clouds are large, irregular and dense regions of molecular hydrogen. This molecular hydrogen is predominantly found in two types of cloud; giant molecular clouds (GMCs) and dark clouds.

GMCs are the largest cohesive objects in the galaxy and contain up to $10^6 M_\odot$ of gas e.g. Orion has a mass $\sim 10^5 M_\odot$ (Genzel & Stutzki 1989). These GMCs are found extensively in both our own galaxy and other galaxies e.g. M31 (Lada et al. 1988). In our own galaxy GMCs are found along the spiral arms (Georgelin & Georgelin 1976).

GMCs are thought to form by one of two methods: large scale gravitational instabilities (Balbus & Cowie 1985) or the coalescence of smaller clumps of molecular hydrogen (Field & Saslaw 1965). These clumps of molecular hydrogen are believed to form when a spiral arm of the galaxy passes through the background interstellar medium consisting mainly of atomic hydrogen. The resultant shock instantaneously cools and compresses the gas (Dobbs et al. 2006). This results in large clumps of turbulent molecular hydrogen which come together along the spiral arms to form GMCs.

Once formed, GMCs are observationally associated with massive stars. Massive

stars have a spectral class of O or B and are greater than $10M_{\odot}$ in mass. These stars have very short lifetimes (Schaller et al. 1992), which means that they trace regions of on-going or very recent star formation. When massive stars form within GMCs they are so luminous that their UV/X-ray flux ionises the surrounding material. The associated UV/X-ray flux of these so-called HII regions results in a radiation pressure which also blows out a fraction of the dust within the cloud. This extensive stellar feedback means that GMCs are transient regions with lifetimes of $\sim 10^6$ yrs (Elmegreen 2000), which decay as the stellar UV/X-ray flux erodes the cloud, e.g. the erosion of the Horsehead Nebula (Abergel et al. 2003).

GMCs are not the sole location of star formation. Dark clouds are smaller regions of molecular hydrogen where stars are formed. These dark clouds are similar in structure to GMCs, in as much as they appear irregular and turbulent, however they only contain around $10^4 M_{\odot}$ of gas (Cohen & Kuhl 1979). In addition, dark clouds do not form massive stars (Cohen & Kuhl 1979). With no massive stars in dark clouds there is a much lower UV/X-ray flux and therefore a lower radiation pressure to blow the dust within the clouds away. Higher extinction results from dust remaining in the region which conceals some of the on-going star formation at optical wavelengths. A well known example of a dark cloud is the ρ Ophiuchus complex.

2.2 Cloud Core Collapse

Stars form within clouds of molecular hydrogen when small over-densities collapse under gravity to form a starless clump. The over density must be massive enough such that the gravitational collapse can overcome the increased repulsive pressure forces due to thermal energy produced during the collapse. This basic treatment of collapse was first formulated by Jeans (1902) and was termed gravitational instability; it did not include magnetic flux, turbulence or angular momentum. Jeans considered density perturbations in an initially uniform medium which collapse gravitationally against pressure. The critical mass a clump must have in order to undergo this form of collapse is called the Jeans mass (M_J). The Jeans mass can be derived starting from the virial theorem and assuming the cloud is of uniform density and is spherically symmetric. Gravity must dominate the thermal energy, i.e. from the virial theorem $2U < \Omega$, where U is the internal energy and Ω the gravitational potential energy. The Jeans mass is then

$$M_J = \frac{5kT}{G\mu m_H} \frac{3}{4\pi\rho_0}, \quad (2.1)$$

where k is the Boltzman constant, T is the temperature of the cloud, G is the gravitational constant, μ is the mean molecular weight, m_H is the weight of atomic hydrogen and ρ_0 is the cloud density. A high temperature cloud needs to be much more massive or have a high density in order to collapse due to the increased thermal motions of the particles. Therefore, Jeans collapse will only occur in the colder, denser regions of space.

The Jeans formalism deals with collapsing clumps of material, but was not put

into the perspective of star formation until the work of Hayashi (1966). The Hayashi model deals with the collapse, under gravity, against the thermal pressure forces and once collapse begins it proceeds on the gravitational free-fall timescale. The gravitational free-fall timescale, t_{ff} , is derived by considering the time it takes for a point mass to fall from the edge of the cloud,

$$t_{\text{ff}} = \frac{1}{4} \sqrt{\frac{3\pi}{2G\rho}}, \quad (2.2)$$

where G is the gravitational constant and ρ is the cloud density. The time it takes a star to collapse from a clump to a centrally condensed core is determined by the density of the cloud, a more dense cloud collapses faster than a sparse cloud.

2.3 Pre-Main Sequence Evolution

Both the Jeans and Hayashi treatment do not account for the turbulence or magnetic fields that are present within molecular clouds. GMCs are known to be turbulent environments (Larson 1981), possibly due to large scale gravitational interactions and stellar feedback. The stellar feedback aspect of turbulence explains why the larger GMCs often appear more turbulent than the dark clouds (Larson 1981). Turbulence is an additional force gravity must counteract, therefore it acts to retard the collapse of a clump to form a star. Since the collapse requires high density regions and turbulence constantly mixes the material in a cloud. For example, any high density region which begins to collapse could be wiped out by turbulence before it has a chance to form a core. Another aspect of the molecular clouds are their magnetic fields, on the order of \sim tens of micro gauss (Kazes et al. 1987). The magnetic fields of the cloud inhibit the collapse of charged particles as the charged particles can only flow along field lines and perpendicular to them. This slowing of collapse due to magnetic fields is the basis for the standard model of single star formation, that of Shu (1977) and Shu et al. (1987).

2.3.1 Theoretical Models

The Shu et al. (1987) model begins with the assumption that GMCs are long-lived and relatively static. In this model the dominant process of star formation is called ambipolar diffusion. Ambipolar diffusion means the collapse is retarded by magnetic fields within the cloud which only allow neutral particles to diffuse through field lines. This process is very slow with a timescale of ~ 10 Myrs (Mouschovias 1991), and is the basis for slow star formation models. The slow collapse of neutral particles will eventually form a core with enough mass such that gravity will overcome initial forces which resist collapse. During the collapse, the gravitational potential energy of the infalling cloud is converted into kinetic/thermal energy. This heating, together with the increased density within the core, causes nuclear fusion to occur within the core.

Current evidence suggests that the Shu model is not the dominant process by which

stars form. GMCs are not long-lived and static in fact they are not stable over the 10^7 yrs required to form a star by ambipolar diffusion (Elmegreen 2000). Single systems in the early stages of collapse have been observed to have gas infall velocities larger than that predicted by the Shu model (Lee et al. 2001). The inability of the Shu model to form multiple star systems is another problem for the model as multiple systems are widespread. Within our local neighbourhood, Duquennoy & Mayor (1991) found the binary fraction of nearby solar type stars to be $\sim 60\%$.

More recent models of star formation attempt to account for the timescale and binarity issues encountered by the Shu model. Star formation needs to occur over a timescale < 10 Myrs since GMCs are now known to be highly turbulent and not static like the assumption by the Shu model. One rapid star formation model (hereafter the BP model) was developed with MHD simulations by Ballesteros-Paredes et al. (1999). The BP model of star formation proposed that collapse in regions around molecular hydrogen clumps can occur on far shorter timescale than that of the Shu model due to external pressures driven by inter-cloud turbulence. The inter-cloud medium consists of streams of atomic hydrogen, which can impact the denser molecular regions causing collapse to occur rapidly, $t \leq 3$ Myr. This decreased formation time results in the stellar feedback affecting the cloud at a much earlier epoch, dissipating the dust and returning the region to the atomic hydrogen background over time.

2.3.2 Observational Classes

Angular momentum plays a key role in the formation of a star. The protostellar environment is not simply dominated by the gravitational forces causing the cloud to collapse. Molecular clouds have been shown to be rotating and therefore possess angular momentum (Goodman et al. 1993), which affects the infall of the gas. The angular momentum must be conserved. However, the material around the protostellar core needs to accrete onto the core in order to increase its mass. This is achieved by the cloud collapsing into a disk-like structure (Terebey et al. 1984). The disk structure facilitates the removal of angular momentum of the gas and dust through viscous interactions. Removing the angular momentum of the disk material allows it to fall onto the star in an accretion column. Surrounding the disk during the early stages of formation is an envelope of gas and dust which can replenish the disk material.

The pre-main sequence evolution of low mass stars is categorised observationally as five stages. These stages were named Class I to Class III by Lada & Wilking (1984), with Class 0 added later by Andre et al. (1993) and Flat Spectrum defined between Classes I and II. The classes are based on the spectral energy distribution (SED) and specifically the spectral index, α , in the infrared (IR) between 4.8 and $20 \mu\text{m}$. The SED of an object shows how the flux received from the object varies with wavelengths. The spectral index is defined as

$$\alpha = \frac{d \log F_{\lambda} \lambda}{d \log \lambda}, \quad (2.3)$$

where λ is the wavelength of the radiation and F_λ is the flux of radiation at that wavelength (Lada 1987). An SED can be used to show whether a source shows excess emission above the photospheric emission of the central star. The wavelength that this excess occurs at can indicate where in the system the excess emission is from, for example a near IR excess is indicative of a heated inner disk. From the observed radiation the classes are assigned properties (Feigelson & Montmerle 1999).

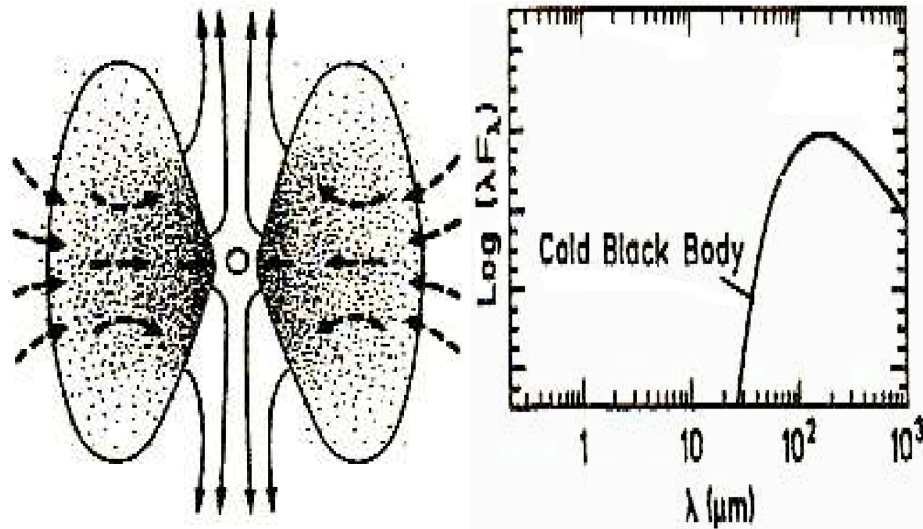


Figure 2.1: Schematic diagram and SED of the evolution of a Class 0 star. Class 0 sources are completely surrounded by high density envelope gas with powerful outflow jets. The material closest to the star forms a disk structure. Class 0 SEDs are blackbodies at the temperature of the dust (~ 20 K) (Glass 1999)

A Class 0 protostar, Fig. 2.1 has a hot, dense core, due to the initial collapse of the cloud (Andre et al. 1993). The core formed accretes more of the gas and dust from the original cloud and continues to collapse causing more heating. The Class 0 sources are believed to be $\sim 10^4$ yr old (Feigelson & Montmerle 1999). During the Class 0 stage the gas and dust forms a disk like structure due to angular momentum conservation. There is also a large, cold envelope present. The star is so deeply embedded within its pre-natal envelope that it is invisible at optical and near to mid infrared wavelengths. The cold ($T \sim 20$ K) envelope emits at submillimetre (submm) and millimetre (mm) wavelengths and often appears extended. The SED is characterised by a blackbody at the temperature of the dust. The Class 0 stage is also known to have large molecular jet-like outflows (Snell et al. 1980).

The protostar continues to gain mass from the infalling material and reaches the Class I stage, Fig. 2.2 ($t \sim 10^5$ yr) (Lada & Wilking 1984). During this stage the core gets hotter and denser while the outer envelope begins to disappear due to a combination of infall and the powerful molecular outflows. The infalling material becomes optically thick within the disk structure. This results in a protostar surrounded by a smaller envelope of gas and dust, than in the Class 0 stage, and in addition the system now also contains a

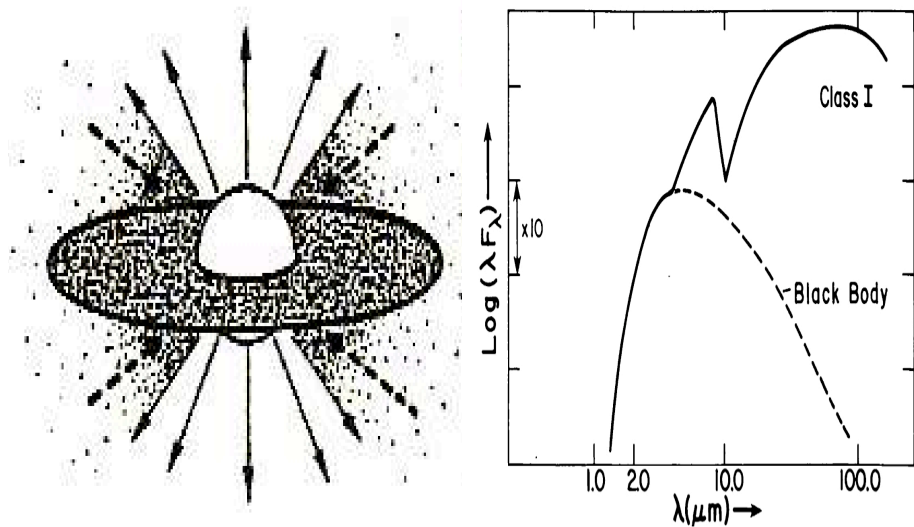


Figure 2.2: Schematic diagram and SED of a Class I star. Class I sources have the beginnings of a disk but most of the gas is still in the envelope. Class I SEDs show large IR excesses from inner dust as well as very high submm excesses from the cold dust in the outer regions of the disk. Both these excesses are clearly above the expected black body emission from the protostar (Glass 1999; Lada 1987).

disk. This phase is categorised observationally as having $0 < \alpha \leq 3$. The SEDs of Class I sources still have large submm excesses, however they are less deeply embedded in their envelope. Due to the formation of a disk with removal of some of the obscuring envelope, the SED also shows a large infrared excess. This IR excess arises from the stellar heating through radiation incident on the inner edge of the disk (Dullemond et al. 2001).

Flat Spectrum (FS) sources are a small subset of objects that appear between Class I and Class II. This class is characterised by having a flat far IR and submm SED. Class II objects have a spectral index $-2 \leq \alpha \leq 0$ (Lada & Wilking 1984). These sources no longer have large envelopes, however they still have disks, as in Fig. 2.3. The lack of an obscuring envelope means they are sometimes observable in the visible. The SED continues to show an infrared and submm excess, however the excesses above the protostellar blackbody of the growing core are much smaller. Class II sources are thought to be $10^6 - 10^7$ years old.

The final class is the Class III protostellar objects, these objects have a spectral index $-3 \leq \alpha \leq -2$ (Lada & Wilking 1984). Class III sources are believed to be around 10^7 years old, they are the last class before turning off onto the main sequence. Class III sources have no disk or envelope, Fig. 2.4. Their SEDs are well approximated by blackbodies at the stellar surface temperature and they show no significant IR or submm excesses.

Another observational distinction between young stellar objects is the $H\alpha$ equivalent width (EW). The $H\alpha$ EW is the width of a rectangle centred on the $H\alpha$ emission line with the same area that the $H\alpha$ emission line profile has above the continuum. The $H\alpha$ EW is therefore a measure of the strength of the line profile. Young stellar objects with a mass

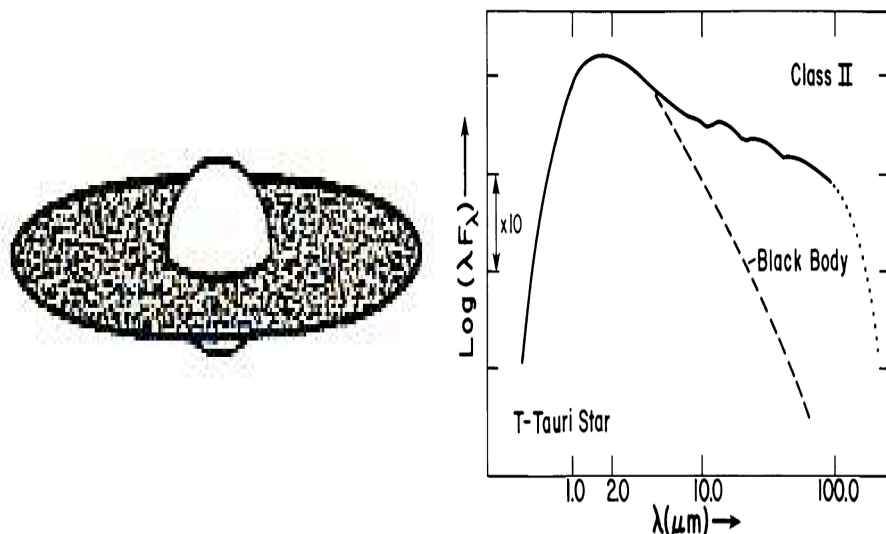


Figure 2.3: Schematic diagram and SED of a Class II star. Class II sources no longer have outer envelopes but they do have smaller dust disks. Class II SED's show continued IR and submm excesses which are clearly above the blackbody protostellar emission (Glass 1999; Lada 1987).

between $0.075M_{\odot}$ and $2M_{\odot}$ in the pre-main sequence phase are known as T Tauri stars (TTS), named after the first such instance of this type of source (Joy 1945). TTS are classified by their spectroscopic characteristics and range from spectral types K0 to M6. They are also known to be very young, $t \sim 10^5 - 10^7$ yrs (Covino et al. 1997) and often show X-ray emission (Neuhäuser 1997). Classical T Tauri stars (CTTS) and Weak-line T Tauri stars (WTTS) are defined depending on their $H\alpha$ EWs (Herbig 1978).

CTTS's have strong $H\alpha$ emission, $EW > 10\text{\AA}$ (Herbig 1978) due to on-going accretion from the disk onto the star. These sources also show IR and submm excesses and since there needs to be continued disk accretion for these objects to maintain a large $H\alpha$ EW it is believed these sources are in the Class II stage.

WTTS's show little or no $H\alpha$ emission, $H\alpha$ $EW < 10\text{\AA}$ (Herbig 1978), indicating little or no accretion from a disk onto the star. This class is associated with significantly reduced IR and submm excesses indicative of a dissipated disk. They often show X-ray emission which indicates the system is still young since X-ray emission from main sequence stars is weak (Neuhäuser 1997).

2.3.3 Binary Star Formation

Multiple star systems are systems comprised of two or more stars with binaries being the most common type. Duquennoy & Mayor (1991) undertook a multiplicity survey of the nearest solar type stars and observed that the majority of the solar neighbourhood G dwarfs are multiple. Overall, a binary fraction of $\sim 60\%$ was observed in the spectral range F7 to G9. This survey was sensitive to both very short period binaries and tight binaries ($P < 1000$ d), using spectroscopy to search for transitions that are observed as

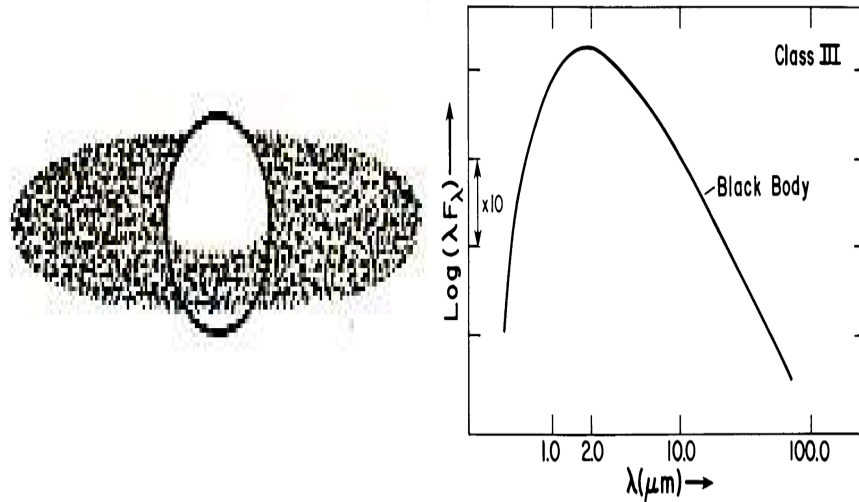


Figure 2.4: Schematic diagram and SED of a Class III star. Class III sources have no disk or envelope. Class III SED's show no excesses and appear to be protostellar blackbody spectra (Glass 1999; Lada 1987).

double lines, through to longer period ($P > 1000$ d) visual binaries and common proper motion binaries. This may not represent the complete sample because very low mass secondaries are difficult to detect with current instruments.

A complimentary multiplicity survey of solar neighbourhood M dwarfs (Fischer & Marcy 1992) measured a lower binary fraction of $42\% \pm 9\%$. Due to the restriction that the primaries be M dwarfs, there is therefore a smaller range of companion masses available. It is thought that the smaller range of companions accounts for the lower binary fraction observed. Fischer & Marcy's survey was able to detect companions down to $0.1M_{\odot}$ with separations from $<1\text{AU}$ to $\sim 10^4$ AU.

A multiplicity survey of field brown dwarfs in the solar neighbourhood by Burgasser (2007), focussed on the L dwarf/T dwarf transition. A binary fraction of $\sim 11\%$ was measured which is lower than the surveys of higher mass stars. However, the restriction on companion masses will have a large effect. Also due to these stars being very low mass and difficult to observe it is thought that $\sim 66\%$ of these objects are too tightly bound to be spatially resolved (Liu et al. 2006). Therefore, there may be a large increase to the observed multiplicity of $\sim 11\%$.

Since the survey by Ghez et al. (1993), binary systems in star forming regions are of particular interest because there appears to be a disparity in the fractions between different star forming regions and with the field stars. Ghez et al. (1993) observed binaries with separations between 16–252 AU and found a binary fraction of $60\% \pm 17\%$, while the binary fraction of solar-type main sequence stars in this range is only $16\% \pm 3\%$. The difference in these binary fractions led to the theory that the stars form in tight clusters as multiples which are then reduced in number due to interactions with other cluster members, leading to companion ejection (Clarke 1996).

Both the Shu and BP model of star formation fail to explain the formation of multiple systems. Therefore, such a high binary fraction creates a problem for these models of star formation. In order to account for the formation of binary and higher order multiple systems three types of formation models have been proposed. These binary formation models are capture, fragmentation, and fission.

The capture formation theory (Clarke 1992) begins with the single star formation scenario and then the stars form pairs through dynamical interaction. However the capture method has flaws. Simple two body interactions would most likely not result in a binary pair; the system would need an additional energy dissipation mechanism (Clarke 1992). One way of achieving this energy dissipation is through tidal circularisation, where the excess energy goes into stellar tides. However, the main drawback of this approach is that the interaction cross section of two body encounters is very small, implying stars would require a very close encounter to become bound (Hills 1976). This kind of interaction is likely to be very rare within star forming regions leading to capture timescales of 10^9 yrs. Another method is to require three body encounters whereby the third star in the encounter provides the energy dissipation mechanism through momentum transfer. The interaction of three stars is less frequent than two star encounters and therefore this method for forming binaries can only work in the densest regions of globular clusters (Portegies Zwart et al. 1997), or in small, tight clusters of stars (Clarke 1996). The capture model does not reproduce the observed binary frequency and results in far more uneven mass binaries than are observed (McDonald & Clarke 1993). The interactions between the young stars during the capture process also act to disturb and truncate disks.

Fragmentation is another possible formation scenario, which can occur when multiple over-densities are present within the collapsing cloud (Pringle 1989). Each over dense region would locally collapse splitting the cloud into more than one initial clump with each clump forming a separate star. This process has been extensively modeled, with interesting results. Fragmentation is found not to occur in free-fall collapsing gas, as such gas is stable against formation of secondary clumps (Boss 1989). However, when infalling gas is modeled as a flattened disk it is found that the disk could fragment multiple times (Tsuribe & Inutsuka 1999). This would imply the existence of many more triple and quadruple systems than are observed. It is only when fragmentation is restricted to only occur once, if at all (Clarke 1996), that the results reproduces the observed binary frequencies and mass ratio distribution more accurately than the capture model. Yet the problem remains of why a system would only undergo a single fragmentation. Ultimately, fragmentation is seen as a viable formation method for binaries and is also thought to be a possible method of low mass star formation and planet formation (discussed later).

The fission model, a third formation mechanism, requires the cloud to have very large amounts of angular momentum (Lyttleton 1953). Fission can happen during the accretion of the disk where the material hitting the star also deposits angular momentum. Rapidly rotating bodies can deform, possibly into the shape of a dumbbell (Lebovitz 1974), and split. Even with this splitting it could only account for the very tightest of binary

systems. Attempts to model this formation mechanism have proved to be very difficult as the limit of current computing power does not allow the simulations to achieve the required resolution as the cloud collapses. With the best model to date failing to produce a binary system as their computing power was limited (Cazes 1999).

2.3.4 Low Mass Star and Brown Dwarf Formation

Observations of the galaxy reveal that low mass stars and brown dwarfs form the majority of objects with the number of sources increasing towards lower masses (Scalo 1986). The low mass star and brown dwarf range extends from hydrogen burning stars, spectral types K1 to M6, to stars which only have sufficient mass to burn deuterium, M6 to T8. During the Class II stage of formation the M6 spectral type delineates the boundary between hydrogen and deuterium burning. The boundary occurs at a stellar mass of $\sim 0.075 M_{\odot}$ (Martín 1997).

Formation models have been proposed which attempt to account for low mass star and brown dwarf formation, $M < 1M_{\odot}$. Substellar objects could possibly form in the same way as higher mass stars. There are also a broad range of other models which could produce these objects.

The ejection model (Bate et al. 2002) could be used to account for high proper motion single brown dwarf systems. In this model protostellar cores are dynamically ejected from their host clouds, perhaps in the interaction to form a binary system. Once ejected from their natal envelope they no longer have any gas to accrete and therefore stay at their ejection mass. If this occurs early enough in the formation process the stars will be ejected at brown dwarf masses. A similar formation mechanism is the photoerosion model (Whitworth & Zinnecker 2004) where the envelope around the forming star is eroded by a nearby massive star. This stops accretion onto the surface and thus removing the reservoir of that would increase the mass of the protostar.

These substellar objects are difficult to observe. They are still embedded in dust, which results in extinction of their radiation, this combined with their low mass, and hence temperature, means they have a low luminosity. These formation scenarios are not mutually exclusive and it is thought low mass stars form from all of the models detailed.

2.4 Circumstellar Material

Circumstellar material around young stellar objects is a natural consequence of many star formation scenarios. The envelopes and disks dissipate as gas and dust accretes. The accretion also results in the star gaining mass, which results in increased stellar winds that act to remove some of the circumstellar material. Planetary systems can form from circumstellar material during the Class I and II phases of formation (Pollack et al. 1996; Boss 2000).

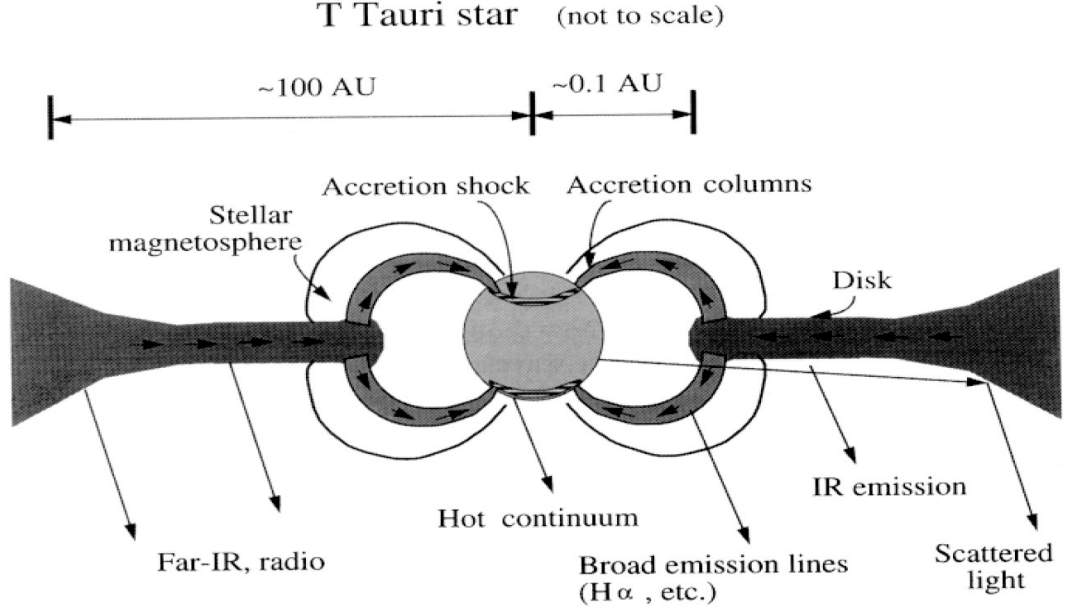


Figure 2.5: Schematic diagram of a T Tauri star including the emission regions. The accretion columns generate the hot continuum optical emission when they strike the surface. The columns of hot gas themselves produce the observed broad emission lines. Inner disk regions emit IR radiation while the outer disk regions emit in the far IR and submm/mm (Feigelson & Montmerle 1999).

2.4.1 Disk Emission

The gas and dust within the disk emit over a large range of wavelengths. Ground based measurements are typically made at three main wavebands with high atmospheric transparency. Two probe the inner disk region, optical/UV and IR, and one the outer, submm/mm.

The optical/UV continuum emission is caused by the inner edge material being heated during the accretion process as well as the intrinsic stellar luminosity. The gas is confined to the inner edge of the disk by the stellar magnetic field, Fig. 2.5. The accreting material is channeled along the magnetic field lines resulting in much greater impact speeds, \sim few hundred kms^{-1} , with the stellar surface. This causes shocks, which in turn cause the strong optical/UV continuum (Bouvier et al. 1995). These accretion columns also cause the broad emission lines, $\text{H}\alpha$, that are observed.

The infrared excess is caused by thermal reprocessing of the stellar radiation incident on the dust in the inner disk. These inner regions are optically thick and therefore observations in the IR can probe the temperature structure of the disk. The temperature of the dust at the disks inner edge can be estimated by the equation

$$T_d^4(R) \sim \frac{T_{\text{eff}}^4}{\pi} \left(\frac{R_*}{R} \right)^3, \quad (2.4)$$

where T_{eff} is the temperature at the photosphere of the protostar, R_* is the radius of the

protostar and R is the radius of the inner disk. This results in a temperature of ~ 1000 K at ~ 0.01 AU around a typical T Tauri star assuming all the IR emission is from the heated inner disk (Adams et al. 1988).

The outer regions of the disk are cool, $T \sim 20$ – 100 K, and they primarily emit in the submm/mm. The intensity of the emission is dependant on a number of factors including the temperature of the dust and also the disk surface density profile. The dust in the outer regions of the disk is thought to be optically thin and therefore can be used as a tracer of mass (Hildebrand 1983).

The calculation of dust mass can be made using the relation, assuming an optically thin outer disk,

$$M_d = \frac{d^2 F_\nu}{\kappa_\nu B_\nu(T_c)}, \quad (2.5)$$

which assumes an isothermal region, with a characteristic temperature (T_c). The flux, at a particular frequency, received by the telescope from the dust is F_ν at a distance, d . The opacity of the dust is κ_ν , while B_ν is the Planck function at the dust temperature, T_c . This is a gross simplification; the size, orientation and chemistry of the dust grains will also change the nature of radiation from the disk (Draine & Lee 1984; Miyake & Nakagawa 1993).

Graphite and silicate grains are thought to be the main dust constituents in disks (Mathis et al. 1977). These grain types were tested under laboratory conditions to determine their scattering and reflection properties. These experiments showed that the dielectric functions of the grains have a large temperature and size dependence at long wavelengths $\lambda > 1$ mm (Draine & Lee 1984). Laboratory testing also found that larger sizes of grains lower the opacity index of the dust (Miyake & Nakagawa 1993). The dust opacity index, β , is an indication of how the dust reacts to incident light at a certain frequency. If the frequency is such that the wavelength of the light is small compared to the size of the dust particles then the opacity index will be ~ 0 . Therefore particle growth within dense environments, like circumstellar disks, would result in a lower opacity index. The dust opacity index measured in disks, $\beta \sim 0$ – 1 (Beckwith & Sargent 1991), is much lower than that of the ISM, $\beta \sim 2$ (Hildebrand 1983). By modeling the disk with both small particles, $\sim 0.1 \mu\text{m}$, and large particles, ~ 1 cm, the total dust opacity index observed within disks can be replicated (Miyake & Nakagawa 1993).

2.4.2 Disk Properties

The emission from disks around young stellar objects allow us to calculate disk properties. Disk radii can be estimated by observing disks in the mm wavebands. However, in order to get the resolution required to determine disk sizes interferometry is required. Lay et al. (1994) conducted a disk size survey and found that disks have a typical radius of ~ 100 – 300 AU. While the largest disks observed have radii ~ 1000 AU. They were observed as silhouettes against the bright optical background of the Orion Nebula using the Hubble Space Telescope (McCaughrean & O’Dell 1996). The current sample of resolved disks are

likely to represent the upper range of disk sizes since current instruments cannot resolve the smaller disks. Disk sizes are also heavily affected by environmental factors such as a binary companion (Artymowicz & Lubow 1994).

The optically thin approximation, discussed in the previous section, has been used to obtain a lower limit of the mass of dust in the system. Using measured fluxes at 1.3mm, Beckwith et al. (1990) estimated the range of T Tauri disk masses to be between 0.001 and 1 M_{\odot} . More recent measurements suggest the average disk mass is around 0.005 M_{\odot} (Andrews & Williams 2005, 2007a). This mass is similar to the calculated mass of the minimum mass solar nebula (MMSN), $M_d \sim 0.01 M_{\odot}$ (Weidenschilling 1977). The MMSN was a value produced by calculating how much solar type material was needed in order to form all the planets. It was done by summing the solar component of iron in the planets as well as estimating the mass of the asteroid belts. This is an indication of how much material was around our own sun as it was forming.

Binary systems can have more than one associated disk. A circumbinary disk surrounding both components of the binary system can form as well as two separate circumstellar disks around each individual member. These disks interact gravitationally with each other and with their stars. Papaloizou & Pringle (1977) calculated how circumstellar disks are affected by the tidal forces induced by the binary system. These simulations showed that circumstellar disks in binary systems would accrete quickly enough onto the stars to leave no remaining circumstellar disk in a very short timescale, ~ 1000 yrs. Since circumstellar disks are observed around binary members it is believed that they are constantly replenished by flows from circumbinary disks. Artymowicz & Lubow (1994) simulated the interaction disks with each other. Their simulations found that the circumstellar disks were truncated in size with large gaps between the circumstellar disks and the circumbinary disks, leaving it uncertain as to whether the circumbinary material could replenish the circumstellar disks. Observations have detected the gaps within the disks in binary systems (Jensen & Mathieu 1997). Recent observations, which detect periodic variations in luminosity indicative of accretion streams suggest that the flow of material across these gaps is possible (Jensen et al. 2007). Due to truncation by tidal forces binary systems are expected to have smaller disks than their single counterparts.

2.4.3 Disk Dissipation

Disks must dissipate at some point since they are not observed around all stars. The frequency of observed disks appears to have a linear relationship with the age of the system (Hillenbrand 2005), the younger a star is the more likely it is to still retain a disk. This is uncertain since system ages are not well determined. Most disks are present for ~ 2 Myr (Beckwith et al. 1990), however, there are some long lived disks which appear to be ~ 10 Myr (Takeuchi et al. 2005).

There are several mechanisms which act to remove the gas and dust present in the disk. The circumstellar material accretes through the disk and onto the star. The circumstellar material can also be blown away by increasing stellar winds and radiation

(Hollenbach & Gorti 2005; Adams et al. 2004). Planetary systems can also be formed within disks, in this case the circumstellar material accumulates together to form the planets (Safronov 1966).

The circumstellar disk facilitates the removal of angular momentum from the material in the inner disk to the outer disk. As the inner material loses angular momentum it accretes onto the young stellar object. This accretion rate of disk material onto the stellar surface is highly variable from 10^{-9} – $10^{-7} \text{ M}_{\odot} \text{ yr}^{-1}$ (Gullbring et al. 1998). It is therefore possible some smaller disks around low mass stars accrete most of their material onto the star. Disks have been observed to be eroded by stellar winds from massive stars in the Orion Nebula Cluster (Adams et al. 2004). It is also possible that the parent stars stellar wind can erode the disk (Hollenbach & Gorti 2005). Massive stars have a much larger UV flux than lower mass stars. The UV flux photodissociates the material in the disk which creates the winds to blow out material from the disk.

The final scenario for how disks dissipate is the formation of a planetary system. Grain growth within disks, several smaller dust particles agglomerating together and forming a single larger particle, follows from the observed opacities of disks. This grain growth is the initial stage of planet formation by the core accretion model (Pollack et al. 1996). In the core accretion model, larger particles are formed from the smaller particles. The large particles formed continue to merge together until the gravity of one of these particles is enough to attract other dust particles in its vicinity. However, metre sized particles no longer stick together on impact and they do not possess enough mass to clump together gravitationally. There is no solution to this problem as yet, one possible explanation was put forward by Johansen et al. (2007) whereby high pressure, high density regions are created by turbulence within the disk. Once clumps which are $\sim 1 \text{ km}$ in size form, they agglomerate due to gravity. The process of agglomeration continues until the core has enough mass to accrete the surrounding gas. Building the core is a very slow process, $t \sim 10 \text{ Myr}$, which is at the very limit of disk survival timescales. The timescales are so slow because the gravitational attraction of the smaller particles is very small and the ability of the larger particles to stick together is also poor (Safronov 1969).

The other model of planet formation is the disk instability model (Boss 1997). In the disk instability model planets are formed due to gravitational instabilities in the disk. The gravitational instabilities are usually present due to a region of the disk with a density enhancement. These density enhancements are produced by cooling within the disk causing material to clump together under gravity. Regions that do have a greater density than the average of the disk can collapse becoming self gravitating clumps. These clumps continue to accrete more gas from the rest of the disk, which becomes the envelope of a giant planet. The planet's core forms later when the dust within the initial clump settles centrally. The timescale of this formation mechanism is far shorter, $t \sim 10^4 \text{ yr}$, which is well within the disk survival timescale (Boss 2000). The disk instability model only works for disks that are either cool or have very efficient cooling, otherwise the disks appear stable against fragmentation (Gammie 2001).

Chapter 3

Submm/mm Observations

3.1 Atmospheric Windows

Ground-based submm/mm observations are possible in several wavelength ranges corresponding to windows of high transmission through the atmosphere: $350\ \mu\text{m} - 60\ \text{m}$. Figure 3.1 shows the atmospheric transmission from 0 GHz to 1000 GHz and indicates that even with only 1mm precipitable water vapour present the transmission varies from 0 % to 100 %. In order to avoid the adverse affects of the atmosphere submm/mm telescopes are located at high, dry sites such as Mauna Kea and Chajnantor, Chile, where the next generation interferometer ALMA will be located.

Submm/mm observations are taken with either single dish telescopes or interferometers. Single dish observations probe the total flux of an object but have limited resolution due to their limited size. Interferometers have increased resolution but do not recover the total flux as effectively as single dish measurements. The data for this project were taken with the OVRO interferometer array located in the Owens Valley where the precipitable water vapour ranges from $\sim 2.0\text{mm}$ in good winter conditions to $\sim 7.0\text{mm}$ in acceptable summer conditions. Since data acquisition the OVRO array has been merged with another array and moved to a higher site with improved atmospheric conditions to form CARMA.

3.2 Submm/mm Telescopes

In submm/mm astronomy the source intensity, I , is measured by collecting photons emitted by the source, normally using a parabolic dish to focus the incident radiation to a receiver system. These intensities are usually quoted in Janskys (Jy), where $1\ \text{Jy} = 10^{-26}\ \text{W m}^{-2}\ \text{Hz}^{-1}$. Another method of defining intensities is the brightness temperature (T_B), which is the temperature a theoretical blackbody would have in order to replicate the peak of the observed (non-blackbody) intensity. The brightness temperature does not necessarily have any physical correlation with the source, unless the source itself is a blackbody.

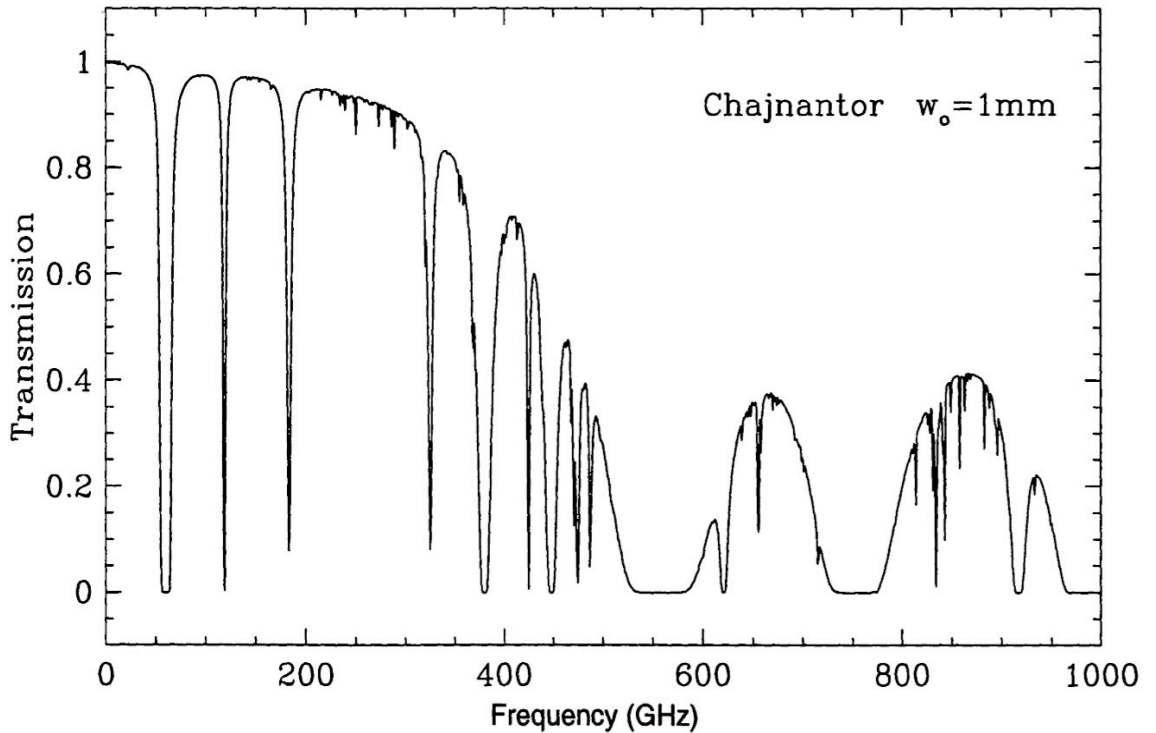


Figure 3.1: The atmospheric transmission between 0 GHz and 1000 GHz, which corresponds to a wavelength range of 30 cm to $300\,\mu\text{m}$, at Chajnantor in Chile the site of ALMA. This is assuming a precipitable water vapour content of 1mm which is typical for this site. This clearly shows the windows in which ground based observations are possible. The main windows are around 850 GHz ($350\,\mu\text{m}$), 650 GHz ($450\,\mu\text{m}$), 350 GHz ($850\,\mu\text{m}$) and below 300 GHz (above 1 mm) (Carilli et al. 1999).

3.2.1 Single Dish

A single dish receiver measures the convolution of the source intensity with the beam of the antenna. A schematic diagram of the beam is shown in Fig. 3.2. The beam pattern is due to diffraction at the aperture of the far field waves from the source; leading to interference between waves coming in at different angles. This results in a series of maxima and minima at the focus of the dish, which in 2-dimensions is an Airy disk. The central maxima of the Airy disk is a Gaussian, this is the main beam and represents the direction that the dish receives the greatest percentage of the incoming waves. The diffraction pattern also results in other maxima away from the direction of the source being observed. These are regions outside the main beam that, due to constructive interference, also contribute to the measured signal, these are known as beam sidelobes.

The largest single dish observatory that operates at Submm/mm wavelengths is the 30 m IRAM dish. Dishes at Submm/mm wavelengths have a number of constraints on the maximum size of a dish. There is a cost issue: the cost of dishes and supporting structures increases with increasing dish sizes. The price is empirically defined by Christiansen & Hogbom (1985) as $\propto D^2 \lambda^{-0.7}$. There are also constraints on dish size due to possible

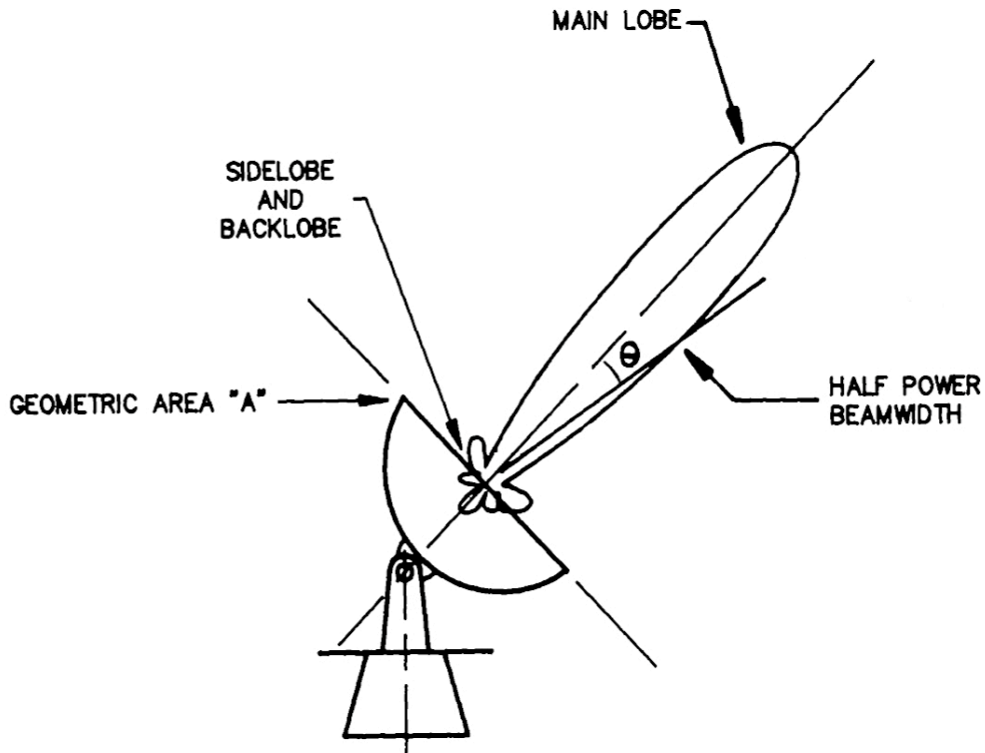


Figure 3.2: The beam pattern of a circular aperture is shown as a 2-dimensional cross-section. The sizes of the lobes schematically represent how much of the signal strength is received in that direction. The side lobes, the first of which are at $\sim 60^\circ$, also contribute to the signal, including from behind the receiver. The half power beamwidth (θ), a measure of dish resolution, is also shown (Napier 1999).

deformation by gravity. A larger dish is going to deform more since it is heavier. These deformations distort the parabolic nature of the dish resulting in a reduction in the sharpness of the focus, discussed by Akabane (1983) in relation to the Nobeyama telescope. Modern submm/mm dishes are built in such a way that the gravitational deformations which affect the dish deform it into another parabola, for example the adaptive dish surface at the Caltech Submillimeter Observatory (CSO) (Leong et al. 2006) and the similar dish adjustment system on the JCMT.

3.2.2 Interferometry

In order for a dish to have a diffraction limit lower than ~ 1 arcsecond at 1 mm a dish diameter of ~ 200 m would be required. Telescopes at Submm/mm wavelengths cannot be built this size due to weight and cost issues. The need for higher resolution led the development of interferometry. Current interferometers include SMA, consisting of eight 6m dishes, and CARMA, consisting of six 10m dishes and nine 6m dishes, while a future instrument is ALMA, consisting of fifty 12m dishes. Interferometric observations use more than one dish to observe the same source at the same time. The simplest kind of interferometer is a two-element interferometer also known as a Michelson interferometer (Michelson 1920).

The Michelson interferometer was developed for use at optical wavelengths but the idea was later extended to radio wavelengths, a diagram of a two element radio interferometer is shown in Fig. 3.3. The distance (\mathbf{b}) between the two antennae leads to a geometrical time delay,

$$\tau_g = \frac{\mathbf{b} \cdot \mathbf{S}}{c}, \quad (3.1)$$

where \mathbf{S} is the source direction and c is the speed of light, in the time it takes signals to reach one antenna compared to the other.

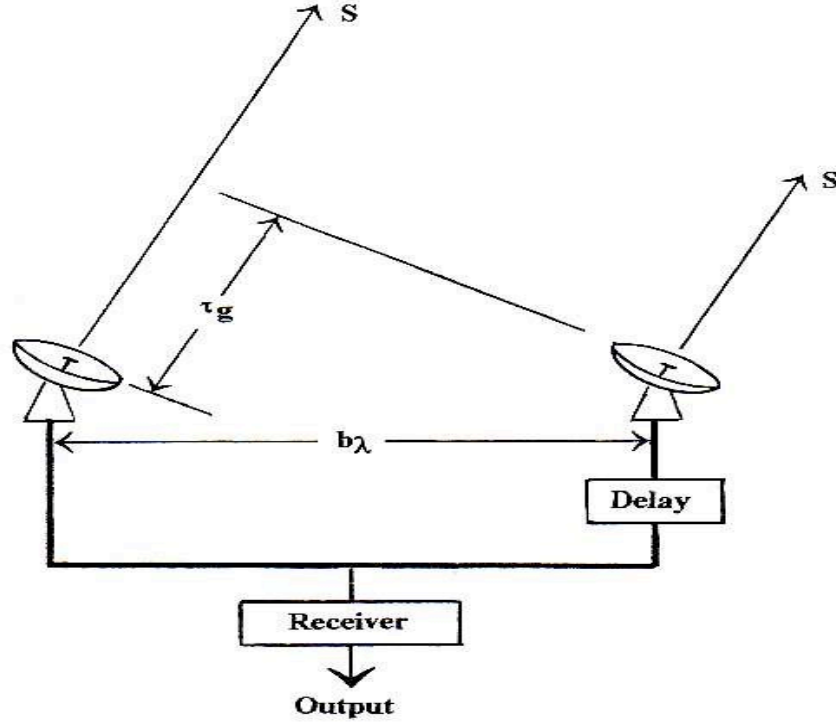


Figure 3.3: A two element interferometric system. The baseline vector is \mathbf{b}_λ , while the source direction is \mathbf{S} . The geometrical time delay, τ_g , is shown in terms of signal travel length. A delay is added to compensate for the geometrical time delay in order to match the phases of the signals at the receiver (Thompson 1999).

The time delay results in interference between the signals received by the two antennae and results in a fringe pattern, shown in Fig 3.4. This fringe pattern changes as the source position changes due to the Earth's rotation, with the position of maximum fringe strength revealing the position of the source. Therefore, a map of the source can be built up by measuring the visibility (V) over time of the fringe pattern. Extending this theory to use more than one pair of antennae gives the ability to produce a 2-dimensional map of the source brightness.

In order to make use of pairs of antennae measuring visibilities interferometry observations use the u,v coordinate system. The u,v -plane is defined as the plane in which the antennae lie, i.e. at any time the baseline between two antennae is one vector in the u,v -

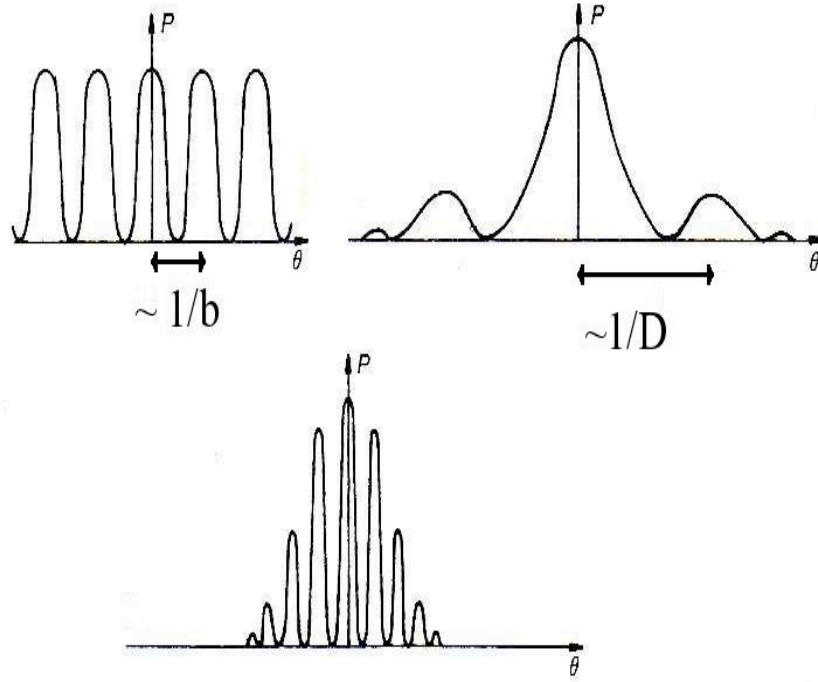


Figure 3.4: Top Left: The fringes that result from two antennae (analogous to Youngs two slit experiment) with a separation, b . Top Right: The single dish beam pattern of each antenna of diameter, D . Bottom: The response of the interferometer system to a point source in the direction of the main beam of each antenna (Burke & Graham-Smith 2002).

plane. Aperture arrays were designed to take advantage of antenna pairs sampling single visibilities in the u,v -plane. These arrays have different baselines between each antenna, which then produces visibilities for different points in the u,v -plane. In addition to sampling different points in the u,v -plane at any one time, the projected baselines change due to the Earth's rotation, resulting in greater sampling of the u,v -plane. With each antenna pair contributing the visibility for a single u,v coordinate, it is possible to build the source brightness distribution at the corresponding x,y coordinate by Fourier transforming the visibilities,

$$V(u, v) \Leftrightarrow I(x, y). \quad (3.2)$$

Before Fourier inversion, the measured visibilities must be calibrated, usually done by observing a source of known flux within the track. They are then Fourier inverted to form an image. However, due to the lack of complete u,v coverage the generated image is not a true representation of the source brightness distribution. It is therefore important to account for the incomplete u,v coverage. This is done using a deconvolution algorithm called CLEAN (Högbom 1974), described in more detail in Section 5.

3.3 Resolution Limits

The minimum separation two objects can have and still be distinguishable is the angular resolution and is due to diffraction. This resolution limit is shown in Fig. 3.2 as the half power beamwidth. The maximum resolution that a single dish can achieve is,

$$\theta_{\text{sd}} \sim \frac{\lambda}{D}, \quad (3.3)$$

where λ is the wavelength of the observation and D is the diameter of the dish. There is also a trade-off with the field of view (fov) of a telescope and its size,

$$\Omega_{\text{sd}} = \frac{\lambda^2}{A}, \quad (3.4)$$

where Ω_A is the telescope field of view and A is the collecting area of the dish. Therefore, in order to have a large field of view the telescope area needs to be small. However, a minimum in telescope area also corresponds to a poor sensitivity limit.

A single dish observation is able to probe all spatial frequencies at once up to the resolution limit. An interferometer is only responsive to spatial frequencies between the minimum and maximum antennae separation. The achievable resolution of an interferometer is determined by its maximum baseline length,

$$\theta_{\text{I}} \sim \frac{\lambda}{b_{\text{max}}}, \quad (3.5)$$

where λ is the wavelength of observation and b_{max} is the maximum baseline. The minimum antenna separation gives an indication of how much structure is resolved out by the interferometer. Structures larger than λ/b_{min} do not contribute to the flux measured by the interferometer; this flux can only be recovered in single dish observations or by decreasing b_{min} at the expense of resolution. The field of view of an interferometer is also limited by the size of the antennae's beamwidth,

$$\Omega_{\text{I}} \sim \frac{\lambda}{D}, \quad (3.6)$$

where D is the diameter of the dishes used in the interferometer. A summary of the resolution limits of current submm/mm observatories in comparison to the OVRO array is presented in Table 3.1.

3.4 Noise & Sensitivity

An ideal telescope system would collect radiation from the source, which could immediately be interpreted as an intensity. However, all observations have noise, which limits the sensitivity that a receiver can achieve. Noise arises from a number of different sources, for example the dish structure emits some photons at the wavelength of observation that can contaminate a signal. The system intensity, quoted in temperature units, at the output

Single Dish	Resolution
IRAM (1 mm)	11"
JCMT (850 μm)	15"
CSO (350 μm)	9"
Interferometers	Resolution
OVRO (3 mm)	2.5"
SMA (1 mm)	0.3"
CARMA (1 mm)	0.3"
ALMA (1 mm)	0.011"

Table 3.1: Resolution limits at Submm/mm observatories. Interferometers have greatly increased resolution over single dish observatories. ALMA is the next generation interferometer currently under construction.

consists of the source flux and the noise contributions,

$$T_{\text{sys}} = T_{\text{s}} + T_{\text{b}} + T_{\text{atm}} + T_{\text{r}}, \quad (3.7)$$

where T_{sys} is the measured system temperature, T_{s} is the source temperature, T_{b} is the noise of the background sky, T_{atm} is the noise contribution from the atmosphere, T_{r} is the contribution from the noise of the receiver, including dish noise.

The sensitivity of a telescope is not only governed by the noise but also the size of the telescope. The number of submm/mm photons from the astronomical source collected increases with increasing dish area (A), the sensitivity limit $S \propto N_{\text{photons}}^{-1} \propto A^{-1}$. The more photons a dish can collect and focus, the lower the sensitivity limit of the dish allowing fainter objects to be observed. Also affecting the sensitivity is the range of frequencies a receiver is responsive to, this also has the effect of increasing detectable photon numbers. The noise contribution to the source is Gaussian random noise, which allows a lower limit to be placed on the achievable sensitivity of the telescope system. The single dish limiting rms flux sensitivity (ΔS_{sd}) of a point source is,

$$\Delta S_{\text{sd}} = \frac{2kT_{\text{sys}}}{A\sqrt{B\tau}}, \quad (3.8)$$

where k is the Boltzmann constant, T_{sys} is the noise temperature of the telescope, A is the receiving area, B is the receiver bandwidth and τ is the on-source integration time.

The sensitivity of an interferometer (ΔS_{I}) is limited by the sensitivity of each dish. An interferometer of N antennae has a sensitivity of,

$$\Delta S_{\text{I}} = \frac{2k}{\eta_{\text{s}}} \frac{T_{\text{sys}}}{AN(N-1)\sqrt{B\tau}}, \quad (3.9)$$

where k is the Boltzman constant, η_{s} is the system efficiency, T_{sys} is the system temperature, A is the area of a single dish, B is the receiver bandwidth and τ is the integration time. This assumes all the antennae have the same T_{sys} when observing the same source. Interferometers, despite greatly increasing the possible resolution, do not greatly enhance

the sensitivity. A summary of the sensitivity of OVRO and current submm/mm observatories is presented in Table 3.2.

Single Dish	Sensitivity [mJy]
IRAM (1 mm)	1.5 (10 mins)
JCMT (850 μm)	35 (72 mins)
CSO (350 μm)	24
Interferometers	Sensitivity [mJy]
OVRO (3.3mm)	3
SMA (1 mm)	6.5
CARMA (1 mm)	2.5
ALMA (1 mm)	0.25 (10 mins)

Table 3.2: Sensitivity limits at Submm/mm observatories. Sensitivities are listed for 60 minutes on source time unless otherwise stated, all times are on source times. Note that interferometers do not offer increased sensitivity.

Chapter 4

Sample & Observations

4.1 Ophiuchus

A good laboratory to study the initial stages of star and planet formation is the ρ Ophiuchus molecular cloud complex. ρ Ophiuchus is one of the nearest, ~ 140 pc (Mamajek 2008), dark cloud star forming regions with no massive stars. The region has a spatial extent of $\sim 5^\circ \times 5^\circ$ which corresponds to ~ 12 pc \times 12 pc. The ρ Ophiuchus region is split into many clumps throughout the cloud, which have a total mass of $\sim 3 \times 10^3 M_\odot$ (Loren 1989). The most massive clump is the L1688 cloud, which has a mass of $\sim 8 \times 10^2 M_\odot$ (Loren 1989). L1688 is also the region where most of the current star formation is taking place (Nutter et al. 2006). Optical and millimetre images of the cloud are shown in Fig. 4.1.

4.2 Previous Surveys

4.2.1 Non Submm/mm Surveys

The region was observed by the Infrared Astronomical Satellite, IRAS, (Beichmann 1985) at mid and far infrared (12, 25, 60 and $100 \mu\text{m}$) revealing 652 sources with high signal to noise at $12 \mu\text{m}$ and $25 \mu\text{m}$. More recently, the cloud has been studied with Spitzer at mid IR wavelengths with both the IRAC (3.6, 4.5, 5.8 and $8 \mu\text{m}$) and MIPS (24 and $70 \mu\text{m}$) instruments. Using the IRAS survey as a template, Ichikawa & Nishida (1989) surveyed the region in the optical and discovered 577 IRAS detections coincided with an optically detected star. The 2 Micron All Sky Survey, 2MASS (Cutri et al. 2003), observed the J ($1.25 \mu\text{m}$), H ($1.65 \mu\text{m}$) and K ($2.17 \mu\text{m}$) bands providing near infrared coverage of the region.

A survey at wavelengths of 3 and 6 cm was conducted using the Very Large Array (VLA) by Leous et al. (1991). This survey discovered over 40 sources within the Ophiuchus region many of which were coincident with shorter wavelength detections. The ρ Ophiuchus cloud was also observed by Chandra in the X-ray region of the spectrum. Chandra detected 87 sources, 60 of which were previous known YSO's (Gagné et al. 2004).

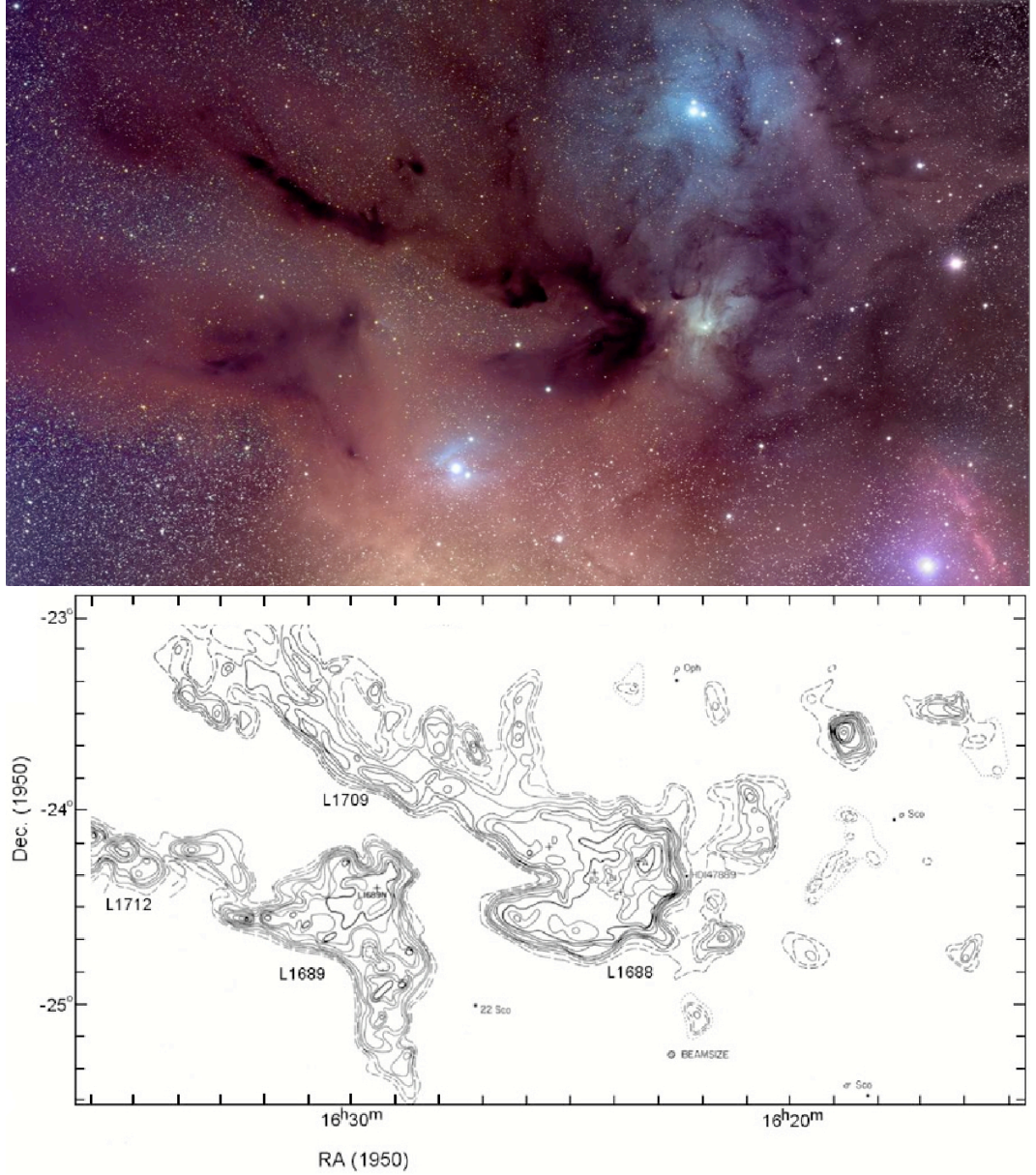


Figure 4.1: Top: Optical image of the ρ Ophiuchus molecular cloud complex from www.fourthdimensionastroimaging.com. Easily identified are the triple system ρ Ophiuchi, top right of image, the L1688 cloud, the dark cloud in the centre of the image, the L1689 cloud, the cloud to the left of centre and the L1709 cloud, the dark lane in the top left portion of the image. Bottom: The ^{13}CO 1-0 transition map of the entire ρ Ophiuchus cloud complex from Nutter et al. (2006). The ^{13}CO 1-0 effectively maps the cold molecular gas that forms the stars. This is used instead of H_2 due the comparative strength of its emission. The maps cover the same region.

Many of the sources in this survey were previously observed by these non Submm/mm instruments, which has allowed me to build complete SEDs, from optical to Submm/mm, of those sources.

4.2.2 Submm/mm Surveys

Three previous surveys of the ρ Ophiuchus dark cloud form the background sample for the work in this thesis. The IRAM telescope operating at 1.3 mm was used in the surveys of both Andre & Montmerle (1994) and Motte et al. (1998). While, the survey of Andrews & Williams (2007a) used both the JCMT operating at 450 μ m and 850 μ m and the CSO operating at 350 μ m.

The IRAM telescope is a 30 m dish located at Pico Veleta in Southern Spain. The half power beam width at 1.3 mm is $\sim 11''$. For the observations of Andre & Montmerle (1994) the effective observing frequency of this instrument was 240 GHz (~ 1.3 mm) with a bandwidth of 50 GHz. They achieved a 3σ sensitivity of ~ 20 – 30 mJy during ~ 10 minute observations in very good weather. Their sample consisted of over 100 sources from Class 0 to Class III. Single pointings of the dish for each source were used to recover the peak flux. Also included in this survey were maps of the brighter and more extended sources, compiled by scanning the telescope across the source. These maps were $2' \times 1'$ in size but had a poor sensitivity of ~ 100 – 200 mJy. The maps allow a determination of total flux for the strong, extended sources.

The survey of Motte et al. (1998) used a receiver with an effective observing frequency of 240 GHz with a bandwidth of 70 GHz. All of the analysis in this survey was undertaken by mapping the regions by scanning the telescopes around the region of the sources, in order to recover total (not just peak) fluxes. The maps were produced to a 3σ sensitivity level of ~ 24 mJy in good weather for ~ 1 hour integration times. Fifty maps were made and combined in a mosaic to form a map covering an area of ~ 480 arcmin². This survey discovered over 60 starless core candidates and provided the first 1.3 mm detections of 15 other young stellar objects of Class I or Class II.

The survey of Andrews & Williams (2007a) used the Submillimeter Common-User Bolometer Array (SCUBA) on the JCMT to observe 48 Class I to Class III sources at 450 μ m and 850 μ m. The JCMT is a 15m telescope on Mauna Kea in Hawaii with receivers that operate between 450 μ m and 1 mm. SCUBA provided simultaneous measurements of the 450 μ m flux and the 850 μ m flux of each source. The SCUBA beam sizes for these measurements were $9''$ and $15''$ respectively. Each source was observed in good weather for integration times of ~ 10 minutes to achieve a 3σ sensitivity of ~ 200 mJy at 450 μ m and 8.4 mJy at 850 μ m.

Andrews & Williams (2007a) also used SHARC II (Dowell et al. 2003) on the CSO to observe an additional 7 sources at 350 μ m. The CSO is a 10 m dish on Mauna Kea that operates between 350 μ m and 2.1 mm. The beam size of these observations was $\sim 9''$. The survey mapped the 7 sources with integration times of between 120 and 600 s to detect all sources with a 3σ rms of ~ 100 mJy. The survey of Andrews & Williams (2007a) provides a comparison survey to this project as it includes calculations of disk mass and dust opacity up to 1.3 mm for most of the sources in this sample, it does not include starless or Class 0 objects.

4.3 OVRO Sample

To investigate the complete evolution of circumstellar material the 3.3 mm OVRO survey was chosen to cover starless cores to Class III objects. The sample consisted of 36 Class 0 through to Class III targets from the 1.3 mm survey of Andre & Montmerle (1994). Also included were 13 starless cores from the 1.3 mm survey of Motte et al. (1998). These starless sources were selected from the Motte et al. (1998) survey on the basis that they remained either unresolved with the beam size of 11'' or resolved to have a size small enough such that the interferometer would not resolve out any of the flux on large spatial scales. In addition to the objects of known class, 11 other sources with no previously assigned class were present within the field of view of other source. Their flux upper limits are included for completeness. Figure 4.2 provides a breakdown of the class and spectral type of the sources in the survey, while Table 4.1 contains the complete sample and includes whether the sources have been detected other wavelengths.

With the increased resolution available with the OVRO interferometer we can, not only, provide 3.3 mm data on these sources for the first time but also spatially resolve the emission from some of the more extended sources. Additionally these new data allows us to probe the dust opacity index of these sources by extending the SED further into the mm range. This should allow an estimation of the dust opacity index without needing to worry about contamination from optically thick emission, which may be present at Submm wavelengths.

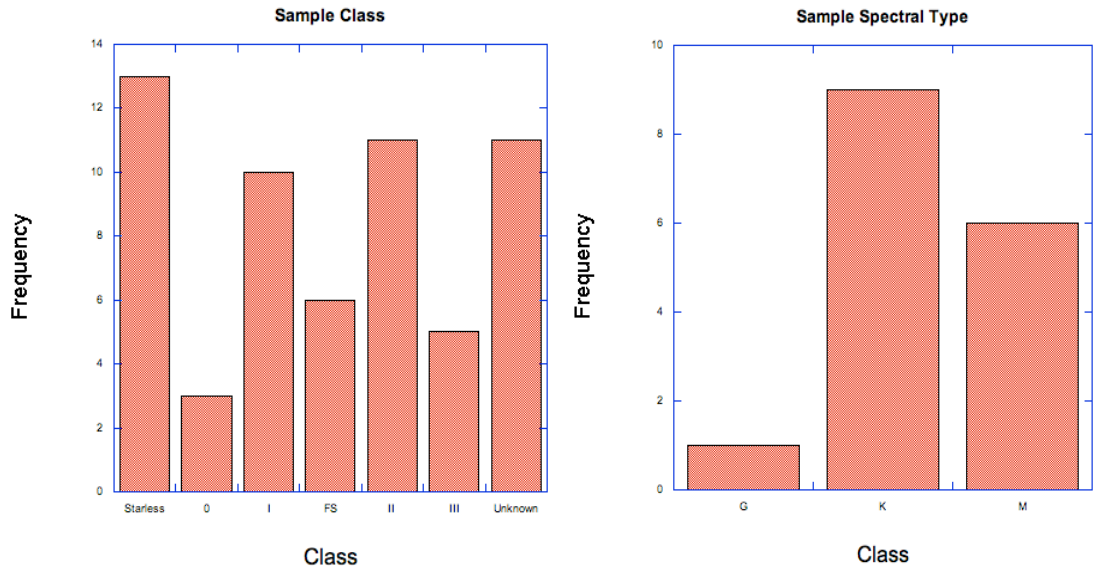


Figure 4.2: Histograms of the key properties of the sample. Left: The breakdown of Young Stellar Objects by SED classification, see also Table 1. Right: The known spectral types of the sample, mainly types K to M.

Table 4.1: Table presenting the basic properties of the sample, first ordered by Class and then alphabetically. RA and Dec are given in J2000 epoch. Individual fluxes for all the detections are given in Appendix B. IRAS16293 A and B were observed in one map.

Source Name	SED Class	Spectral Type	RA (hms)	Dec (dms)	X-ray Detection	Optical Detection	IR Detection	submm/mm Detection	radio Detection
A-MM1	starless	starless	16:26:22.4	-24:23:40	No	No	No	Yes	No
A-MM2	starless	starless	16:26:23.0	-24:24:00	No	No	No	Yes	No
A-MM3	starless	starless	16:26:23.3	-24:24:16	No	No	No	Yes	No
A-MM7	starless	starless	16:26:29.2	-24:22:34	No	No	No	Yes	No
A3-MM7	starless	starless	16:26:10.3	-24:23:06	No	No	No	Yes	No
A-S	starless	starless	16:26:43.1	-24:23:06	No	No	No	Yes	No
B2-MM7	starless	starless	16:27:27.9	-24:27:39	No	No	No	Yes	No
B2-MM8	starless	starless	16:27:28.1	-24:27:11	No	No	No	Yes	No
B2-MM10	starless	starless	16:27:29.6	-24:27:37	No	No	No	Yes	No
B2-MM14	starless	starless	16:27:32.8	-24:26:29	No	No	No	Yes	No
B2-MM15	starless	starless	16:27:33.5	-24:26:20	No	No	No	Yes	No
B2-MM16	starless	starless	16:27:34.5	-24:26:12	No	No	No	Yes	No
B2-MM17	starless	starless	16:27:35.2	-24:26:21	No	No	No	Yes	No
<i>IRAS16293A</i> ¹	0	...	16:32:22.9	-24:28:36	No	No	Yes	Yes	Yes
<i>IRAS16293B</i> ¹	0	...	16:32:22.6	-24:28:32	No	No	Yes	Yes	Yes
LFAM 5	0	...	16:26:26.4	-24:24:31	No	No	Yes	Yes	Yes
CRBR12	I	...	16:26:17.3	-24:23:47	No	No	Yes	Yes	No
EL21	I	...	16:26:21.4	-24:23:06	No	No	Yes	Yes	No
GY91	I	...	16:26:40.5	-24:27:14	Yes	No	Yes	Yes	No
IRS43	I	...	16:27:26.9	-24:40:51	Yes	No	Yes	Yes	Yes
L1689S	I	...	16:32:00.8	-24:56:42	No	No	Yes	Yes	No
L1709B	I	...	16:31:35.8	-24:01:29	No	No	Yes	Yes	No

Table 4.1 cont.

Source Name	SED Class	Spectral Type	RA (hms)	Dec (dms)	X-ray Detection	Optical Detection	IR Detection	submm/mm Detection	radio Detection
LFAM26	I	...	16:27:05.4	-24:36:31	No	No	Yes	Yes	Yes
LFAM30	I	...	16:27:15.8	-24:38:44	No	No	Yes	Yes	Yes
YLW2	I	...	16:26:44.3	-24:34:47	No	No	Yes	Yes	No
YLW46A	I	...	16:27:37.3	-24:30:35	No	No	Yes	Yes	No
GY11	FS	M7	16:26:22.3	-24:24:09	No	No	Yes	No	No
L1719B	FS	...	16:22:04.4	-19:43:26	No	No	Yes	Yes	No
LFAM1	FS	...	16:26:21.7	-24:22:51	No	No	Yes	Yes	Yes
LFAM15	FS	...	16:26:42.4	-24:26:26	No	No	Yes	No	Yes
RNO91	FS	M1	16:34:29	-15:47:01	No	Yes	Yes	Yes	No
SR24	FS	K1	16:26:58.5	-24:45:37	No	Yes	Yes	Yes	No
AS205	II	K5	16:11:31.4	-18:38:26	Yes	Yes	Yes	Yes	No
DoAr25	II	K5	16:26:23.6	-24:43:14	Yes	Yes	Yes	Yes	No
DoAr44	II	K3	16:31:33.4	-24:27:37	Yes	Yes	Yes	Yes	No
EL24	II	K6	16:26:24.1	-24:16:13	Yes	Yes	Yes	Yes	Yes
EL27	II	K8	16:26:45.0	-24:23:08	Yes	Yes	Yes	Yes	Yes
Flying Saucer	II	...	16:28:13.7	-24:31:39	No	Yes	Yes	No	No
GSS26	II	K8	16:26:10.3	-24:20:55	Yes	Yes	Yes	Yes	No
SR4	II	K5	16:25:56.2	-24:20:48	Yes	Yes	Yes	Yes	No
SR21	II	G3	16:27:10.1	-24:19:15	Yes	Yes	Yes	Yes	No
WaOph6	II	K6	16:45:45.6	-14:16:36	Yes	Yes	Yes	Yes	No
YLW58	II	M4	16:28:16.6	-24:36:58	No	Yes	Yes	Yes	No

Table 4.1 cont.

Source Name	SED Class	Spectral Type	RA (hms)	Dec (dms)	X-ray Detection	Optical Detection	IR Detection	submm/mm Detection	radio Detection
GY10	III	M9	16:26:22.2	-24:23:54	No	No	Yes	No	No
GY12	III	...	16:26:22.4	-24:22:53	No	No	Yes	No	No
GY29	III	...	16:26:25.3	-24:24:45	No	No	Yes	No	No
GY306	III	M4	16:27:38.2	-24:30:43	No	No	Yes	No	No
ISO-Oph 26	III	M5	16:26:18.9	-24:24:14	No	No	Yes	No	No
BLKT J162736	?	...	16:27:36.0	-24:30:20	No	No	Yes	No	No
BLKT J162815	?	...	16:28:15.5	-24:36:46	No	No	Yes	No	No
BLKT J162818	?	...	16:28:18.1	-24:37:34	No	No	Yes	No	No
GY124	?	...	16:26:47.0	-24:23:05	No	No	Yes	No	No
GY294	?	...	16:27:35.1	-24:30:14	No	No	Yes	No	No
GY313	?	...	16:27:38.9	-24:30:25	No	No	Yes	No	No
LFAM4	?	...	16:26:25.7	-24:24:30	No	No	No	No	Yes
LFAM16	?	...	16:26:42.9	-24:22:59	Yes	No	Yes	No	Yes
LFAM29	?	...	16:27:14.7	-24:39:20	No	No	No	No	Yes
LFAM34	?	...	16:27:27.9	-24:40:34	No	No	No	No	Yes
SFAM127	?	...	16:31:59.5	-24:56:38	No	No	No	No	Yes

4.4 OVRO Observations

OVRO was a six element interferometer that was located in the Owens Valley in Southern California. Each of the OVRO dishes was 10.4m in diameter. Baselines from 15 to 220m were available on a straight track that the dishes could be moved along. These baselines translate to a maximum resolution of $2.5''$ in one direction, while structures larger the 37 arcsec are resolved out. Since the baselines are not arranged in an ordered 2-D grid the projected baseline differs in different directions. Therefore, the minimum beamsize is $2.4 \times 3.5''$, corresponding to $\sim 350 \times 510$ AU at 150 pc.

The OVRO observations were taken in 2004 between January and May during director time. All the observations had a central frequency of 90 GHz (~ 3.3 mm) and a bandwidth of 4 GHz. Most sources where observed multiple times during this period with each single observation track having a total time of ~ 5 hours. This track time was split between observing a strong quasar for bandpass calibrating, a planet for total flux calibrating, a secondary quasar for phase calibration, and the source. Absolute flux calibration performed using the planet resulted in uncertainties of $\sim 10\%$. The maps reached a roughly uniform sensitivity level of between ~ 1 mJy for sources with many tracks and ~ 2.5 mJy for sources with only one track.

Chapter 5

Data Reduction

Data were recorded at OVRO in the u - v plane as visibility amplitudes and phases for each pair of antennae. The data reduction was then performed using Miriad (Sault et al. 1995). The reduction process involves two key stages, the editing and calibrating stage and the mapping stage. Editing and calibration involves correcting the measured visibility amplitudes of a quasar to its known visibility amplitudes. This is done by creating a function, which when applied to the quasar data result in the measured visibilities becoming the known visibilities. These values for each u - v point are the gain solution and when applied to the source data, should return the true source visibilities.

The mapping stage involves Fourier inverting the calibrated visibilities to form a map of the source brightness distribution. However, since the data are not continuous in the u - v plane the Fourier inverted map is not a true representation of the source brightness. Therefore, the map must be deconvolved using the CLEAN algorithm before being reconvolved with a gaussian beam to produce the final map of the source brightness. This section sets out all the steps taken, after the data is recorded at the telescope to the generation of source maps. Figure 5.1 shows the data reduction steps in the order they are taken.

5.1 Editing and Calibration

5.1.1 Baseline Correcting

Before any calibration of data can be achieved the data must be corrected for changing baseline lengths. The baseline lengths affect the phase coherence of the interferometer, reducing its ability to produce useful maps. Wind and other effects can change the relative positions of antennae, therefore, the baseline lengths are monitored. If a dish has moved then this must be accounted for within the data but the antenna positions are not necessarily updated at the time of observation. Therefore, the baseline lengths must be checked and corrected in the first stage of data reduction.

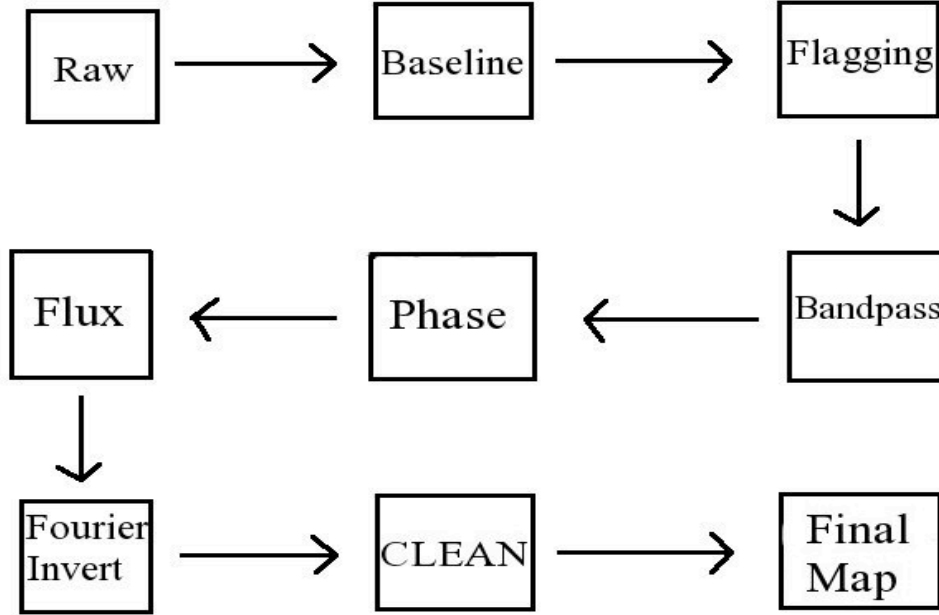


Figure 5.1: Flow diagram charting the steps made in getting the received visibilities into a map of the source brightness.

5.1.2 Data Inspection and Flagging

The final step before calibration involves inspecting the amplitudes and phases for any sections that are of too poor quality to use. This can be due to factors such as atmospheric turbulence or evolving receiver conditions. For example, at sunrise the wires carrying the signals expand slightly, which would in turn lower the phase coherence of the correlated data. Poor quality data are flagged and ignored in subsequent analysis. In order to determine which data need to be flagged, the u - v data from the high flux quasar observations are inspected. Good data will show a monotonic trend in phase and amplitude, which can be fit and applied to the source data. Bad data will have jumps in phase or amplitude between consecutive observations due to rapidly changing atmospheric conditions or system changes. Figure 5.2 shows an example of both good uncalibrated data and bad uncalibrated data. The sections of bad data are flagged and take no further part in the calibration procedure.

5.1.3 Bandpass Calibration

The receiver on each antenna has a slightly different response to the incident radiation across the bandwidth of observation. This change in response across the channels of the receiver needs to be quantified by measuring a strong flat spectrum source. Bandpass calibration is achieved by observing a strong quasar, > 1 Jy, for ~ 20 minutes at the start of each observing track. For the relatively narrow bandpass of each OVRO band the strong quasar will have the same flux across the observing bandwidth, so the measured

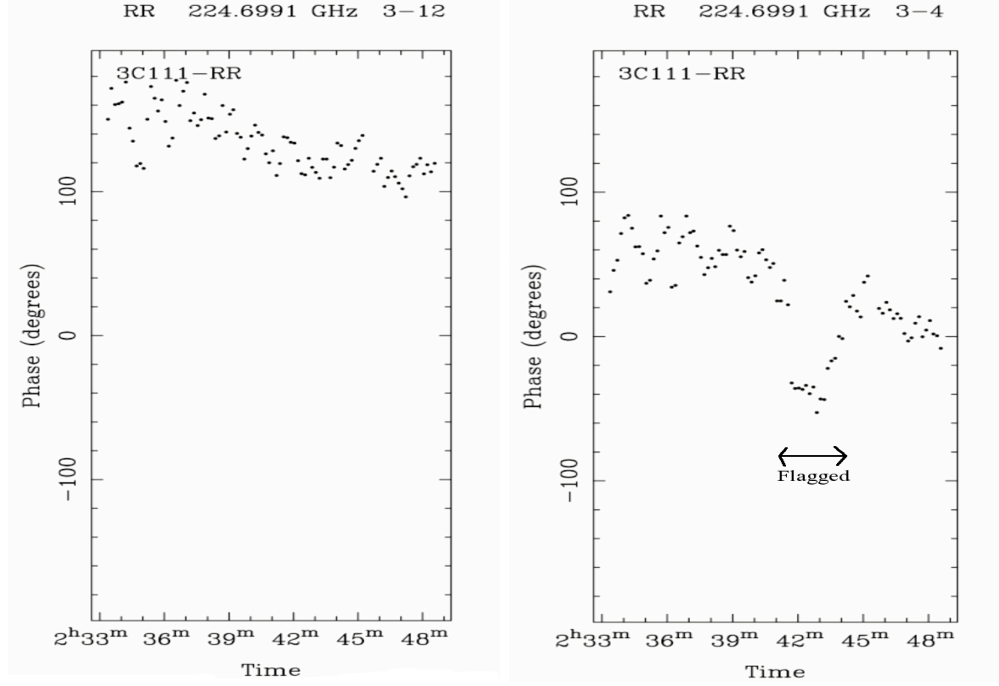


Figure 5.2: Left: Good uncalibrated data taken from one baseline of an observation of the quasar 3C111. The phase follows a clear trend. Right: Bad uncalibrated data taken from two baselines of an observation of the quasar 3C111. There is a jump in the phase between two sets of observations about three quarters of the way through this observation. This jump would mean the data for that section of time would not be calibrated correctly.

flux reveals any variations in sensitivity across the channels. The calibration generates a function that when divided with the visibility data flattens the observed amplitudes across the bandwidth.

5.1.4 Phase Calibration

The main stage of data calibration are phase and gain calibration for each baseline. This calibration is performed to recover the true visibilities, which due to effects such as atmospheric turbulence or receiver noise are not identical to the observed visibilities. In order to achieve this calibration a point source quasar, 0.5 Jy – 3 Jy, which is within 20° of the source is observed at ~ 20 minute intervals throughout the track. The true visibility of the quasar is known since it is a point source with known flux. Therefore, by comparing the measured quasar visibilities with the standard visibilities it is possible to create a solution, which when divided by the measured visibilities returns the known source visibilities. This accounts for the variation in the measured phases and amplitudes throughout the observations. The quasar gain solution is then applied to the source data to produce the true calibrated visibilities. Figure 5.3 shows a comparison of the calibrated phases to the uncalibrated phases of the quasar 3C111.

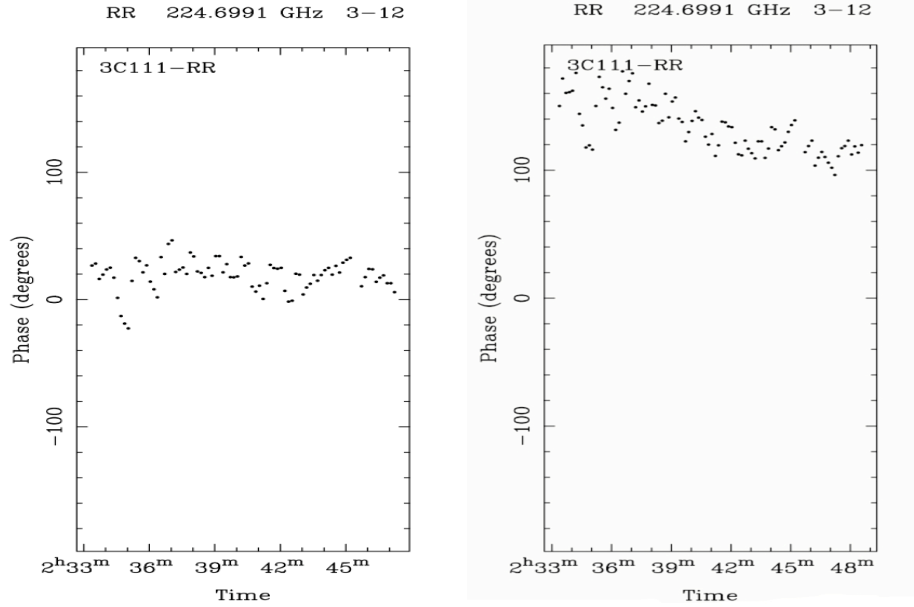


Figure 5.3: Left: Calibrated phase data taken from one baseline of an observation of the quasar 3C111. The phases are \sim flat with very little variation in time and with no longer term phase fluctuations. Right: Uncalibrated phase data taken from one baseline of an observation of the quasar 3C111. The phases have a long term gradient and are not centred around zero.

5.1.5 Flux Calibration

The final step in the data calibration is bootstrapping the absolute flux of the observed calibrator to the observed visibility amplitudes. The strong calibrators observed for phase and gain calibration have known fluxes at the time of observation. Therefore, while calibrating the gains they are not only flattened through the time of the observation they are also flattened around the known amplitude of the quasar. Appendix A shows a reduction script created for calibrating interferometry data.

5.2 Mapping

To produce a source intensity map from the u - v data, a Fourier inversion is performed. This is not a simple Fourier transform as not all points in u - v space are sampled.

5.2.1 Fourier Inversion

The discrete nature of the u - v points sampled must be accounted for during the process of recovering the source brightness distribution from the calibrated visibility data. This involves defining a weighting function that is equal to 0 wherever there is not a u - v visibility point. The weighting function affects both the size of the beam and the sensitivity of the observations. The two extremes of weighting functions are natural and uniform weighting functions. A natural weighting function gives each point the same weight, that is all points

are treated as equal when Fourier inverted. This weighting emphasises the shorter u - v spacings as there are more short u - v spacings sampled. This has the effect of maximising the signal to noise of the interferometer but natural weighting also increases the beam size. The second weighting function is a uniform weighting function, whereby weights are determined by the number of other sampled u - v points within a symmetric region around the current point. The more u - v points around the current point, the lower the weight it is given. This weighting emphasises the longer u - v spacings, since there are far fewer long spacings sampled. Therefore, by putting more weight on the larger spacings uniform weighting results in a smaller beam size but lower signal to noise.

Once the weighting of the visibility points has been established it is still important to account for their irregular sampling. The irregularly sampled data could be directly Fourier transformed to produce an image but this is extremely computationally expensive. Therefore, fast Fourier transform algorithms are used in order to greatly reduce the number of arithmetical operations required. These algorithms do this using regularly gridded data, with each cell then directly Fourier transformed separately. Therefore, the irregularly sampled u - v points must be resampled onto a grid. The size of each cell of the grid, when Fourier transformed, is the pixel size, while the number of grid cells determines the size of the resultant image. The effects of gridding also include creating a periodic image, where the central maximum is repeated near the edge of the image. This unwanted effect creates apparent sidelobes in the image, which need to be removed. The image that comes from the fast Fourier transform algorithm is hence known as the dirty image due to these contaminants. An example of a dirty image is shown in Fig. 5.4.

5.2.2 Deconvolution

In order to progress from the dirty image to the final representation of the source brightness the iterative CLEAN algorithm is applied to the map. In each iteration, CLEAN searches for the peak of intensity then records its strength and position on an initially blank model map. This source is then removed from the dirty map and the process begins again. Usually, only the portion of the image around where the source is expected to be detected is cleaned, in order to remove the unwanted sidelobes in the dirty image. CLEAN builds up a series of point sources in the model map with a point source represented by one pixel. This process continues until the original dirty map, now devoid of all strong point sources, has an rms similar to the rms noise expected for the observation. An example of a CLEAN model map is shown in Fig. 5.4.

The final step in generating the source map is a convolution of the CLEAN model pixel map with a Gaussian beam. This convolution is performed in order to remove the artificial enhancement in the resolution of the image due to the CLEANing process. An example of a final map is shown in Fig. 5.4. The final maps in this survey were created using the script shown in Appendix A.

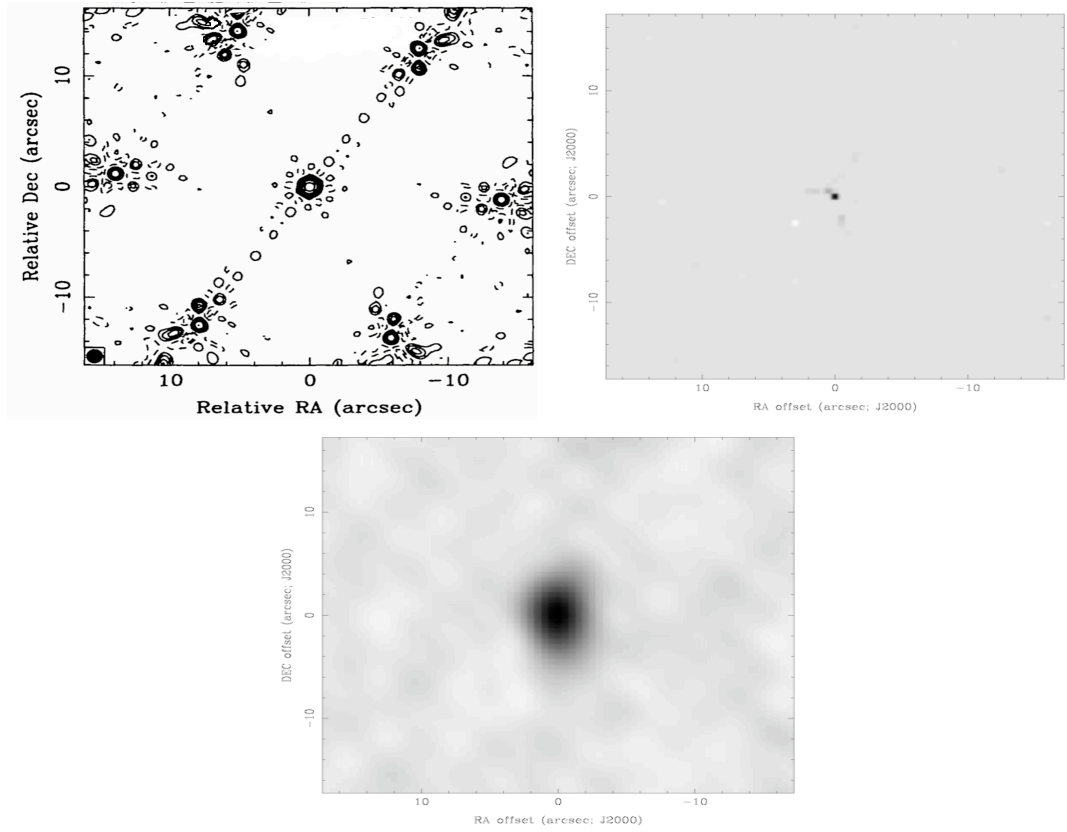


Figure 5.4: Example of the products of the three stages of taking calibrated u - v data into making a map of a source. Top Left: An example dirty image of a strong source, the sources in this survey are not strong enough to produce obvious sidelobes. In this map they are clearly visible at six points towards the edge of the map. Top Right: The CLEAN map of one of my sources. Bottom: The final map after the CLEAN model map has been convolved with a gaussian beam.

Chapter 6

OVRO 3mm Fluxes & Upper Limits

Of the 60 sources observed in this survey, 28 were detected, 31 had upper limits placed on their total flux values and one source observation failed. For this study the upper limits placed on peak fluxes are three times the rms noise level of the source map. The 28 detections results in an overall detection frequency of 47%, not including the failed observation. The detection frequency also changes through the evolutionary phases, as seen in the left hand side of Fig. 6.1. We would have expected to detect all Class 0 through to Class II objects, yet there is a significantly reduced detection frequency for the Flat Spectrum sources. This is perhaps due to misclassification or possibly due to the dust having a higher than expected dust opacity index. The brightest detected source is IRAS16293B, a Class 0 object, with a flux of 209.8 mJy, while the faintest detected source is the the Flying Saucer, a Class II object, with a flux of only 2.74 mJy. There is also a trend of mean flux with evolutionary phase, the Class 0 objects show very high fluxes compared to the other sources. The other evolutionary phases have similar mean fluxes. These mean fluxes were calculated using the Kaplan-Meier limit estimator method to account for the upper limits (Feigelson & Nelson 1985). The trend in evolutionary phase is seen in the right hand side of Fig. 6.1.

As well as the great sensitivity afforded by OVRO the increased resolution since they are interferometric observations allowed 12 of these sources to be spatially resolved. There appeared to be no correlation between evolutionary class and whether the emission was resolved or the size of the resolved object, except for the Class 0 sources where all of which were resolved. The deconvolved angular sizes ranged from 1.13×0.81 , corresponding to $\sim 160 \times 115$ AU at 140 pc, to 15.1×1.7 , corresponding to $\sim 2100 \times 240$ AU at 140 pc. Notes on individual objects are given by class, while Appendix B contains tables of literature data for the sources.

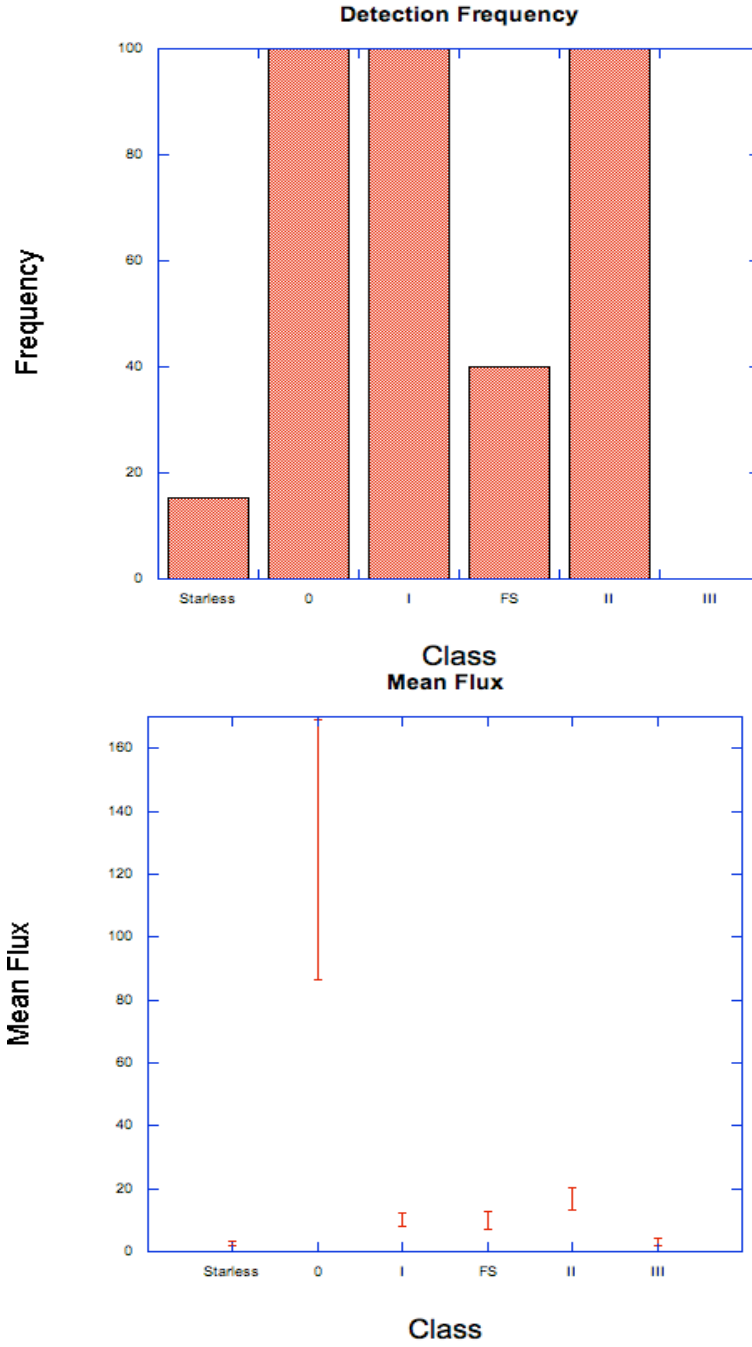


Figure 6.1: Top: A graph of detection frequency against evolutionary phase. The starless objects are not easily detected, while this survey detects all Class 0, I and II sources but there is a drop out of Flat Spectrum sources. None of the Class III sources observed have been detected. Bottom: A graph of mean flux against evolutionary phase. The starless objects do not have very high fluxes, perhaps as dust is resolved out by the interferometer. There is a clear peak in flux at the Class 0 stage, with the fluxes fairly constant through to the Class III stage.

6.1 Starless

There were 13 starless objects included in this survey, of which 2 were detected in 3.3 mm continuum. The fluxes of starless detections are given in Table 6.1. Contour maps created

of the two detected sources are shown in Fig. 6.2. It is possible that due to the extended nature of the starless cores some of the emission will be resolved out by an interferometer.

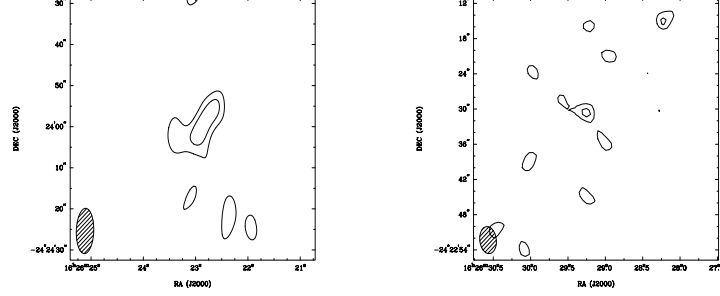


Figure 6.2: Maps of the starless sources, A-MM2 (also containing A-MM1 and A-MM3) and A-MM7. Contour levels are 2-5 times the RMS level of the individual images. The beam size of each map is shown.

Source Name	3mm Peak Flux [mJy]	3mm Total Flux [mJy]	Map Noise [mJy]	Calibration Uncertainty [mJy]	Source Size ["]
A-MM1	< 5.3	-	2.5	0.5	-
A-MM2	9.5	12.8	2.5	1.3	15.1 x 1.7
A-MM3	<7.0	-	2.5	0.7	-
A-MM7	2.4	4.3	1.3	0.4	13.7 x 0.9
A-S	<1.7	-	1.9	0.1	-
A3-MM1	<2.5	-	0.9	0.2	-
B2-MM7	<4.2	-	1.6	0.4	-
B2-MM8	<4.2	-	1.6	0.4	-
B2-MM10	<4.3	-	1.6	0.4	-
B2-MM14	<2.8	-	0.9	0.3	-
B2-MM15	<3.2	-	0.9	0.3	-
B2-MM16	<1.4	-	0.9	0.1	-
B2-MM17	<2.7	-	1.1	0.3	-

Table 6.1: Table containing the recovered fluxes and upper limits for the starless objects.

6.1.1 A-MM1, A-MM2, A-MM3

These three sources have only been observed at two previous wavelengths and were first detected by the 1.3 mm survey of Motte et al. (1998). The strongest of these three is A-MM2, with a 1.3 mm flux of 90 mJy, which is also the only of the three detected in this survey, with a flux of 12.8 mJy. All three sources were unresolved by Motte et al. (1998). However, this survey has allowed A-MM2 to be resolved with a size of $\sim 2100 \times 240$ AU. The position angle of the deconvolved size indicates the source is stretched in the direction of A-MM1 and A-MM3. These three sources are grouped closely enough that they were all within one beam size in the 1.2 mm survey of Stanke et al. (2006), which quoted an integrated flux of 964 mJy for the three sources.

6.1.2 A-MM7

This source was detected in this survey with a flux of 4.3 mJy, with a resolved size of $\sim 1900 \times 130$ AU. It also has a bright detection of 110 mJy in the survey of Motte et al. (1998), they also resolved the source to an extent of 1400×1400 AU. This discrepancy relative to the work of Motte et al. (1998) could be due to the fact the clump lies along the photo-dissociation front of a nearby B star. It is also detected by the survey by Stanke et al. (2006) with an integrated flux of 3137 mJy.

6.1.3 Non-Detected Sources

The remaining starless sources all have 1.3 mm detections by Motte et al. (1998). However, they have not been detected in this survey and upper limits ranging from 1.4 to 7.0 mJy are placed on their flux.

6.2 Class 0

Two Class 0 sources were included in this survey and both were detected with a high signal to noise. These two sources are binary systems, with these observations only resolving one of the two systems into its two components. The fluxes of the Class 0 objects are likely to arise mainly from envelope material, although due to their extended nature it is possible some of the flux is resolved out. The fluxes of the Class 0 detections are given in Table 6.2, while maps are shown in Fig. 6.3.

Source Name	3mm Peak Flux [mJy]	3mm Total Flux [mJy]	Map Noise [mJy]	Calibration Uncertainty [mJy]	Source Size ["]
IRAS16293A	74.3	100.2	3.2	10.0	6.9 x 1.8
IRAS16293B	190.7	225.7	3.2	22.6	1.8 x 0.9
LFAM5	39.9	57.7	1.9	5.8	4.9 x 2.4

Table 6.2: Table containing the recovered fluxes for the Class 0 objects.

6.2.1 IRAS16293

IRAS16293 is the most studied of all my sources, having been observed from $3.6 \mu\text{m}$ to 20 cm, it has also been the subject of molecular line studies to search for outflows. It is a binary with a separation of $5''$, which is ~ 700 AU at 140 pc (Wootten 1989). The work of Loinard (2002) suggests it may be a triple system with the A component being a subarcsecond binary. These data partially resolve the two main components of the system. IRAS16293A has a resolved size of $6.9'' \times 1.8''$, which corresponds to ~ 950 AU \times 250 AU at the distance of 140 pc. This seems too large to be resolving the disk of the system but too small to be resolving the large envelope. It is likely that contamination from the stronger IRAS16293B is causing the deconvolution to stretch in the direction of this

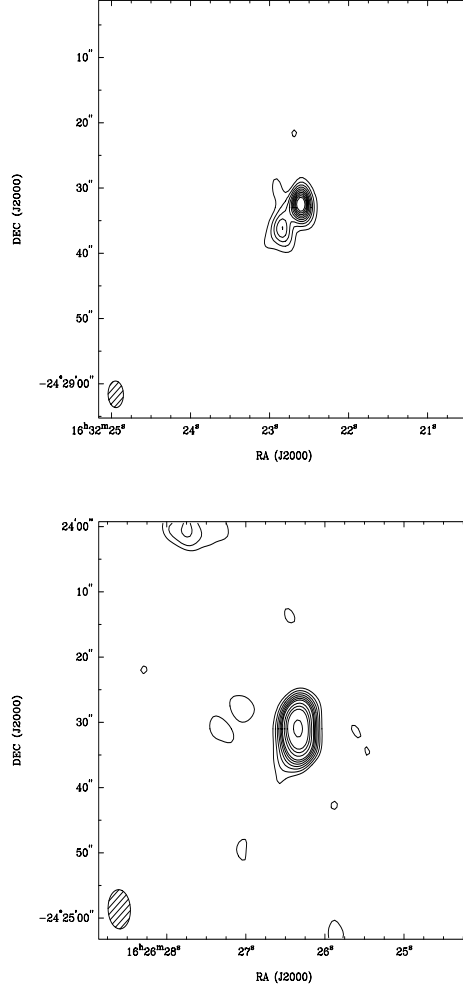


Figure 6.3: Maps of the two class 0 sources, top is IRAS16293 and bottom is LFAM5. Contour levels for IRAS16293 they are 5,10,15,20,25,30,35,40,45,50 times the RMS of the map. While for LFAM5 are 2-8 then 10,12,14,20,25,30 times the RMS level of the map. The beam size of each map is shown.

source. IRAS16293B has a resolved size of 250 AU x 125 AU at 140 pc, which is likely to represent the size of the disk.

IRAS16293 is also known to drive two molecular outflows, one E-W and the other NE-SW. The source is undetected at near-IR wavelengths with the first detection of the object at $8\mu\text{m}$. At mid and far-IR wavelengths the source was detected by IRAS from $25\mu\text{m}$ to $100\mu\text{m}$ and ISOCAM from $50\mu\text{m}$ to $190\mu\text{m}$. The source is detected at sub-millimeter and millimeter wavelengths, indicating large amounts of cold dust are present. This source has no previous 3.3 mm flux measured. This survey attributes a 3.3 mm total integrated flux of 100.2 mJy for IRAS16293A and 225.7 mJy for IRAS16293B. The source also has fairly strong centimetre emission (Estalella et al. 1991). It is therefore possible that some of the flux from this source arises from free-free emission. However, at most ~ 10 mJy and it is therefore neglected. If this were included the measured flux arising from

dust would decrease. During the mapping of the source, uniform weighting was used in order to enhance the resolution, and resolve the pair.

6.2.2 LFAM5

LFAM5 or VLA1623 is the prototype Class 0 pre-stellar object as classified by Andre et al. (1993). It is a binary system with a separation of just over $1''$; these observations fail to resolve the pair. The circumstellar material around the source is detected with a total integrated flux of 57.7 mJy and is resolved by OVRO with a size of $4.9'' \times 2.4''$. At the ρ Ophiuchus distance of 140 pc this corresponds to $\sim 680 \text{ AU} \times 335 \text{ AU}$, which is possibly the size of the circumbinary disk in the system. LFAM5 is also known to drive a molecular outflow in the NW-SE direction (Dent et al. 1995). This source has only one detection below a wavelength of $350 \mu\text{m}$, a faint $24 \mu\text{m}$ detection with Spitzer. The source had previously only been studied up to 2.7 mm. Therefore, this survey extends the Submm/mm SED of the source further into the region where we can be certain the emission is optically thin. Due to this source's weak 6 cm detection we also know that very little of the flux is due to free-free emission.

6.3 Class I

All the Class I objects in the survey were detected. The observed Class I source fluxes are likely to arise from a combination of both disk and envelope material. Therefore, it is possible some of the flux of these objects is resolved out by these interferometric observations. The fluxes of the Class I objects are shown in Table 6.3. Contour maps created of all the sources are shown in Figs. 6.4 and 6.5.

Source Name	3mm Peak Flux [mJy]	3mm Total Flux [mJy]	Map Noise [mJy]	Calibration Uncertainty [mJy]	Source Size ["]
CRBR12	9.4	9.4	1.1	0.9	Point
EL21	9.8	9.7	1.9	0.9	Point
GY91	6.6	7.3	0.8	0.6	3.9 x 1.9
IRS43	7.4	4.2	2.0	0.7	Point
L1689S	6.9	4.4	1.4	0.7	Point
L1709B	31.7	31.2	1.2	3.2	Point
LFAM26	3.8	4.9	1.2	0.5	4.2 x 2.7
LFAM30	7.6	6.9	1.3	0.8	Point
YLW2	11.5	7.2	1.9	1.2	Point
YLW46A	5.2	4.3	1.2	0.5	Point

Table 6.3: Table containing the recovered fluxes for the Class I objects.

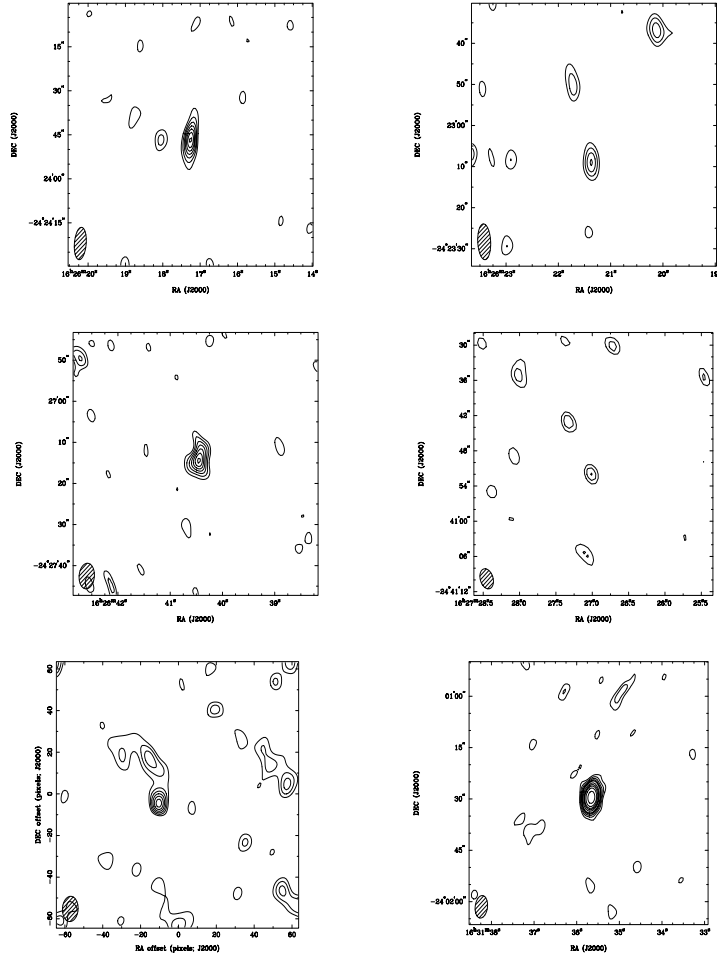


Figure 6.4: Maps of the Class I sources, from top left CRBR12, EL21, GY91, IRS43, L1689s and L1709b. Contour levels are 2-12 times the RMS level of the individual maps for the first 5 while they are 2-6,8,10,12,15,20 for L1709b. Note: We do not believe the extended nature of L1689S is real simply that it is an artifact of the imaging process. The beam size of each map is shown.

6.3.1 CRBR12

This survey detects CRBR12 as a point source with a flux of 9.4 mJy. CRBR12 has been detected from the near-IR H band up to this surveys detection at 3.3 mm. This system is a possible spectroscopic binary system, which would have a separation of only ~ 5 AU (Covey et al. 2006). This source has no centimetre detection indicating that free-free emission is not a large contributor to the measured flux at 3.3 mm. Andrews & Williams (2007a) used the 1.3 mm detection of Andre & Montmerle (1994) to calculate a dust mass of $0.02 M_{\odot}$ for this source, there is no previous β measurement.

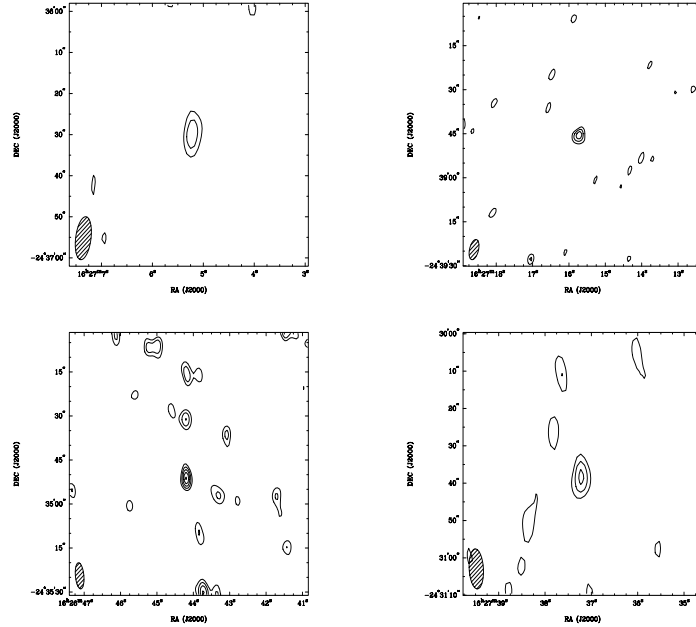


Figure 6.5: Maps of the Class I sources, from top left LFAM26 LFAM30, YLW2, and YLW46. Contour levels are 2-12 times the RMS level of the individual maps.

6.3.2 EL21

EL21 is unresolved in these data and has a flux of 9.8 mJy. This source has detections ranging from the near-IR J band to the 3.3 mm detection in this survey. Very high resolution near-IR imaging reveals that this source may be a binary system with a separation of 0.15'' (Chen et al. 2007). Andrews & Williams (2007a) find this source to have a dust mass of $0.01 M_{\odot}$, with a β of 0.5.

6.3.3 GY91

This source is detected with a total integrated flux of 7.3 mJy and has a deconvolved size of $3.9'' \times 1.9''$. This size corresponds to $\sim 540 \text{ AU} \times 260 \text{ AU}$, which is likely to correspond to the disk in the system. GY91 is a single star, which has been detected from J band to the detection in this survey. As well as these detections, this source is also known to be a strong X-ray emitter (Gagné et al. 2004). The current calculated dust mass is $0.06 M_{\odot}$ (Andrews & Williams 2007a), there is no previous β measurement.

6.3.4 IRS43

IRS43 has a flux of 7.4 mJy and is unresolved in this survey. It is a triple system with separations of 6.99'' and 0.6'' (Haisch et al. 2002; Girart et al. 2000). It has been detected at wavelengths from the J band to 6 cm, as well as being a bright X-ray source. IRS43 is a strong emitter at centimetre wavelengths indicating possibly all of the flux at 3.3 mm could arise from free-free emission. This source has a spectral type of K5. This source

previously has been observed at 3 mm and found to have a β of 1.3, with a dust mass of $0.02 M_{\odot}$ (Patience et al. 2008).

6.3.5 L1689S

This source is one of the few YSO's discovered in the L1689 cloud in Ophiuchus and is a single system. It is detected as an unresolved point source with a peak flux of 6.9 mJy in these data. It has previously been detected from the J band to the 1.3 mm. The survey of Andrews & Williams (2007a) calculated a dust mass of $0.02 M_{\odot}$, with a β of 0.28.

6.3.6 L1709B

L1709B is a single system in the L1709 cloud in Ophiuchus. It was unresolved by OVRO and had a peak flux of 31.7 mJy. The source has been detected from the J band to 3.3 mm. Previous derivations of the dust mass, $0.06 M_{\odot}$, and β , 0.28, were made by Andrews & Williams (2007a).

6.3.7 LFAM26

LFAM26 was detected with a total integrated flux of 4.9 mJy, it was also resolved to a size of $4.2'' \times 2.7''$. This size corresponds to $\sim 585 \text{ AU} \times 380 \text{ AU}$ at 140 pc, which is likely to be the disk of the system, although it would represent a large scale disk. This source is a single system, which has been detected at wavelengths from the K band to 6 cm. The centimetre detection is a weak detection, meaning free-free emission is not likely to be a large contributor to the measured 3.3 mm flux. A previous estimate of the dust mass was $0.02 M_{\odot}$ but there are no previous estimates of β (Andrews & Williams 2007a).

6.3.8 LFAM30

This source is a triple system that contains two Class II sources and one Class I source. LFAM30 is separated from the other components by $\sim 2.3''$ and $3.7''$ (Ressler & Barsony 2001), all within the beam size of these observations. These observations detect the source with a peak flux of 7.6 mJy but fail to resolve the material around LFAM30. All three sources in this system have been observed from J band to $20 \mu\text{m}$ with LFAM30 being very weak in the near-IR. Above $20 \mu\text{m}$ only the Class I source has been detected including the 3.3 mm observation in this survey. This source was part of the survey of Andrews & Williams (2007a) and was found to have a disk mass of $0.01 M_{\odot}$, with a β of -0.61. There is also a centimetre detection of this source. However, as it is a weak detection free-free emission should not represent a large portion, $\sim 5\%$, of the measured flux at 3.3 mm.

6.3.9 YLW2

YLW2 was detected, but unresolved, with a peak flux of 11.5 mJy by these observations. It is a single YSO that has been detected from the J band to the 3.3 mm detection of this

survey. This source also has a strong X-ray detection (Gagné et al. 2004). In the survey of Andrews & Williams (2007a) a dust mass of $0.01 M_{\odot}$ and a β of 0.00 were calculated.

6.3.10 YLW46A

YLW46A is part of a binary system with a Class III system that has a separation of $\sim 1.5''$ (Haisch et al. 2006). It was detected with a peak flux of 5.2 mJy and was unresolved in these observations. This source has been detected at wavelengths from the J band to the 3.3 mm detection in this survey. The calculated dust mass from Andrews & Williams (2007a) is $0.01 M_{\odot}$, while β is -0.09.

6.4 Flat Spectrum

Of the 6 flat spectrum sources only 2 were detected. One of the sources, SR24, had particularly bad phase coherence from the observations due to bad weather and is omitted from the future analysis. This source is only included here for completeness. It is also possible both GY11 and LFAM15 are classified incorrectly, as neither has a previous submm/mm detection. The fluxes of the Flat Spectrum objects are shown in Table 6.4. Contour maps created of all the sources are shown in Fig. 6.6.

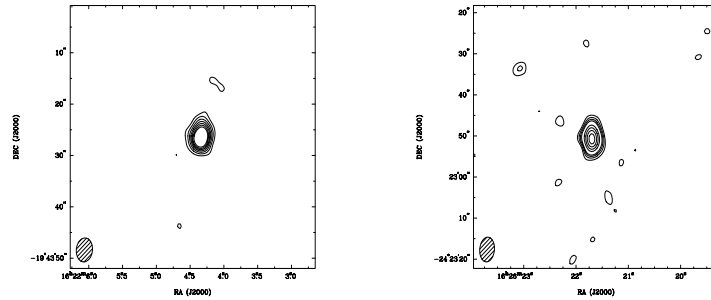


Figure 6.6: Maps of the Flat Spectrum sources, left is L1719B and right is LFAM1. Contour levels are 2,3,4,5,8,10,12,14,16,18 times the RMS level of the individual images. The beam size of each map is shown.

Source Name	3mm Peak Flux [mJy]	3mm Total Flux [mJy]	Map Noise [mJy]	Calibration Uncertainty [mJy]	Source Size ["]
GY11	<4.8	-	2.5	0.5	-
L1719B	17.2	17.3	0.7	1.7	1.1 x 0.8
LFAM1	18.9	18.7	1.0	1.9	Point
LFAM15	<5.1	-	1.9	0.5	-
RNO91	<4.9	-	1.5	0.5	-
SR24	<66.4	-	31.6	6.6	-

Table 6.4: Table containing the recovered fluxes and upper limits for the Class FS objects. SR24 was the source with the failed observation.

6.4.1 L1719B

L1719B is a single YSO in the L1719 cloud of Ophiuchus. This source was detected with a total integrated flux of 17.3 mJy with a resolved size of $1.1'' \times 0.8''$. This size corresponds to $\sim 150 \text{ AU} \times 110 \text{ AU}$, which is likely to correspond to the disk. It has been detected from the R band to the 3.3 mm detection of this survey. However, this source has only one previous Submm/mm detection, at 1.3 mm, from Andre & Montmerle (1994). The source is on the border between Class I and Flat Spectrum, referred to as Class I by Andre & Montmerle (1994) but FS by Andrews & Williams (2007a). The literature values for β and dust mass are 0.28 and $0.06 M_{\odot}$ respectively (Andrews & Williams 2007a).

6.4.2 LFAM1

LFAM1 is a binary system with a wide, $9.4''$, Class III companion, GY12. These observations indicate the source has a peak flux of 18.9 mJy, and fail to resolve the material. The source has been detected from the K band to a wavelength of 6 cm. The system is believed to harbour an edge-on disk due to its resolved shape in the IR (Duchêne et al. 2007). The weak 6 cm emission indicates free-free emission is unlikely to contribute greatly to the measured flux at 3.3 mm. This source has a calculated dust mass of $0.04 M_{\odot}$ and a β of 0.18.

6.4.3 Non-Detected Sources

Both GY11 and LFAM15 are possibly in the wrong class. GY11 has no detection above $24 \mu\text{m}$ but its near-IR spectra indicates a Class II source Alves de Oliveira & Casali (2008). It is possible, since this is a very low mass Brown Dwarf (spectral type = M7), that the disk is very small due to its method of formation. LFAM15 is described as a Flat Spectrum object by Andrews & Williams (2007a). However, other surveys list this source as a Class III source. This source has not been detected between the wavelengths of $80 \mu\text{m}$ to 3.6 cm, indicating that cold dust emission does not play a significant part in the spectrum of this source.

The source RNO91 has been detected from V band out to a wavelength of 1.3 mm and was expected to be detected in this survey. The non-detection at 3.3 mm possibly indicates an abnormally high β value for this source. Previous measurements of β for this source are 0.64 (Andrews & Williams 2007a), this value of β should result in this source being detectable at 3.3 mm. Therefore, it is possible that the shorter wavelength observations of this source contain some contamination from optically thick emission. This source also powers a CO outflow (Mathieu et al. 1988).

Bad weather during the observation of SR24 make the upper limits established here very poor. Therefore, as stated previously the analysis of this source is not taken any further.

6.5 Class II

All the Class II sources in this survey were detected and it is believed that the fluxes arise from the circumstellar disk, with no extended envelope. The lack of an envelope would mean that no emission should be resolved out. The fluxes of the Class II objects are shown in Table 6.5. Contour maps created of all the sources are shown in Figs. 6.7 and 6.8.

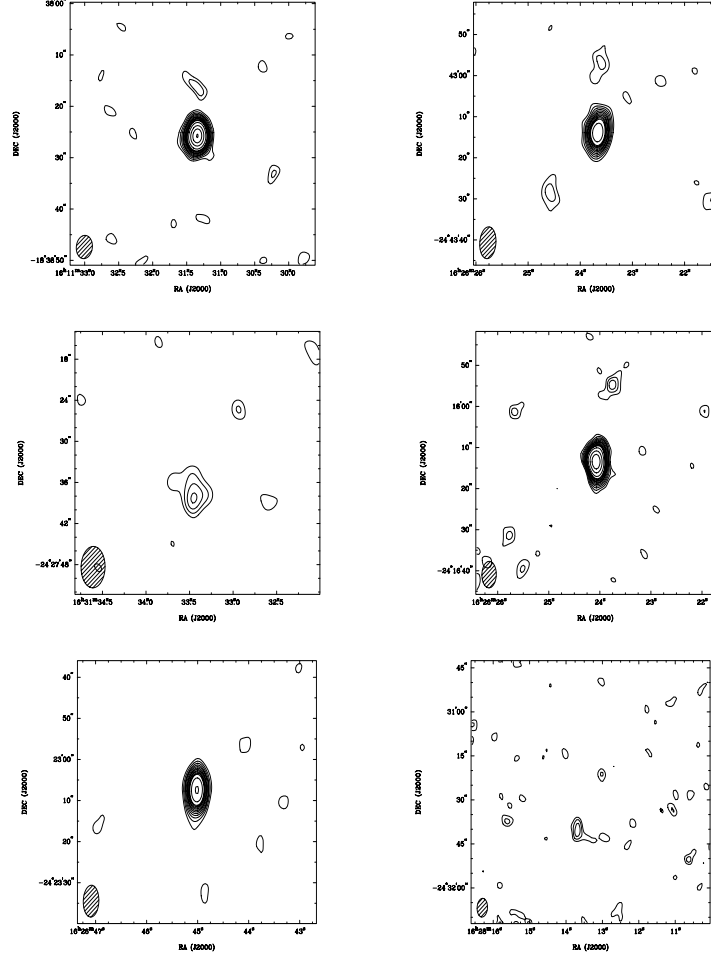


Figure 6.7: Maps of the class II sources, from top left AS205, DoAr25, DoAr44, EL24, EL27 and Flying Saucer. Contour levels are 2-12 times the RMS level of the individual images, except for DoAr25, AS205, EL24 which are 2-12,15,20,25,30. The beam size of each map is shown.

6.5.1 AS205

AS205 is a triple system with a separation of $1.3''$ (Ghez et al. 1993) between AS205A and AS205B, while AS205A is also be a spectroscopic binary (Melo 2003). AS205A has a spectral type of K5 Cohen & Kuhl (1979). It was detected with a total integrated flux of 35.8 mJy by these observations and was resolved to be $2.3'' \times 1.2''$ in size. This size corresponds to $\sim 320 \text{ AU} \times 170 \text{ AU}$ at 140 pc and is likely to represent a circumbinary disk

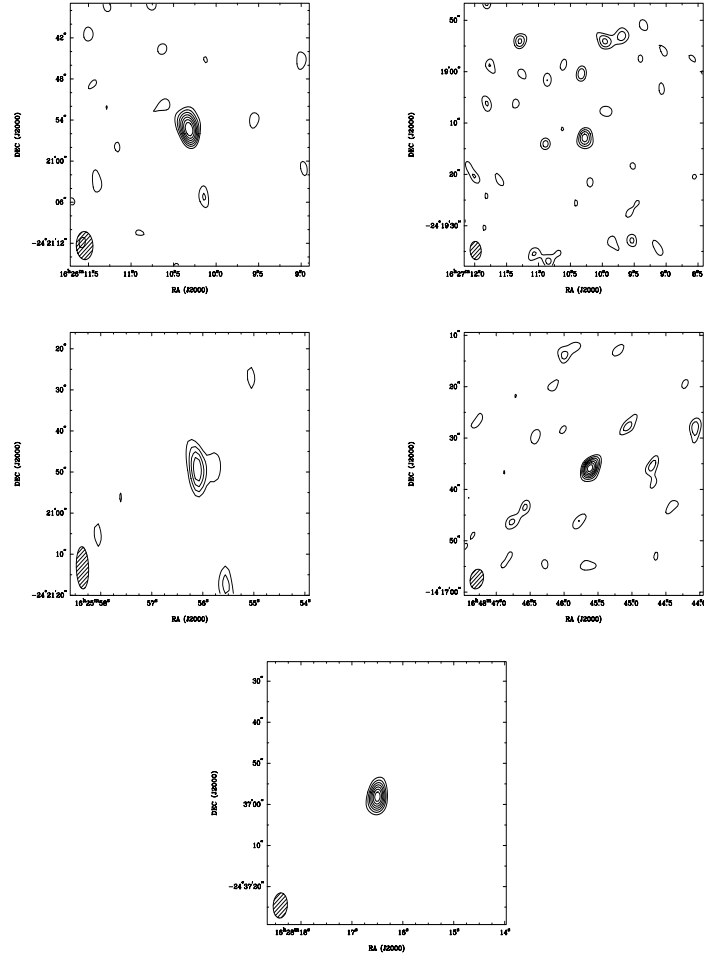


Figure 6.8: Maps of the class II sources, from top left GSS26, SR21, SR4, WAOph6 and YLW58. Contour levels are 2-12 times the RMS level of the individual images, except for GSS26 which are 2-16. The beam size of each map is shown.

Source Name	3mm Peak Flux [mJy]	3mm Total Flux [mJy]	Map Noise [mJy]	Calibration Uncertainty [mJy]	Source Size ["]
AS205	31.2	35.8	1.0	3.6	2.3 x 1.2
DOAR25	21.6	21.8	1.0	2.2	Point
DOAR44	5.3	6.4	1.1	0.6	Point
EL24	35.1	37.2	1.2	3.7	2.6 x 0.9
EL27	26.4	27.3	1.2	2.7	3.5 x 0.6
Flying Saucer	2.7	3.0	0.7	0.3	Point
GSS26	18.8	15.2	2.1	1.5	Point
SR21	3.7	2.9	0.8	0.3	Point
SR4	7.8	12.4	1.2	1.2	4.8 x 2.4
WAOph6	14.7	11.6	1.6	1.1	Point
YLW58	11.8	11.2	0.8	1.1	Point

Table 6.5: Table containing the recovered fluxes for the Class II objects.

around AS205. This source has been detected from the optical U band to a wavelength of 3.3 mm in this study. It also has strong X-ray and centimetre detections. With only one centimetre wavelength observed it is difficult to extrapolate the free-free flux at 3.3 mm. It is possible that the free-free emission contributes as much as 10 mJy to the measured flux at 3.3 mm. However, it is not accounted for further. Andrews & Williams (2007a) calculate a β of -0.15, with a system dust mass of $0.03 M_{\odot}$.

6.5.2 DOAR25

DOAR25 was detected with a peak flux of 21.6 mJy and remained unresolved. It is a single system, which has been detected from the optical B band to the 3.3 mm detection in this survey. The system has a surprisingly low accretion rate of only $10^{-10} M_{\odot} \text{yr}^{-1}$ given its strong detection at Submm/mm wavelengths (Natta et al. 2006). This hints that the inner disk of this system is at an advanced stage of evolution (Andrews et al. 2008). This source has a K5 spectral type (Willing et al. 2005). The survey of Andrews & Williams (2007a) calculated a β value of -0.83 and a dust mass of $0.03 M_{\odot}$ for this source. The source also has an X-ray detection (Montmerle et al. 1983).

6.5.3 DOAR44

DOAR44 has a peak flux 5.3 mJy but is unresolved by these observations. This source is a single system, which has been detected from the B band to the 3.3 mm detection of this survey. The source also has an X-ray detection (Montmerle et al. 1983). The current value of β is -0.72, while the dust mass is $0.01 M_{\odot}$ (Andrews & Williams 2007a).

6.5.4 EL24

EL24 was resolved by OVRO with a size of $2.6'' \times 0.9''$, which corresponds to $\sim 360 \text{ AU} \times 125 \text{ AU}$. This source had a total integrated flux of 37.2, which made it the strongest non-Class 0 source in the survey. It is a single YSO of spectral type K6 (Willing et al. 2005). It has previous detection ranging from B band to 1.3 mm, with this survey extending that to 3.3 mm. This source also has a strong X-ray detection (Gagné et al. 2004). The literature value for β is -0.01, while the calculated dust mass is $0.2 M_{\odot}$ (Andrews & Williams 2007a).

6.5.5 EL27

This source was detected with a total integrated flux of 27.3 mJy and was also resolved by OVRO with a size of $3.5'' \times 0.6''$. This size results in a derived physical size of $\sim 490 \text{ AU} \times 80 \text{ AU}$, this indicates this system is likely to be near-edge on due to the difference between its major and minor axes when resolved. This is also indicated because unlike most of the Class II sources in this survey EL27 has no optical detection; only detected in J band to this survey's wavelength of 3.3 mm. An edge on disk would obscure the star the optical resulting in no detection. It is a K8 spectral type star (Luhman & Rieke 1999). This source also has an X-ray detection with a very weak centimetre detection (Gagné et al.

2004; Leous et al. 1991). Prior to this work, literature value for β were 0.07, while dust mass was $0.04 M_{\odot}$ (Andrews & Williams 2007a).

6.5.6 Flying Saucer

This survey detects the Flying Saucer for the first time at millimetre wavelengths. There currently exist no literature data on this source above $24 \mu\text{m}$, having previously been detected from B band to $24 \mu\text{m}$. The source is detected with a peak flux of only 2.7 mJy and is the faintest source in this survey. It is also unresolved even with the high resolution available with OVRO. Therefore, these fluxes also provide the first estimate of dust mass around this object. The work of Grosso et al. (2003) shows that the Flying Saucer has an edge on disk.

6.5.7 GSS26

GSS26 was detected with a peak flux of 18.8 mJy and is unresolved by these observations. It is a single YSO of spectral type K8 (Barsony et al. 2005). This is the only other Class II source that does not have an optical detection, having been detected from J band to the 3.3 mm detection in this survey. GSS26 also has an X-ray detection (Gagné et al. 2004). Andrews & Williams (2007a) calculate a β value of -0.35 and a dust mass of $0.04 M_{\odot}$ for this object.

6.5.8 SR21

SR21 is a binary system with a separation of $6.3''$ (Reipurth & Zinnecker 1993). It was detected with a peak flux of 3.7 mJy and was unresolved. As it is unresolved there is likely to be no circumbinary disk in this system as given the separation of the binary elements a circumbinary disk would likely be resolved. The primary has a spectral type of G3 (de Geus et al. 1989), the earliest spectral type of the objects in this survey. This source has previously been detected from B band to 3 mm, with this survey adding a 3.3 mm detection. Both components of SR21 have detected X-ray emission (Gagné et al. 2004). This source has a low accretion rate and is classified at a WTTS, even though it is a Class II source (Patience et al. 2008). The value of β calculated by Andrews & Williams (2007a) is 0.27, while their calculated dust mass is $0.03 M_{\odot}$.

6.5.9 SR4

SR4 is a single YSO of spectral type K5 and is a CTTS (Guenther et al. 2007). It was detected with a total integrated flux of 12.4 mJy and was resolved with a size of $4.8'' \times 2.4''$ by these observations. The corresponding physical size at 140 pc of this emission is $\sim 670 \text{ AU} \times 330 \text{ AU}$, which is likely to be representative of a large disk. This source has been detected from B band to a wavelength of 3.3 mm from this survey. It is thought to be associated with the HH312 outflow (Anathpindika & Whitworth 2008). The current literature values of β is -0.5, while dust mass is $0.004 M_{\odot}$ (Andrews & Williams 2007a).

6.5.10 WAOPH6

WAOPH6 is a single YSO of spectral type K6 (Gras-Velázquez & Ray 2005). These observations detect the source with a peak flux of 14.7 mJy but it remains unresolved. It has been detected from B band to the 3.3 mm detection in this survey. Andrews & Williams (2007a) calculate a β value of 0.07 and a dust mass of $0.08 M_{\odot}$ for this source.

6.5.11 YLW58

YLW58 is a single YSO with a spectral type of M4 (Willing et al. 2005). It is detected with a peak flux of 11.8 mJy but is unresolved by OVRO. This source has been previously detected from B band to a wavelength of 1.3 mm. The literature value of β is -0.41, while the dust mass is $0.03 M_{\odot}$ (Andrews & Williams 2007a).

6.6 Class III

None of the Class III objects observed in this survey were detected. All the Class III objects have not been detected at Submm/mm wavelengths. GY10, GY306 and ISO-Oph 26 are all low mass stars with M spectral types. The 3σ upper limits placed on the fluxes of the Class III objects are shown in Table 6.6.

Source Name	3mm Peak Flux [mJy]	3mm Total Flux [mJy]	Map Noise [mJy]	Calibration Uncertainty [mJy]	Source Size ["]
GY10	<3.2	-	1.1	0.3	-
GY12	<2.7	-	1.0	0.3	-
GY29	<4.8	-	1.9	0.5	-
GY306	<1.8	-	1.2	0.2	-
ISO-Oph 26	<2.2	-	1.1	0.2	-

Table 6.6: Table containing the 3σ flux upper limits for the Class III objects.

6.7 Unknown Class

The unknown class objects were not part of the original survey but were present within the confines of maps of other sources. None of these objects were detected. Very little data exist for these sources with the BKLT and GY sources only having been detected in the near-IR, while LFAM and SFAM sources only been detecting at centimetre wavelengths. Upper limits are placed on their possible disk fluxes and are shown in Table 6.7.

Source Name	3mm Peak Flux [mJy]	3mm Total Flux [mJy]	Map Noise [mJy]	Calibration Uncertainty [mJy]	Source Size ["]
BKLT J162736	<1.8	-	1.2	0.2	-
BKLT J162815	<2.5	-	0.8	0.2	-
BKLT J162818	<2.5	-	0.8	0.2	-
GY124	<2.6	-	1.2	0.2	-
GY294	<3.2	-	1.2	0.3	-
GY313	<3.5	-	1.2	0.3	-
LFAM4	<11.4	-	1.9	1.1	-
LFAM16	<3.3	-	1.2	0.3	-
LFAM29	<3.1	-	1.3	0.3	-
LFAM34	<6.6	-	2.0	0.6	-
SFAM127	<3.2	-	1.4	0.3	-

Table 6.7: Table containing the 3σ flux upper limits for the unknown class objects.

Chapter 7

Data Analysis

7.1 Calculating Dust Opacity

The slope of the submm/mm SED between $350\ \mu\text{m}$ and $7\ \text{mm}$ can be used to estimate the dust opacity power law index (β), defined in the relation,

$$\kappa(\nu) = \kappa_0 \left(\frac{\nu}{\nu_0} \right)^\beta, \quad (7.1)$$

where κ is the opacity of the dust and ν is the frequency. Assuming optically thin emission in the Rayleigh Jeans limit the flux is a power law in frequency, $F_\nu \propto \nu^\alpha$. Under this assumption α is given by the formula

$$\alpha = \frac{d \log F_\lambda \lambda}{d \log \lambda}. \quad (7.2)$$

We can link α to β using the equation $\alpha = 2 + \beta$, which is calculated using a simple disk model (Beckwith & Sargent 1991). This means we can calculate beta using one or more observation in the submm regime by fitting a best fit line through the points on a $\log \nu$ against $\log F_\nu$ plot. The sources submm/mm SED's can be found in Figures 7.4–7.8. The uncertainties in β are calculated from the uncertainty in the best fit lines. The Class III objects do not have sufficient dust to be detected at mm wavelengths. Therefore, a dust opacity index is not calculated for these sources.

The 3.3 mm fluxes used to calculate β are free of optically thick contamination by emission from the dense inner disk. Previous surveys suggest that below 1 mm as much as 20% of the detected flux is from optically thick emission (Andrews & Williams 2007a). At these shorter wavelengths this has the effect of artificially decreasing the calculated β value. By including the 3.3 mm data the effects of this contamination should be lowered.

Another form of contamination is present in the 3.3 mm data, free-free emission. This emission does not come from the dust in the disk and has the effect of increasing the flux observed, and hence decreasing β . Free-free emission can be removed by using detected fluxes at centimetre wavelengths and extrapolating these fluxes to 3.3 mm (Patience et al. 2008). Only $\sim 50\%$ of the sources in this survey have centimetre detections and of

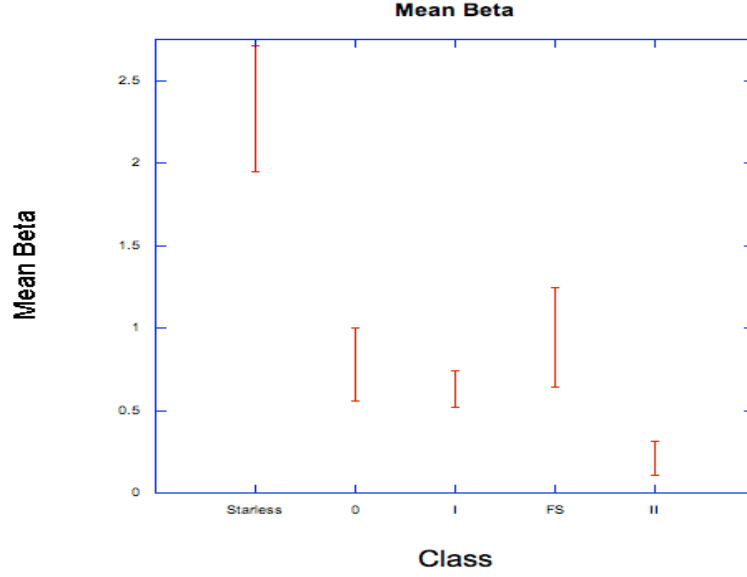


Figure 7.1: Results incorporating the OVRO data to show how dust opacity index, β , changes across the evolutionary stages. There is a clear trend of decreasing β through the evolutionary classes. Although the Flat Spectrum sources appear to have a higher index, this could be simply due to the small number of detected Flat Spectrum sources in this survey.

these detections most are very weak. Even the stronger centimetre sources generally only contribute a small amount to the flux at 3.3 mm, $\sim 10\%$.

The β values calculated range from -0.13, for the Class II source SR4, to 1.5, for the Class I source LFAM26. The mean value for the total sample is ≈ 1.2 , this is skewed toward larger β due to the inclusion of the lower limits on the starless objects. The mean value of β for each class is shown in Fig. 7.1. A clear trend is observed of decreasing β as the evolutionary phase goes from starless to Class II and could indicate that IR evolutionary class and the submm/mm properties of the outer disk are linked. However, Class 0, I and Flat Spectrum cannot be said to differ due to the uncertainties in the means for the samples. The starless cores appear to have a dust opacity index close to the interstellar medium, ~ 2 . The opacity index then decreases through the evolutionary phases to ~ 0.2 for the Class II sources. This trend in opacity index can be accounted for by grain growth of the dust into larger particles resulting in a disk with a mixture of small sub-micron particles and larger millimetre sized particles (Miyake & Nakagawa 1993).

The cumulative distribution of β from this sample was generated using the Kaplan-Meier estimator in order to incorporate the limits. A comparison between using only detections and incorporating the lower limits is shown in Fig. 7.2. These graphs show the probability that the dust will have a β greater than the value of the x-axis. From these distributions we can say the median β value calculated is 0.7.

The Kolmogorov-Smirnov statistical test was employed to determine whether the data from the Class I sources and the Class II source are significantly different. The

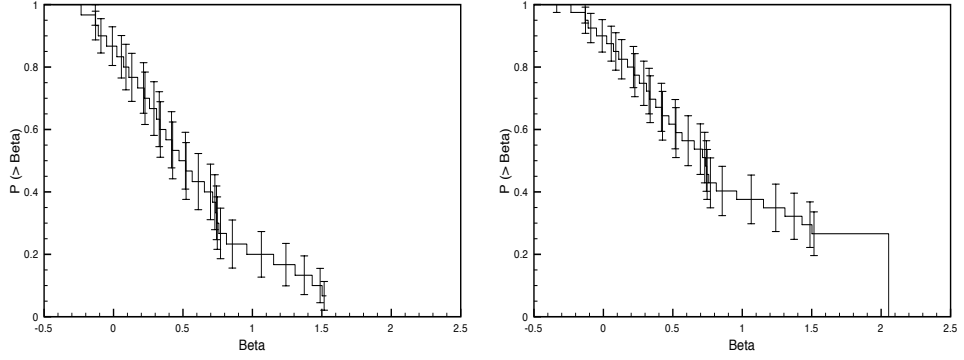


Figure 7.2: Left: The cumulative distribution of β not incorporating the lower limits placed on those sources that were not detected in this survey. This gives a median β value ≈ 0.5 , when only the detections are considered. Right: The cumulative distribution of β with the lower limits included in the calculations. This gives a median β value of ≈ 0.7 . Including the lower limits has the effect of shifting the probability that a disk will have a certain β value to higher values of β , i.e. when only considering the detections only $\sim 20\%$ have a β value > 1 but when you include the lower limits this increases to $\sim 40\%$.

resulting graph is shown in Fig. 7.3. The difference between the two samples can be indicated by a calculation of the D value, which determines the maximum difference in the cumulative fraction between the two datasets. In this case a D value of 0.60 is calculated, which is evidence that the distributions are significantly different. Therefore, we can say the Class II sources are drawn from a distribution with a much lower mean than the Class I sources.

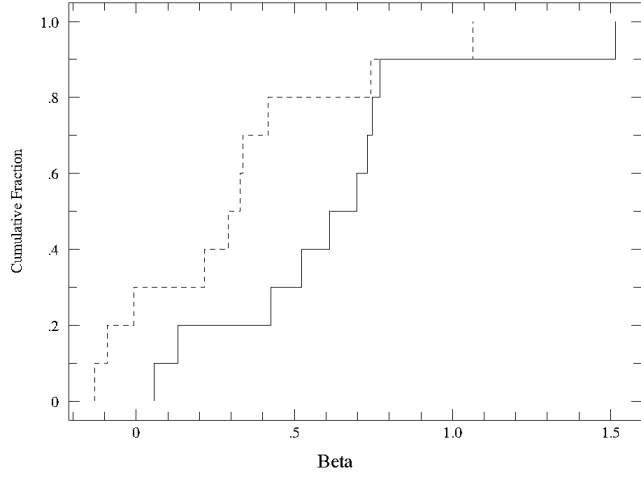


Figure 7.3: The result of the Kolmogorov-Smirnov test to determine whether the Class I sources and the Class II sources could be drawn from the same base distribution. The solid line is the Class I sources, while the dashed line is the Class II sources. The clear gap between the two lines shows that the two classes are indeed statistically significantly different.

7.1.1 Starless

The starless objects β calculations were not performed by calculating the gradient of the submm/mm SED. Their dust opacity values were calculated using only the point from the survey of Motte et al. (1998) and my flux upper limits. This means we can only report lower limits on the dust opacity for all except two of these sources. The mean β value, $\beta = 2.27 \pm 0.21$, was calculated using the Kaplan-Meier estimator to take into account the upper limits. The β values for each starless source are shown in Table 7.1.

Source Name	Dust Opacity Index β	Uncertainty $\Delta\beta$
A-MM1	>0.41	-
A-MM2	0.09	0.53
A-MM3	>0.21	-
A-MM7	1.21	0.83
A-S	>2.25	-
A3-MM1	>2.07	-
B2-MM7	>1.39	-
B2-MM8	>2.22	-
B2-MM10	>1.89	-
B2-MM14	>2.13	-
B2-MM15	>1.58	-
B2-MM16	>2.59	-
B2-MM17	>1.77	-

Table 7.1: Table containing the calculated value and uncertainty of β for the starless objects

7.1.2 Class 0

The Class 0 objects had many previous submm/mm detections. However, they have not had any previous β values calculated in the literature. The mean β value for Class 0 objects calculated in this survey is 0.78 ± 0.22 . This mean value is clearly less than the value for the ISM, perhaps indicating substantial grain growth has already taken place even at this early stage. The β values for each Class 0 source are shown in Table 7.2, while the SEDs used in the calculation are shown in Fig. 7.4.

Source Name	Dust Opacity Index β	Uncertainty $\Delta\beta$
IRAS16293A	0.84	0.24
IRAS16293B	0.28	0.30
LFAM5	1.21	0.49

Table 7.2: Table containing the calculated value and uncertainty of β for the Class 0 objects

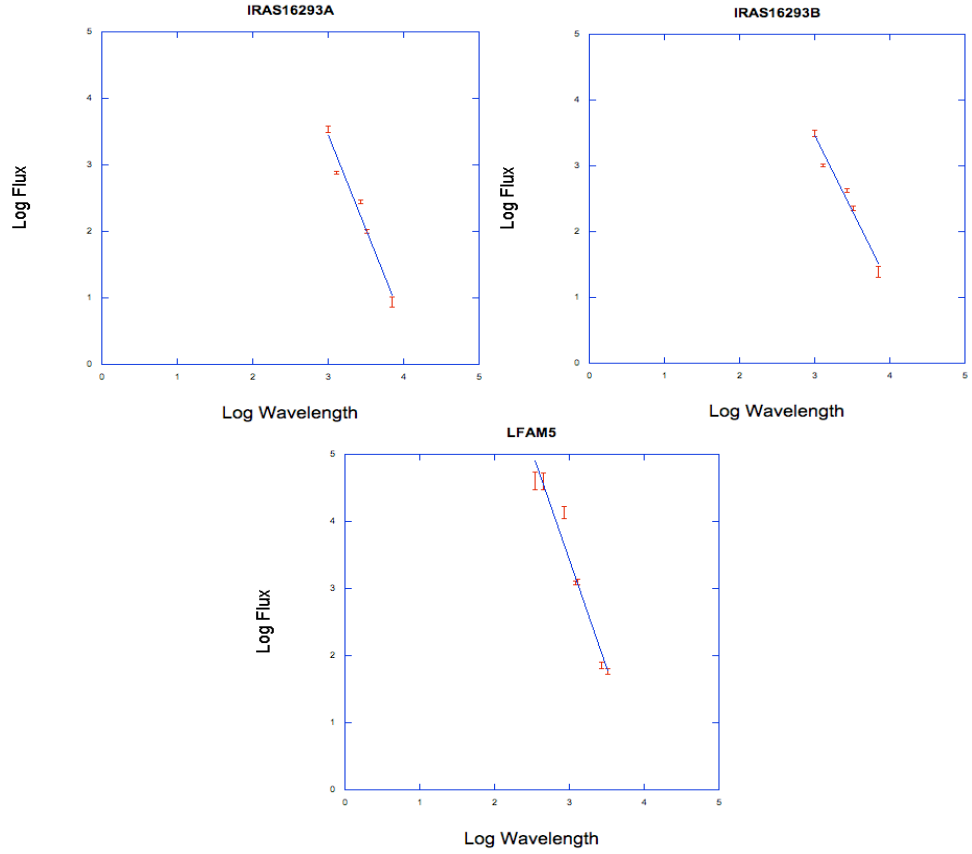


Figure 7.4: Top Left: Submm/mm SED of the source IRAS16293A. Top Right: Submm/mm SED of the source IRAS16293B. Bottom: Submm/mm SED of the source LFAM5.

7.1.3 Class I

All the Class I objects in this survey have had β calculated by Andrews & Williams (2007a), see Section 6.3 for the values. However, they did not attempt to account for the optically thick contamination. These values, calculated using the 3.3 mm point, are less sensitive to optically thick contamination. The mean value of β for the Class I objects is 0.62 ± 0.11 . This value is clearly less than the starless mean, also indicating possible grain growth. The β values for each Class I source are shown in Table 7.3, while the SEDs used in the calculation are shown in Figs. 7.5 and 7.6.

Source Name	Dust Opacity Index β	Uncertainty $\Delta\beta$
CRBR12	0.52	0.10
EL21	0.69	0.06
GY91	0.81	0.10
IRS43	0.77	0.12
L1689S	0.77	0.21
L1709B	0.42	0.14
LFAM26	1.51	0.06
LFAM30	0.06	0.15
YLW2	0.13	0.24
YLW46A	0.61	0.06

Table 7.3: Table containing the calculated value and uncertainty of β for the Class I objects

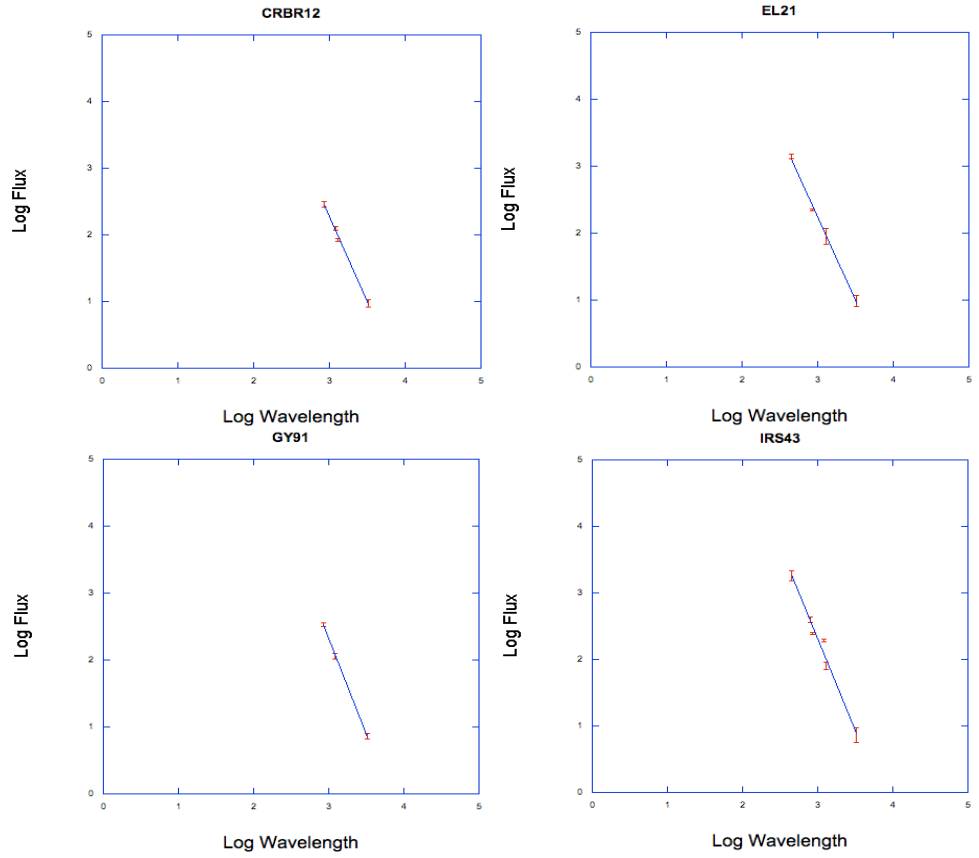


Figure 7.5: Submm/mm SEDs of the class I sources, from top left from top left CRBR12, EL21, GY91 and IRS43.

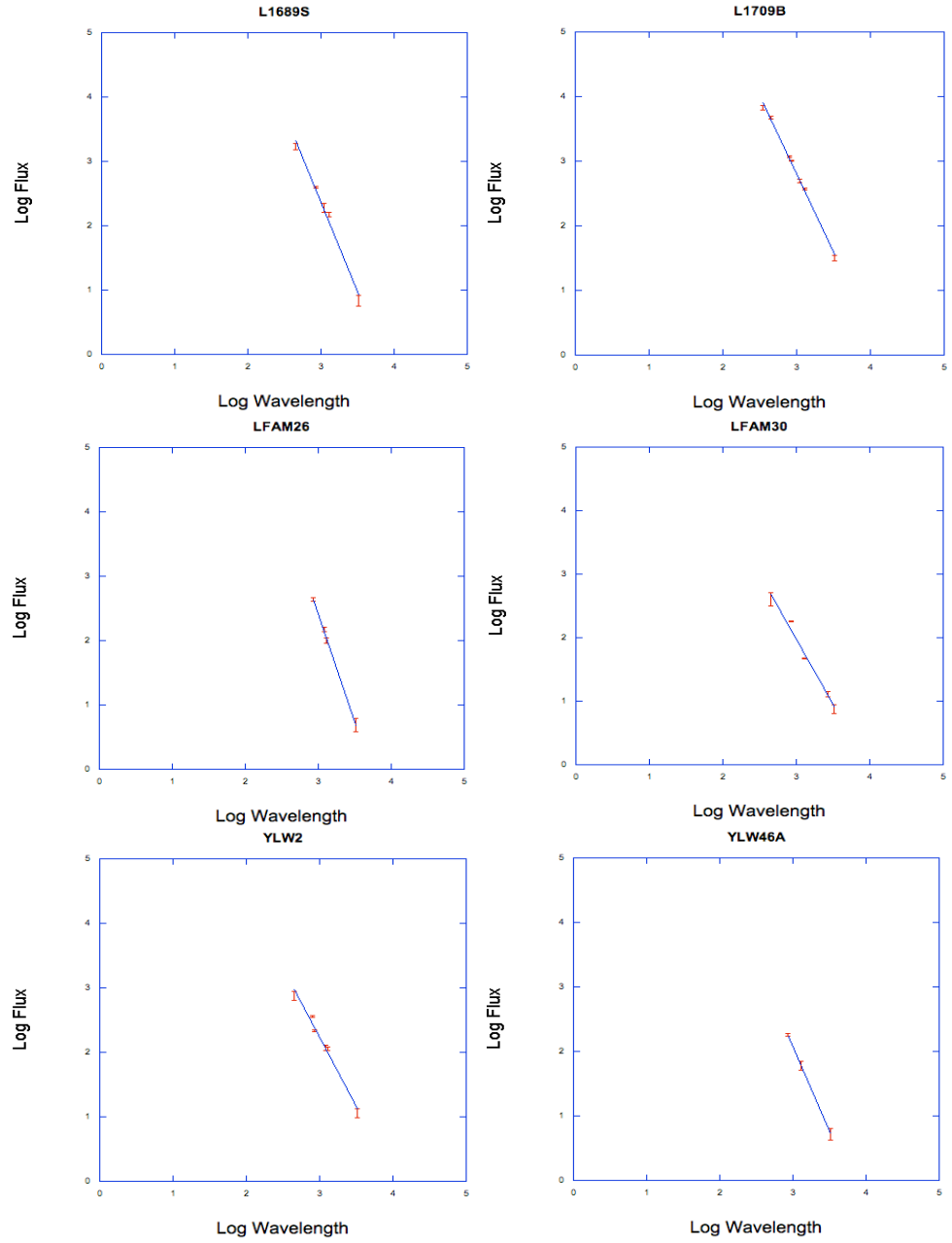


Figure 7.6: Submm/mm SEDs of the Class I sources, from top left L1689S, L1709b, LFAM26, LFAM30, YLW2, and YLW46.

7.1.4 Flat Spectrum

Both the Flat Spectrum sources that have a calculated β value in this survey, are very close to being in IR Class I. Therefore, it is perhaps not surprising that these objects show large values of β . The mean value of β for the Flat Spectrum class, 0.94 ± 0.30 , is higher than that of the Class 0 and Class I. However, due to the significant uncertainties they are not shown to be statistically different. This mean value is still significantly lower than that of the ISM. The β values for each Flat Spectrum source are shown in Table 7.4, while the SED used in the calculation for LFAM 1 is shown in Fig 7.7.

Source Name	Dust Opacity Index β	Uncertainty $\Delta\beta$
L1719B	1.37	0.12
LFAM1	0.52	0.32
RNO91	>0.63	-

Table 7.4: Table containing the calculated value and uncertainty of β for the Class FS objects

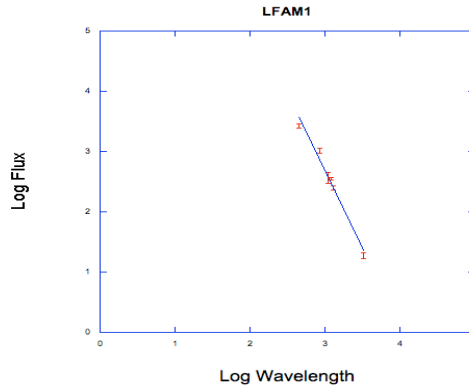


Figure 7.7: Submm/mm SED of the Flat Spectrum source LFAM1. L1719B only had one previous submm/mm measurement and therefore, a graph was not used to calculate β . RNO91 only had an upper limit placed on the 3.3 mm flux, therefore, only a lower limit for β can be established.

7.1.5 Class II

All the Class II objects have a previously calculated value of β from Andrews & Williams (2007a), see Section 6.5 for values. The mean value for the Class II objects is 0.21 ± 0.10 , which is clearly lower than that of the ISM. It is most likely that this reduced dust opacity is due to dust grains growing in size in the disks of these systems. There were no submm/mm literature data for the Flying Saucer, therefore a value of β cannot be calculated. The β values for each Class II source are shown in Table 7.5, while the SEDs used in the calculation are shown in Figs. 7.8 and 7.9.

Source Name	Dust Opacity Index β	Uncertainty $\Delta\beta$
AS205	0.21	0.08
DOAR25	0.20	0.16
DOAR44	0.55	0.46
EL24	0.24	0.12
EL27	0.31	0.10
GSS26	-0.17	0.21
SR21	0.96	0.28
SR4	-0.13	0.55
WAOPH6	0.13	0.17
YLW58	-0.17	0.09

Table 7.5: Table containing the calculated value and uncertainty of β for the Class II objects

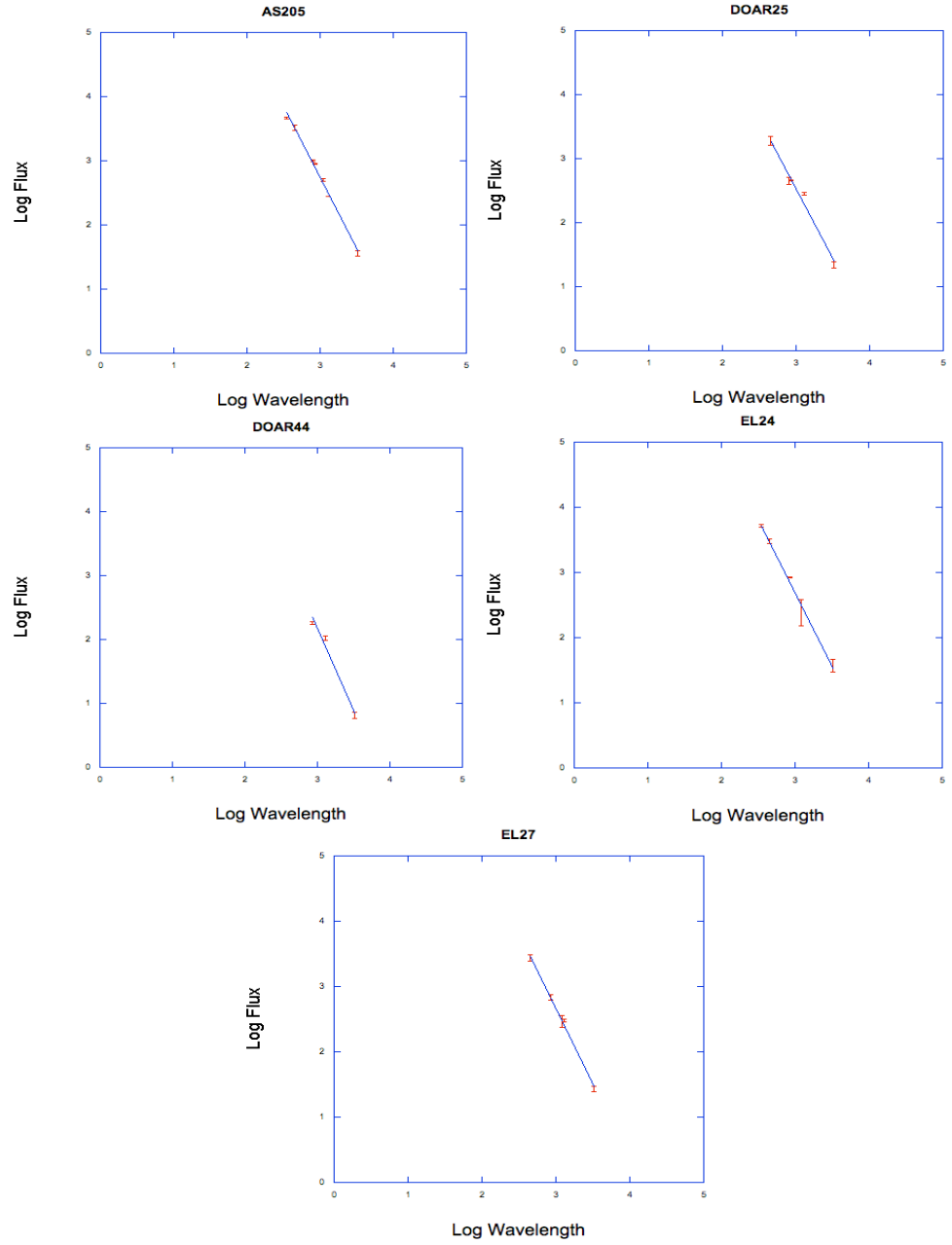


Figure 7.8: Submm/mm SEDs of the class II sources, from top left AS205, DoAr25, DoAr44, EL24 and EL27.

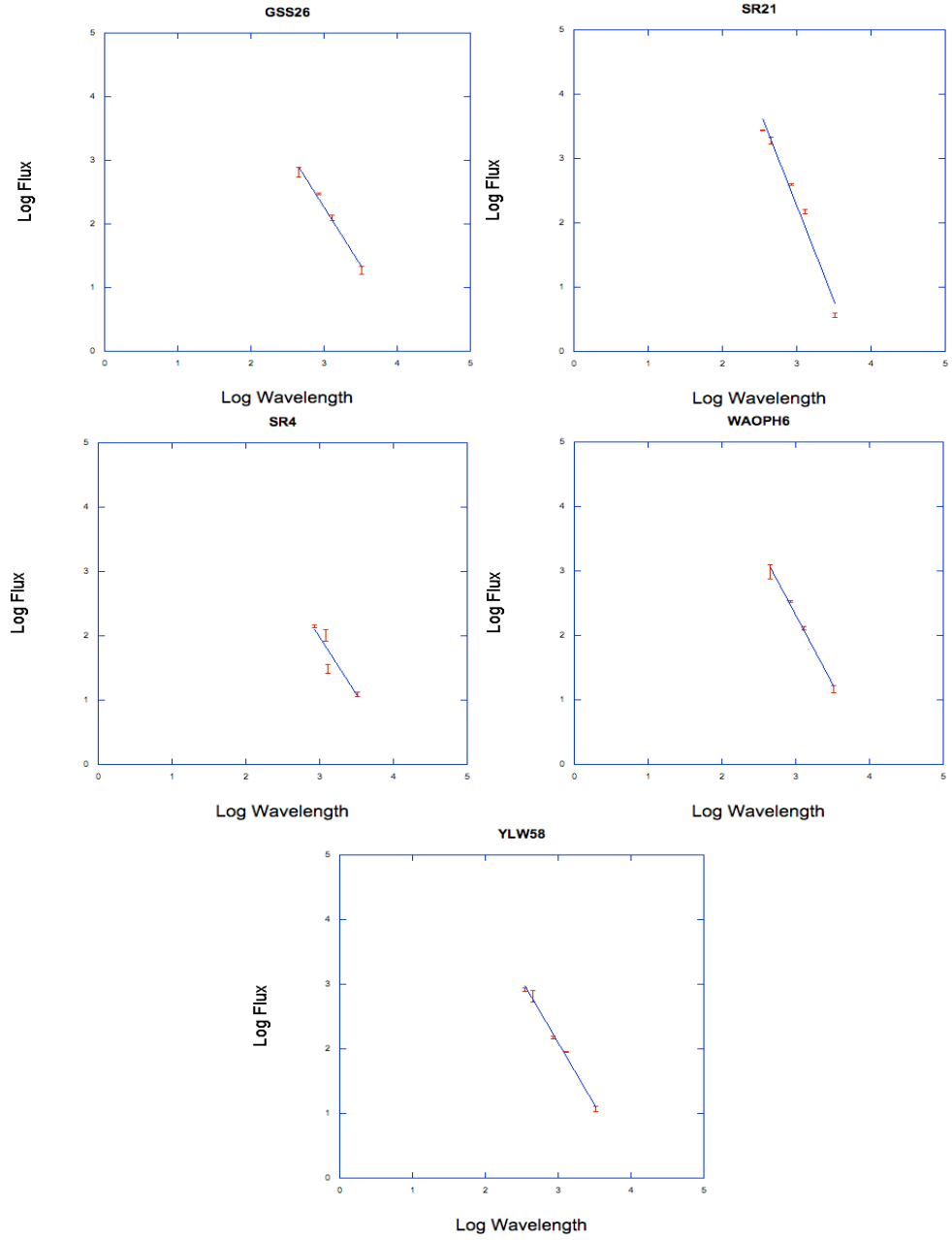


Figure 7.9: Submm/mm SEDs of the class II sources, from top left GSS26, SR21, SR4, WAOph6 and YLW58.

7.2 Calculating Dust Masses

Dust Masses were calculated using both a standard value of β ($\beta = 1$), in order to compare these results with those of Andrews & Williams (2007a), and the calculated β for each source from the previous section. Assuming optically thin emission and cold dust, in the Rayleigh-Jeans limit, it is possible to estimate the total dust mass from the measured submm flux. Total dust masses in units of solar mass were then calculated using the relation:

$$M_d[M_\odot] = \frac{F_\nu D^2}{2\kappa_\nu k T_c M_\odot} \left(\frac{c}{\nu}\right)^2 \quad (7.3)$$

This calculation also requires several other assumptions to be made. We adopt a value of 20K for T_c and a distance, D , of 150 pc to allow a better comparison between these results those of Andrews & Williams (2007a). If a distance of 140 pc is used then all the masses would be $\sim 15\%$ lower. The opacity, κ_ν , is prescribed by the relation, $\kappa_\nu = 0.1(\nu/10^{12}\text{Hz})^\beta \text{ cm}^2\text{g}^{-1}$, where ν is the frequency of the observation and β is the dust opacity index (Beckwith et al. 1990). This relation assumes a gas to dust ratio of 100:1. The standard value of β used by previous surveys was 1 (Beckwith et al. 1990; Andrews & Williams 2007a). The uncertainties in the masses calculated with $\beta = 1$ arise due to the uncertainty in flux measurements. The uncertainties in the masses calculated using the measured β values are given by the equation

$$\delta M_d = M_d \left[\left(\frac{\delta F_\nu}{F_\nu} \right)^2 + \left[-\delta\beta \log \left(\frac{\nu[\text{GHz}]}{10^3} \right) \right]^2 \right]^{1/2}, \quad (7.4)$$

where $\delta\beta$ is the measured error from the straight fit line for β (Patience et al. 2008).

The dust masses calculated using the standard β follow the same trend with evolutionary class as the measured fluxes, as would be expected since the mass is only proportional to the flux in this case. When using the calculated β values the same trend occurs. However, now there is a more obvious drop in mass in the Class II objects. The Flat Spectrum objects also stand out, due to the higher value of β for these sources. Figure 7.10 shows how the dust mass roughly follows the evolutionary phase even when using the calculated value β to determine the mass. The mean dust mass using the standard β for the whole sample is $0.033 M_\odot$. When using the calculated β value to calculate the mass the mean sample mass, $0.018 M_\odot$, is lowered due to the low values of β for each source.

The cumulative distribution of dust masses was calculated using the Kaplan-Meier limit estimator, in order to incorporate the non-detections. Figure 7.11 shows a comparison between the data, when the non-detections are included and when they are not. The median dust mass for this sample is $0.01 M_\odot$. Almost 50% of the sources in this survey have a dust mass greater than the Minimum Mass Solar Nebulae, $0.01 M_\odot$ (Weidenschilling 1977). Indicating these systems should have more than enough dust and gas present for planet formation to take place. However, when calculating the mass using the calculated β only just over 25% of the sources have a disk mass greater than the MMSN. This

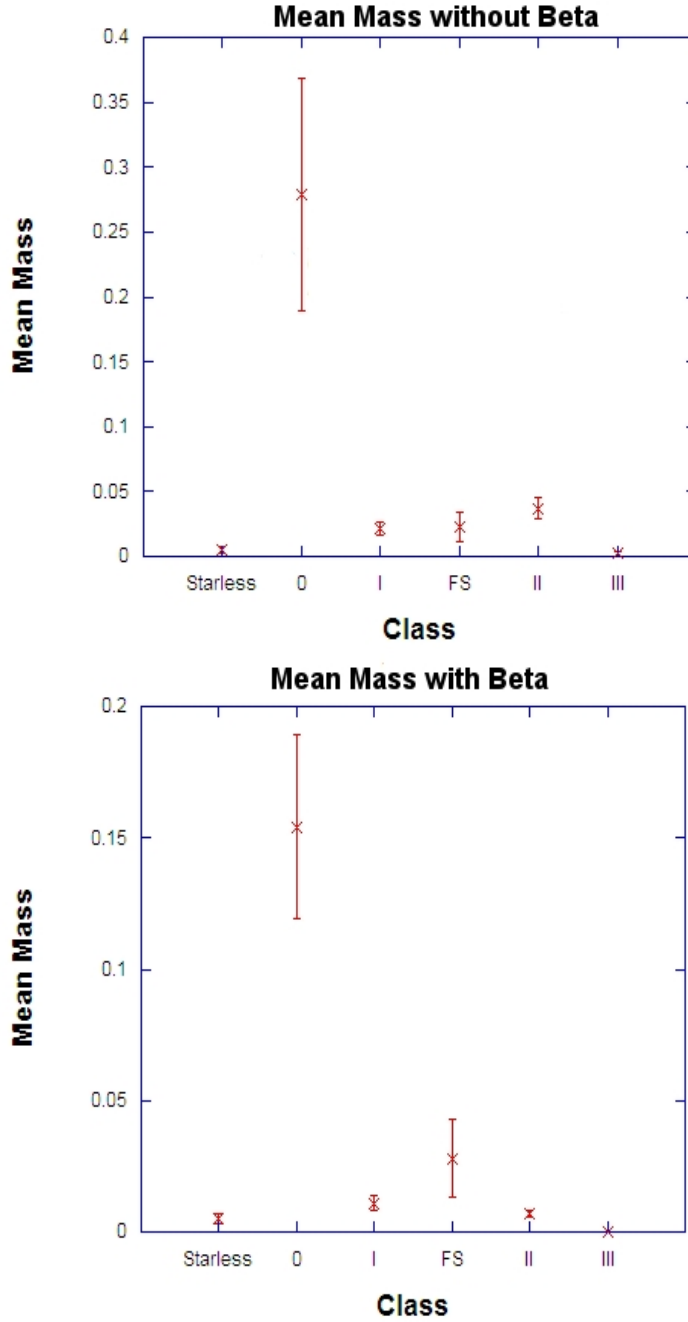


Figure 7.10: Left: Results incorporating the OVRO data to show how dust mass changes across the evolutionary stages, when β is assumed to be 1. After the initial jump from Class 0 to Class I the disk masses appear to be relatively constant over the remaining evolutionary phases. Right: Results incorporating the OVRO data to show how dust mass changes across the evolutionary stages, when M_d is calculated using the β value from this survey. The data follow the same evolutionary path but the Class II objects now have much lower masses due to their small β values.

is calculated under the assumption that the sources that have no β calculation have a $\beta = 1$, which is not only unlikely for the starless sources but ruled out by the lower limits

calculated in Section 7.1.

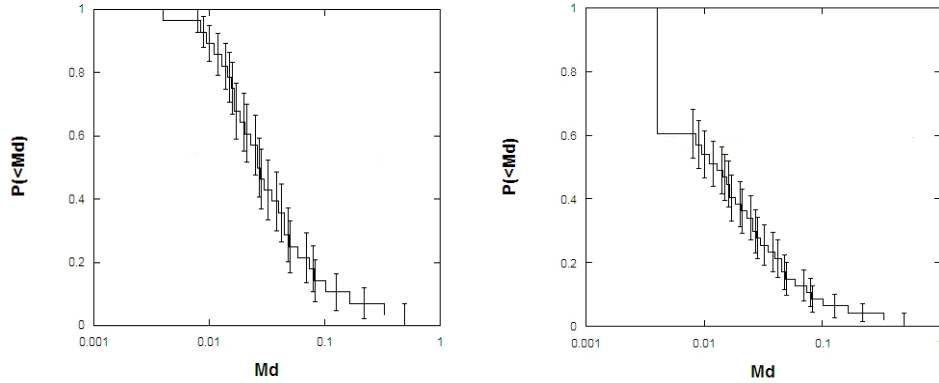


Figure 7.11: Left: The cumulative distribution of dust mass not incorporating the upper limits placed on those sources that were not detected in this survey. The median value of dust mass when only considering the detections is $\approx 0.05 M_{\odot}$. Right: The cumulative distribution of dust mass with the upper limits included in the calculations. The median value of dust mass when including the upper limits is $0.01 M_{\odot}$. Including the non-detections has the effect of lowering the probability that a source has a high mass, i.e. while there is a $\sim 90\%$ probability that the source has a dust mass greater than the MMSN when only including the detection, there is only a $\sim 50\%$ probability when including the upper limits.

The Kolmogorov-Smirnov statistical test was employed to determine whether the calculated masses of the Class I sources differ significantly from those of the Class II sources. The resulting graph is shown in Fig. 7.12. By calculating the D value for these two distributions it is possible to determine whether they are statistically different. In this case a D value of 0.53 indicating that the two samples are drawn from statistically different populations. The mean mass of the Class II sources appears to be higher than the Class I sources. This could be due to flux being resolved out for the Class I sources, while no material is missed in Class II sources.

7.2.1 Starless

Since only lower limits are placed on β for all the starless sources, with the exception of A-MM2 and A-MM7, calculating the mass of the dust using the measured β value is not possible. For the the sources lacking a calculated β , the mass was only calculated in the standard $\beta = 1$ case. However, since the lower limits placed on β are almost all greater than 1, it is possible to say that it is likely there is a much larger mass of dust present than the value calculated here. The mean value of the dust mass from the standard calculation was $0.005 M_{\odot}$.

The starless objects are known to have high β values, from the previous section. However, when calculating the dust mass using each sources β value the mean dust mass of the sample stays the same $0.005 M_{\odot}$. Although the upper mass limits used in this calculation are calculated using the $\beta = 1$ values. Both the standard dust mass calculations

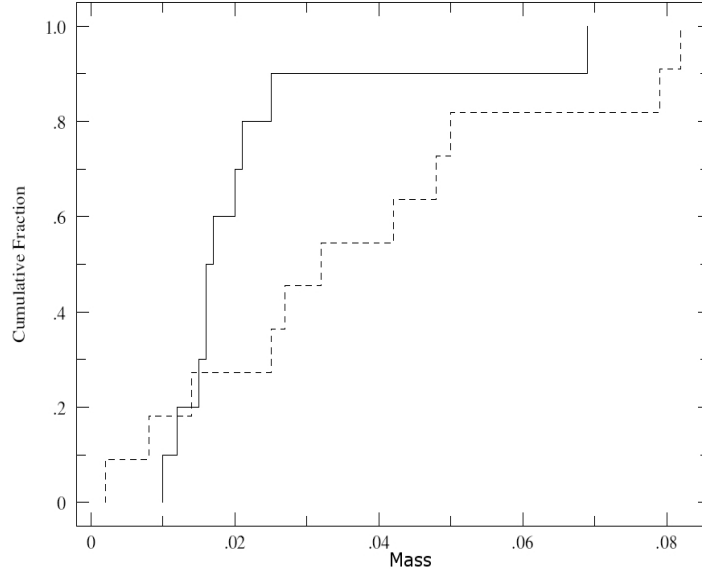


Figure 7.12: The result of the Kolmogorov-Smirnov test to determine whether the Class I sources and the Class II sources could be drawn from the same base distribution. The solid line is the Class I sources, while the dashed line is the Class II sources. The clear gap between the two lines shows that the two classes are indeed statistically significantly different.

and the individual dust mass calculations for the starless objects are shown in Table 7.6.

Source Name	$M_d [M_\odot]$ $\beta = 1$	ΔM $\beta = 1$	$M_d [M_\odot]$ calculated β	ΔM calculated β
A-MM1	<0.011	-	-	-
A-MM2	0.028	0.007	0.003	0.024
A-MM3	<0.015	-	-	-
A-MM7	0.009	0.003	0.030	0.031
A-S	<0.004	-	-	-
A3-MM1	<0.005	-	-	-
B2-MM7	<0.009	-	-	-
B2-MM8	<0.009	-	-	-
B2-MM10	<0.009	-	-	-
B2-MM14	<0.006	-	-	-
B2-MM15	<0.007	-	-	-
B2-MM16	<0.003	-	-	-
B2-MM17	<0.006	-	-	-

Table 7.6: Table containing the dust masses from the standard $\beta = 1$ calculations and the dust masses calculate using each sources β value for the starless objects.

7.2.2 Class 0

The Class 0 sources have high fluxes and, therefore, high dust masses when calculated using the standard β value. The mean standard dust mass value for these sources is

0.279 M_{\odot} . By comparison the mean value of the dust mass using the calculated β is 0.154 M_{\odot} , nearly 50% that of the standard calculation. In both cases the Class 0 objects are the most massive in this survey. Both the standard dust mass calculations and the individual dust mass calculations for the Class 0 objects are shown in Table 7.7.

Source Name	$M_d [M_{\odot}]$ $\beta = 1$	ΔM $\beta = 1$	$M_d [M_{\odot}]$ calculated β	ΔM calculated β
IRAS16293A	0.218	0.023	0.156	0.042
IRAS16293B	0.493	0.050	0.078	0.025
LFAM5	0.126	0.013	0.227	0.118

Table 7.7: Table containing the dust masses from the standard $\beta = 1$ calculations and the dust masses calculate using each sources β value for the Class 0 objects.

7.2.3 Class I

All the Class I sources could have dust mass calculated using both techniques. The mean dust mass using the standard calculation was 0.022, while for the individual β calculation it was 0.011. Both the standard dust mass calculations and the individual dust mass calculations for the Class I objects are shown in Table 7.8.

Source Name	$M_d [M_{\odot}]$ $\beta = 1$	ΔM $\beta = 1$	$M_d [M_{\odot}]$ calculated β	ΔM calculated β
CRBR12	0.020	0.003	0.007	0.001
EL21	0.021	0.005	0.010	0.002
GY91	0.016	0.002	0.008	0.001
IRS43	0.016	0.005	0.009	0.003
L1689S	0.015	0.003	0.009	0.003
L1709B	0.069	0.008	0.017	0.003
LFAM26	0.010	0.003	0.037	0.010
LFAM30	0.017	0.003	0.002	0.0004
YLW2	0.025	0.005	0.003	0.001
YLW46A	0.012	0.003	0.004	0.001

Table 7.8: Table containing the dust masses from the standard $\beta = 1$ calculations and the dust masses calculate using each sources β value for the Class I objects.

7.2.4 Class FS

The Flat Spectrum sources are very diverse in their fluxes, hence also in their calculated masses. The two detected sources have fairly high masses but with three non-detections the mean, 0.023 M_{\odot} , is brought down to roughly the level of the Class I and Class II sources. The mean of the individually calculated sample is 0.028 M_{\odot} . This figure is well above that of the Class I and Class II objects. This appears to be due to the high value of β calculated for L1719B, which then increases the calculated mass substantially. Both

the standard dust mass calculations and the individual dust mass calculations for the Flat Spectrum objects are shown in Table 7.9.

Source Name	$M_d [M_\odot]$ $\beta = 1$	ΔM $\beta = 1$	$M_d [M_\odot]$ calculated β	ΔM calculated β
GY11	<0.011	-	-	-
L1719B	0.038	0.004	0.093	0.015
LFAM1	0.042	0.004	0.013	0.004
LFAM15	<0.011	-	-	-
RNO91	<0.011	-	-	-

Table 7.9: Table containing the dust masses from the standard $\beta = 1$ calculations and the dust masses calculate using each sources β value for the Flat Spectrum objects.

7.2.5 Class II

The Class II sources mean mass calculated by the standard method differs the most of all the classes from the mean mass calculated using the individual β method. This is due to the fact that the Class II sources have very low values of β . The mean mass changes from $0.037 M_\odot$ using the standard calculation to $0.007 M_\odot$ using the individual calculation. Since no calculation of β was possible for the Flying Saucer, only the mass calculation with $\beta = 1$ is included. Both the standard dust mass calculations and the individual dust mass calculations for the Class II objects are shown in Table 7.10.

Source Name	$M_d [M_\odot]$ $\beta = 1$	ΔM $\beta = 1$	$M_d [M_\odot]$ calculated β	ΔM calculated β
AS205	0.079	0.008	0.011	0.002
DOAR25	0.048	0.005	0.007	0.001
DOAR44	0.014	0.003	0.005	0.002
EL24	0.082	0.009	0.013	0.002
EL27	0.050	0.006	0.012	0.002
Flying Saucer	0.002	0.001	-	-
GSS26	0.042	0.006	0.002	0.0006
SR21	0.008	0.002	0.007	0.003
SR4	0.027	0.004	0.002	0.001
WAOPH6	0.032	0.004	0.004	0.0009
YLW58	0.025	0.003	0.002	0.0003

Table 7.10: Table containing the dust masses from the standard $\beta = 1$ calculations and the dust masses calculate using each sources β value for the Class II objects.

7.2.6 Class III

The Class III sources have no previous submm/mm detections and so the upper limits to the dust masses can only be calculated using the standard method. The mean mass of the Class III sources from the Kaplan-Meier limit estimator is $0.002 M_\odot$. This is skewed

towards a higher value because the highest upper limit value is assumed to be a detection by this technique. The standard dust mass calculations for the Class III objects are shown in Table 7.11.

Source Name	$M_d [M_\odot]$ $\beta = 1$	ΔM $\beta = 1$
GY10	<0.007	-
GY12	<0.006	-
GY29	<0.011	-
GY306	<0.004	-
ISO-Oph 26	<0.005	-

Table 7.11: Table containing the dust masses from the standard $\beta = 1$ calculations for the Class III objects. Since none of the sources have been previously observed at submm/mm wavelengths, β cannot be calculated individually. Therefore, there are no individual calculations of mass for these sources.

7.3 Comparison with Other Studies

The main study that this work can be compared to is the work of Andrews & Williams (2007a). They also found that the dust opacity appears to scale with the evolutionary stage of the object. However, their survey did not include starless clumps or Class 0 and therefore this work extends this theory into earliest evolutionary phases. By including these objects a mean value of β is reported as ≈ 1.2 , much higher than their mean value of ≈ 0 . However, in order to attain a more direct comparison to their work the Starless and Class 0 sources must be removed from the mean calculation. When this is done, a mean value of ≈ 0.5 is calculated. This indicates the derivations of β in this work are systematically higher than those of Andrews & Williams (2007a). This could be as a result of the optically thick contamination at the shorter wavelengths affecting their calculation more than those of this survey.

The study of Andrews & Williams (2007a) calculated a mean value for the dust mass of $\sim 0.005 M_\odot$, which is much lower than the value calculated from this survey. Even when restricted to the same evolutionary range that Andrews & Williams considered our mean mass is over two times higher, $\sim 0.024 M_\odot$. This is possibly a bias effect. Andrews & Williams included many sources that were not detected at submm/mm wavelengths, while this sample was drawn from objects that already have some form of submm/mm detection. By doing this we have biased our results towards higher fluxes, and hence higher masses.

Chapter 8

SED Fitting

Using the new 3.3 mm data and literature data from $0.35\,\mu\text{m}$ to 1.3 mm, SEDs were fitted with the online SED fitting tool of Robitaille et al. (2007). This process consists of comparing a source’s SED to each member of a grid of over 200,000 models, and using the χ^2 statistic to determine which model gives a best fit to the data. These models assume symmetrical systems with no external interference. The model with the lowest χ^2 value can then provide a fit to 23 parameters of the source, including disk mass and envelope mass, allowing constraints to be placed on the values of these parameters for the source. Best fit models that have a reduced χ^2 of greater than 100 were rejected as they do not provide reliable parameter estimates. The fitting routine takes a distance range to the source and a range of interstellar extinctions as inputs as well as the SED. For these sources a range of distances between 140 pc and 160 pc was used while the interstellar extinction, A_V , was source dependant. The interstellar extinction range input into the fitting routine was generally a previously calculated $A_V \pm 5$. The models then incorporate this range into the fitting and return a best fit extinction, which is then compared with the extinction calculated in the COMPLETE survey (Ridge et al. 2006). In most cases the best fit A_V is very close to that measured by COMPLETE.

We take the highest quality measurement at each wavelength for the source, as was done in Robitaille et al. (2007). For example, we reject IRAS data if there is MIPS data available for that source. One of the drawbacks of this modeling is that it currently has poor signal to noise at wavelengths greater than 1 mm. This is due to unknown dust properties and external illumination becoming more important at these longer wavelengths (Whitney, private communication). However, as these models are widely used we ran fits including the new OVRO 3.3 mm data and not including the 3.3 mm flux. By removing the 3.3 mm point we clearly lower the χ^2 value of the fit. Despite the problems with including these 3.3 mm data, the best fit models that are returned by not including these data generally have similar parameters to those returned when we include our data-points.

The current lack of multiple system models result in stellar properties of the best fit parameters that are not realistic for the multiple sources. However, these models should still be good at determining the amount of circumstellar material around the binary. The stellar age is also one of the parameters in these fits, but this is not necessarily the true

age of the object; it is only used in the modeling to determine the stellar radius and temperature from pre-main sequence evolutionary tracks. A more detailed list of the known complications associated with these models is presented in Robitaille et al. (2006).

The best fit parameters generated by the fitting are consistent with the evolutionary class of each source. Using the SED fitting technique, the mean disk mass is calculated to be $0.018 M_{\odot}$, while the mean envelope mass is calculated to be $0.53 M_{\odot}$. Only when the disk mass and envelope masses are added can we compare with the previous derivations in Chapter 7.2. When this is done the mean total dust mass is $0.53 M_{\odot}$, which compares to $0.024 M_{\odot}$ from earlier calculations. The massive envelopes of the Class 0 sources result in the total circumstellar material mass being much higher for the fitted models. Also, as even the Class III sources are fitted there are no upper limit disk masses, which would act to lower the mean mass when averaging with the Kaplan-Meier limit estimator. Some of the non-detected sources at 3.3 mm (Class III systems) show some signs of having circumstellar material in these models. All these effects bias the total mass figure to higher values. This increase in mean circumstellar material mass also has implications for planet formation as using the multi-wavelength fitting results in over 80% of the sources having masses greater than the MMSN.

8.1 Class 0

As both the Class 0 sources are binary systems, the stellar component of the best fit SED is again not considered. Since the only available Mid and Far IR data for the source IRAS16293 was from low resolution ISO and IRAS maps, which did not resolve the pair, the SED consists of the flux from both components of the binary combined. The best fit SEDs both including the 3.3 mm data and not including the millimetre data are shown in Fig. 8.1.

Both the Class 0 objects have massive envelopes with comparatively small disks, as is expected at this stage of evolution. The envelopes are large enough, $\sim 10^3$ AU, to be partially resolvable with the OVRO array.

8.1.1 IRAS16293

The reduced χ^2 value for this model when including the new 3.3 mm data is 30.78, while not including the data results in a reduced χ^2 value of 15.9. The A_V for the best fit model of this source is 17, which compares well to the 16.69 measured in the COMPLETE survey (Ridge et al. 2006). The main difference between the two models is the mass of the star. However, this is irrelevant as we know this source is a binary. Therefore we are only interested in the best fit disk and envelope properties. The disk mass differs between the two models by an order of magnitude. However, in both cases the mass in the disk is negligible compared to the mass in the envelope. The size of the envelope, ~ 7000 AU, indicates that this source should be partially resolvable with the $\sim 6''$ resolution of OVRO and the source does appear to be.

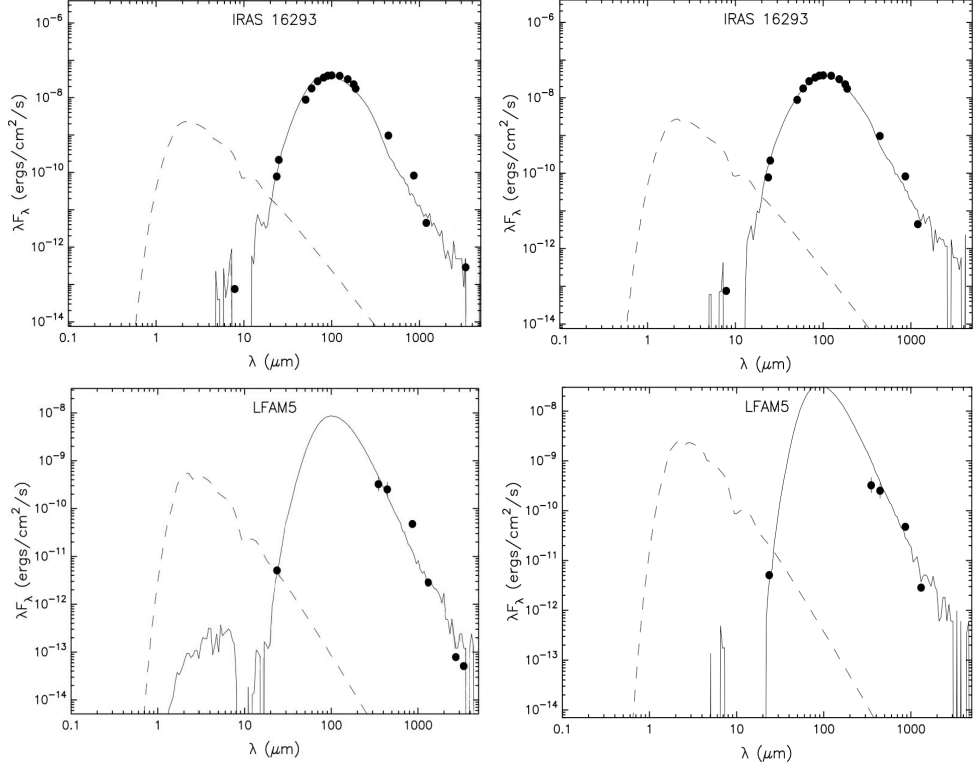


Figure 8.1: Left: The best fit SEDs including the 3.3 mm point for the Class 0 sources. Right: The best fit SEDs not including the 3.3 mm point for the Class 0 sources. Top: IRAS16293, Bottom: LFAM5.

8.1.2 LFAM5

The reduced χ^2 value for this model when including the 3.3 mm data is 37.5, while not including the data results in a χ^2 value of 7.7. However, the model that does not include the 3.3 mm data is unrealistic, due to the size of the envelope this model would require, 32200 AU. If the envelope of this source was this size then it would be resolved at a much larger size than it is in this survey, and a large portion of the envelope would be resolved out by the interferometer. Neither of these things would appear to be the case. Therefore, we can say including the 3.3 mm data greatly increases our confidence in this model, so we adopt it as best fit. This model consists of a large envelope, $1.3 M_{\odot}$, with a small disk, $0.04 M_{\odot}$, both are values typical for a Class 0 source. The envelope size is 1500 AU, which is nearing the resolution of the OVRO array. The best fit model has an $A_V = 20$, which compares to 19.68 measured in the COMPLETE survey.

8.2 Class I

The stellar parameters of the sources best fit models are not shown for CRBR12, EL21, IRS43, LFAM30 and YLW46A due to the multiple nature. The best fit SEDs both including the 3.3 mm data and not including the millimetre data are shown in Figs. 8.2, 8.3, 8.4

& 8.5.

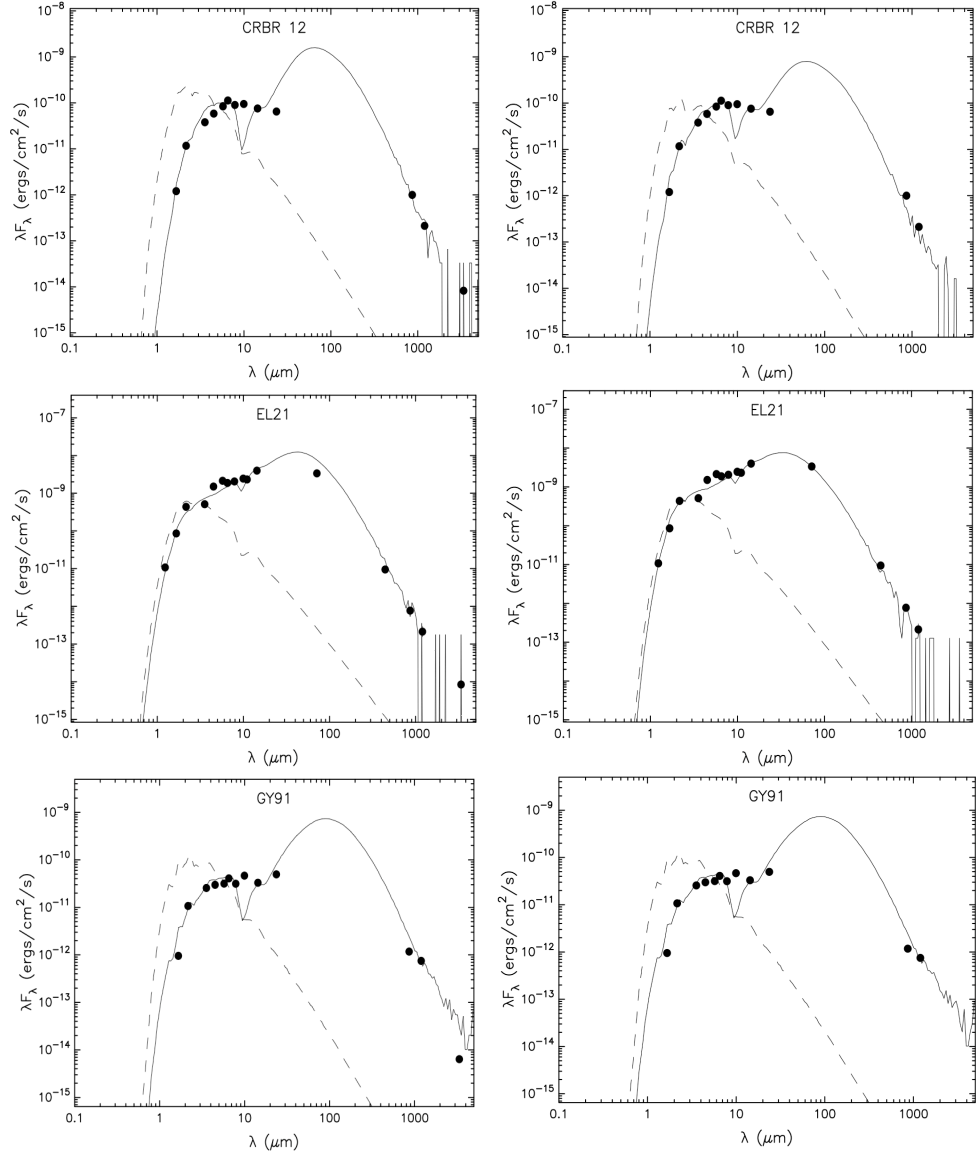


Figure 8.2: Left: The best fit SEDs including the 3.3 mm point for the Class I sources. Right: The best fit SEDs not including the 3.3 mm point for the Class I sources. Top: CRBR12, Middle: EL21, Bottom: GY91.

All the Class I sources show at least some envelope material. However EL21 and IRS43 appear to have very small envelopes given their evolutionary class. None of the sources have larger envelopes than either of the Class 0 sources. The mean envelope mass for the Class I sources is $0.25 M_{\odot}$. The disks around the Class I objects do not contain a great deal of mass at this stage with the mean disk mass, $0.009 M_{\odot}$, much lower than the mean envelope mass.

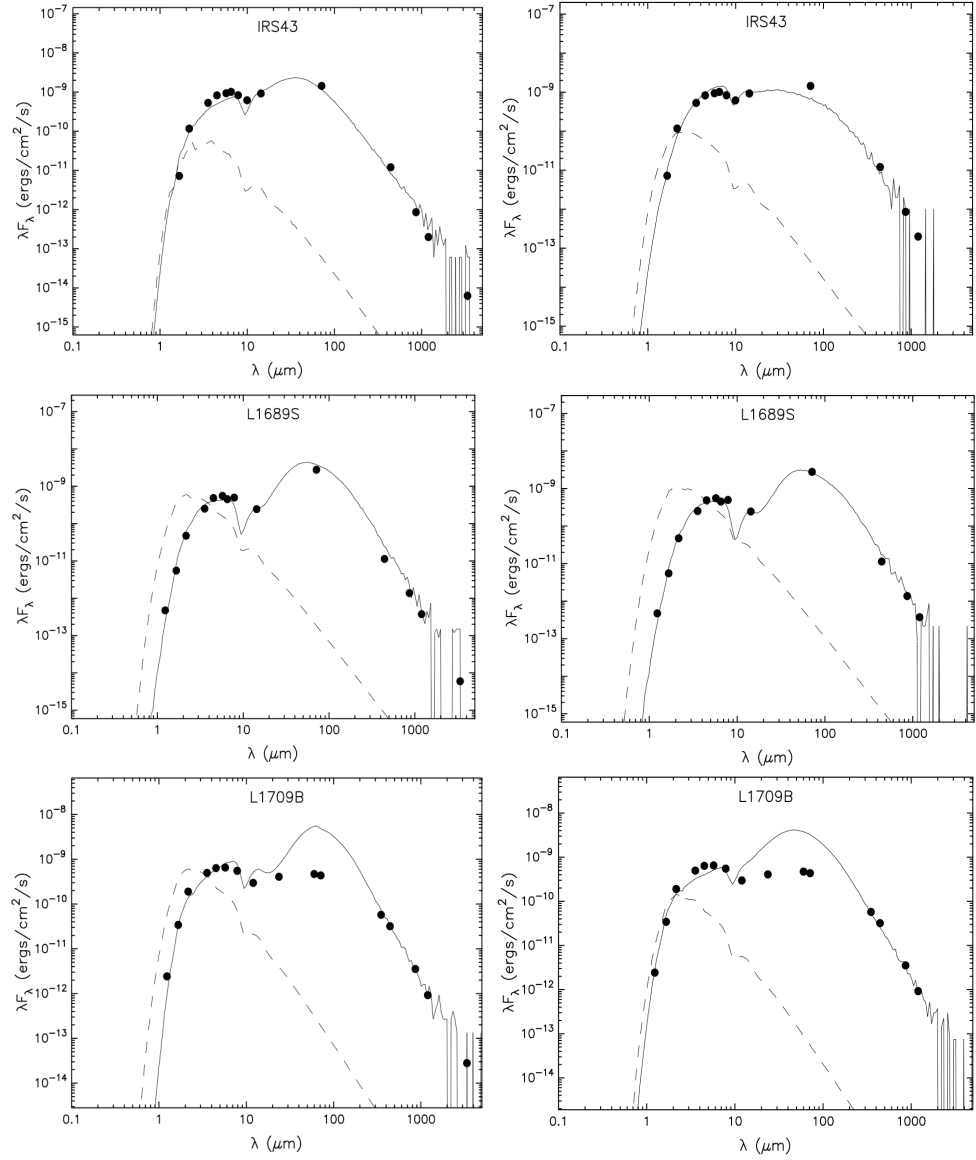


Figure 8.3: Left: The best fit SEDs including the 3.3 mm point for the Class I sources. Right: The best fit SEDs not including the 3.3 mm point for the Class I sources. Top: IRS43, Middle: L1689S, Bottom: L1709B.

8.2.1 CRBR12

The fit to CRBR12 including the 3.3 mm data gave one of the poorer fits, reduced χ^2 of 79, which appears to be due to a large dip in the model spectra at $\sim 10 \mu\text{m}$ and a possible overestimate of envelope emission at $\sim 70 \mu\text{m}$. This dip is seen in the best fit models when including the 3.3 mm data and when it is not included. The lack of a $70 \mu\text{m}$ MIPS data-point leads to the possible over estimate of envelope flux. In both the with and without 3.3 mm cases the best fit model is clearly better than the next best fit model by around 5 times χ^2 per data-point, indicating this is the best this fitting can achieve. In both models the envelope mass, $\sim 0.2 M_\odot$, dominates over a relatively small disk, $\sim 0.0001 M_\odot$.

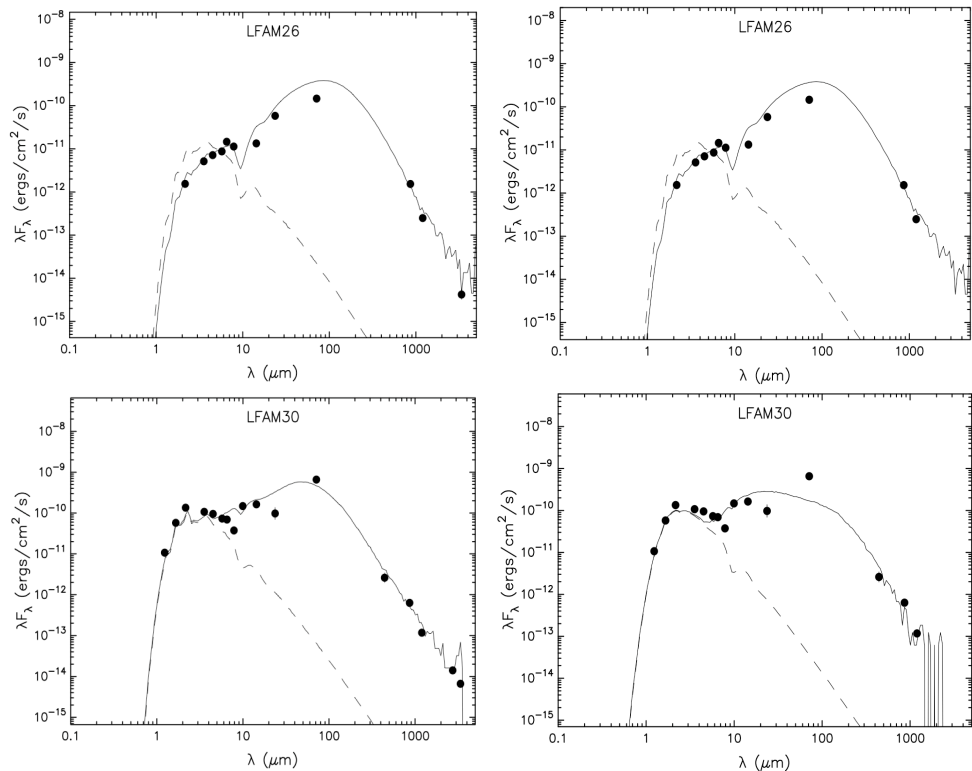


Figure 8.4: Left: The best fit SEDs including the 3.3 mm point for the Class I sources. Right: The best fit SEDs not including the 3.3 mm point for the Class I sources. Top: LFAM26, Bottom: LFAM30.

However, adding the 3.3 mm data-point should allow us to constrain the envelope flux once the models have been improved. The A_V for the best fit model including the 3.3 mm data was 18.26, which is very close to the COMPLETE A_V of 18.72.

8.2.2 EL21

EL21 is one source that seems to benefit greatly by not including the 3.3 mm point in the modeling. The reduced χ^2 goes from 36, still a good fit, to 19. This decrease is clearly due to the 1.3 mm model fitting the 70 μ m MIPS data far better. Therefore, in this case we take the model without the 3.3 mm data to be the best fit model. This model suggests a nearly face on inclination with an A_V of 20.82, slightly higher than the COMPLETE value of 19.9. The model has a typically large envelope compared to disk mass, 0.01 M_\odot to 0.0005 M_\odot .

8.2.3 GY91

Not including the 3.3 mm data made no difference to the best fit model. The best fit model has an A_V of 14.0, which is quite a bit lower than the COMPLETE A_V of 15.5. There is a dip in the model at $\sim 10 \mu$ m similar to that in the best fit of the source CRBR12. This again leads to a poor fit to the data at the 10 μ m point leading to a reduced χ^2 of 44.2.

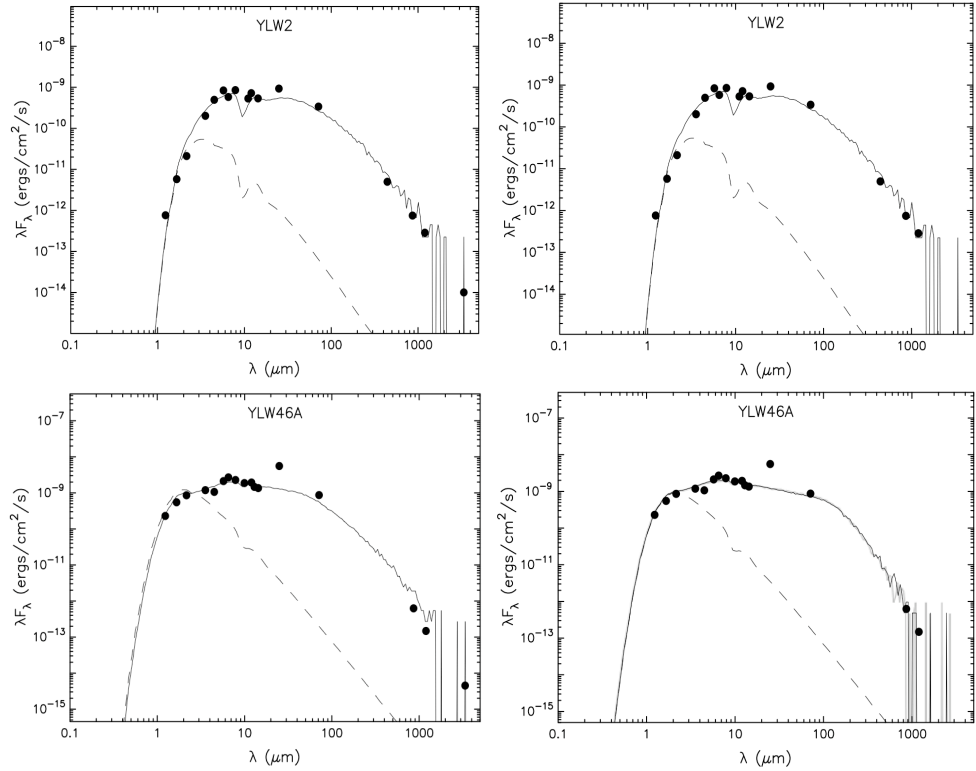


Figure 8.5: Left: The best fit SEDs including the 3.3 mm point for the Class I sources. Right: The best fit SEDs not including the 3.3 mm point for the Class I sources. Top: YLW2, Bottom: YLW46A.

Therefore, even with this outlying point this model is still considered reliable. GY91 is a single star and therefore the best fit parameters for the central star are also considered. The mass of the star in the best fit model is close to the lower limit that was considered by this fitting, $0.13 M_{\odot}$. This mass is comparable to the mass remaining in the envelope, $0.48 M_{\odot}$, while the disk mass is not much lower, $0.01 M_{\odot}$. This hints that this system is perhaps very young and the star is still to accrete a significant amount of mass.

8.2.4 IRS43

This source produced very different results for the best fit model between including or not including the 3.3 mm data. The best fit model when including the 3.3 mm data is similar to a Flat Spectrum source, where the envelope and the disk have comparable mass. However, when this point is not including the best fit model is a large edge-on disk with no envelope. This is a degeneracy noted in Robitaille et al. (2007), where a disk + envelope model can have a very similar SED to a disk only model viewed nearly edge-on. This arrangement would require the central star to be much more massive, $\sim 3 M_{\odot}$, this is unlikely to be the case for this star. Therefore, the model including the 3.3 mm data is the model we adopt. This model looks like a Flat Spectrum source and is the only Class I source that has an envelope with less mass than its disk, $0.004 M_{\odot}$ in the envelope compared to $0.01 M_{\odot}$ in

the disk. This fitting suggests this source should be a Flat Spectrum source not a Class I, which is not inconsistent with what was reported in Chapter 7 as its β value is consistent with either class.

8.2.5 L1689S

The best fit model does not change greatly when the 3.3 mm point is removed. However, there is a marked improvement in the reduced χ^2 when not including the 3.3 mm data; reduced χ^2 of 78.9 when including the 3.3 mm, reduced χ^2 of 29.7 when not. Therefore, the model that does not include the 3.3 mm point is taken to be best. This model is calculated using an A_V of 16.27, which is lower than the 17.8 measured by COMPLETE. The stellar parameters for this source suggest a star of around $1.3 M_\odot$, while the envelope mass is $0.5 M_\odot$, with a disk mass of $0.02 M_\odot$. These parameters indicate a Class I source in the early stages of this evolutionary phase.

8.2.6 L1709B

None of the models in the grid appear to fit these data very well, the best fit model has a reduced χ^2 of 157. Both the with 3.3 mm and the without best fit models seem to overestimate the amount of envelope material, as seen by the models indicating the MIPS flux should be around an order of magnitude higher. Due to these large differences we do not believe any of the models have a good enough fit to give reliable parameters.

8.2.7 LFAM26

LFAM26 produces the best fit of all the Class I source with a reduced χ^2 of only 22. For this source the same model is the best fit to both the with and without 3.3 mm SED. The model indicates an edge on source that suffers from a very large amount of interstellar extinction, $A_V = 30$. The stellar source for this model is low mass $0.12 M_\odot$, which provides very little heating to the inner edge of the disk. The model has a large envelope, $0.25 M_\odot$, with a comparatively small disk, $0.007 M_\odot$, indicative of the Class I phase.

8.2.8 LFAM30

The fitting of this source appears to be good when examining the SED by eye. However, the reduced χ^2 value is very high, 156. There are two outlying points, the $8 \mu\text{m}$ IRAC and $24 \mu\text{m}$ MIPS data, yet they do not appear to be so far to produce the large χ^2 value the fitting returns. Due to these concerns we shall not assign any parameters to this source.

8.2.9 YLW2

YLW2 has a similar problem to that addressed for LFAM30. By eye, the fit looks very good but it returns a very poor reduced χ^2 value of 154. However, unlike LFAM30 there are no really obvious outlying points. The best fit to this source indicates a high level of

interstellar extinction, $A_V = 35$. Indeed this very high interstellar extinction is perhaps the reason for the large χ^2 in the case of this source. As these models were only tested between an A_V range of 0 to 20. Due to the poor value of χ^2 the best fit model for this source is not thought to be reliable enough to return good parameters.

8.2.10 YLW46A

This source has one very obvious outlying point, the $25\mu\text{m}$ IRAS detection, in both the with and without 3.3 mm models. The model appears to fit the other points very well. However, due to this outlying point the models have a high value for the reduced χ^2 , 125.8, above the cut-off for a reliable fit. Removing the 3.3 mm data results in the reduced χ^2 being lowered to 79, which is under the cut-off. Therefore, we will take the parameters from the best fitting model without the 3.3 mm data to be reliable. This model appears to be a Class II, with little or no envelope but a large disk. The disk mass is $0.05 M_\odot$, and it extends to over 400 AU.

8.3 Flat Spectrum

The stellar parameters for the source SR24 are not considered as this source is a triple system. LFAM15 was not fit reliably by any of the models. The best fit SEDs including the 3.3 mm data and not including the new data are shown in Figs. 8.6 & 8.7. The mean envelope mass of these sources is $0.3 M_\odot$, ignoring GY11 as it appears to be classified incorrectly. The mean disk mass for these source is $0.005 M_\odot$. These values are not significantly different from those for the Class I sources.

8.3.1 GY11

The GY11 SED remains unchanged when including the millimetre data, suggesting that this source is classified incorrectly. Indeed this system is best fit, reduced $\chi^2 = 53$, by a model with similar parameters to a Class III system. The model has no envelope and only a very small disk of mass $0.000006 M_\odot$, that produces a very small mid-IR excess. The model also assumes a stellar mass of $0.43 M_\odot$. This source has a previous spectral type of M7, which would indicate the stellar mass should be less than that in the best fit model.

8.3.2 L1719B

The source only has 5 points on its SED and as such it is possible to produce many good fits to the models. As a result of this, L1719B has one of the lowest reduced χ^2 values, 10, of this sample. However, despite the best fit models providing very good fits, their parameters differ greatly between the best few models. The models generally have around $0.04 M_\odot$ of circumstellar material, which is split in different ways between the envelope and disk. There is no previous A_V measurement for this source and so the full range of

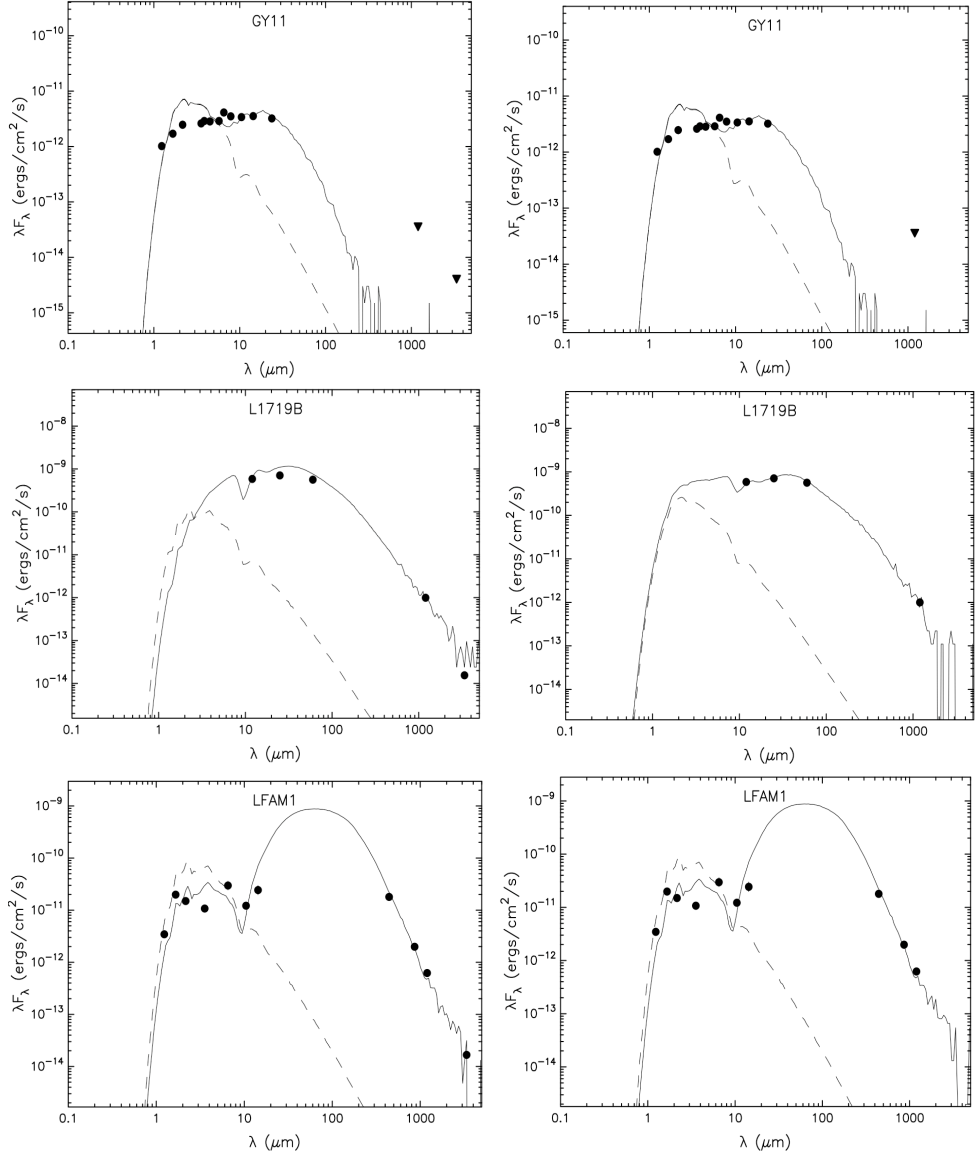


Figure 8.6: Left: The best fit SEDs including the 3.3 mm point for the Class FS sources. Right: The best fit SEDs not including the 3.3 mm point for the Flat Spectrum sources. Top: GY11, Middle: L1719B, Bottom: LFAM1.

A_V values were considered, from 0 to 20. The best fit models returned no preference for either a high A_V or a low A_V .

8.3.3 LFAM1

The models with and without the 3.3 mm data appear to fit this source very well, reduced χ^2 of 35. However, there is no data-point in the range between $14.3 \mu\text{m}$ and $450 \mu\text{m}$, which is where the model appears to have a large excess. If the source was as strong at these wavelengths as the models suggest then it should have been observed by MIPS. A far IR measurement of this source, whether it is a detection or upper limit, would greatly

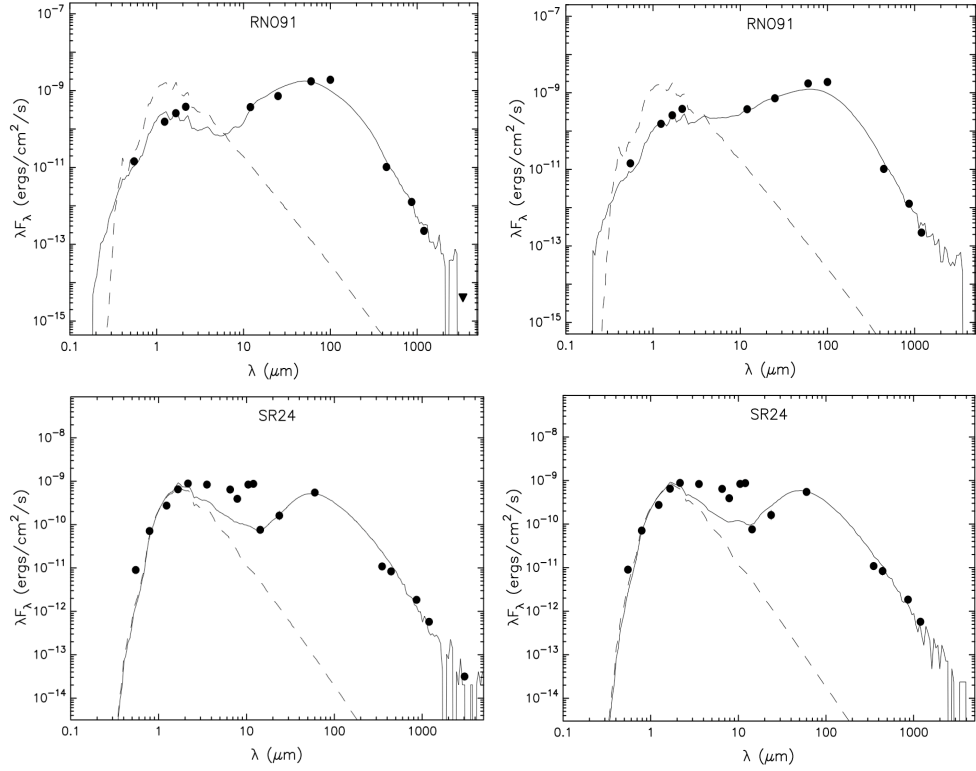


Figure 8.7: Left: The best fit SEDs including the 3.3 mm point for the Class FS sources. Right: The best fit SEDs not including the 3.3 mm point for the Flat Spectrum sources. Top: RNO91, Bottom: SR24.

constrain these models. The current best fit model is a massive envelope, $0.6 M_{\odot}$, and a near face-on small disk, $0.0003 M_{\odot}$.

8.3.4 RNO91

This source is best fit, reduced $\chi^2 = 18.4$, by a close to face-on system with a total circumstellar material mass of $\sim 0.2 M_{\odot}$. The models with and without the 3.3 mm data produce different results as to the location of this mass. The model including the 3.3 mm upper limit suggests that this source consists of mainly a massive envelope with a very small disk. While the model that does not include the 3.3 mm upper limit suggests the mass is more evenly spread between envelope and disk. In both cases the central star is very low mass, $\sim 0.15 M_{\odot}$, which is slightly lower than the current spectral type of M1 would suggest.

8.3.5 SR24

This source was not detected as part of this survey due to a failed observation. However, there is still enough literature data to build an SED for this source. The SED was then fitted using the routine but failed to produce a reliable fit.

8.4 Class II

The stellar parameters for the sources AS205 and SR21 are not shown as they are part of multiple systems. The best fit SEDs and their parameters calculated using the grid are shown in Figs. 8.8, 8.9, 8.10 & 8.11. Very few of the Class II sources have clear Class II models as most contain some amount of envelope flux. It would be expected for this class that the mean disk mass would be larger than the mean envelope mass. However, the mean masses are not greatly different from those of the Class I source. The mean envelope mass is $0.1 M_{\odot}$, while the mean disk mass is $0.01 M_{\odot}$. Although, the envelope mass has generally decreased and the disk mass has generally increased these two sets of sources do not appear to be significantly different. In many cases the far-IR flux appears as an outlier to the best fit model, in these cases it is obvious the models over estimate the amount of envelope material in these systems biasing the mean envelope mass towards higher values.

8.4.1 AS205

The optical, near-IR and submillimetre data-points for this source seem to fit very well. However, the far IR points do not appear to fit the model. This has resulted in a very high reduced χ^2 of 168, which does not improve greatly by not including the 3.3 mm data. Because of the high value for the reduced χ^2 we do not believe the parameters of the best fit model to be reliable.

8.4.2 DOAR25

The DOAR25 SED returns a very good fit to the same model both when including and not including the 3.3 mm data. This model is of a near face-on system with an A_V of 2.5, which compares well with the A_V measured by Wilking et al. (2005) of 2.9. The best fit model appears more like a Class I source than a Class II source, although the constructed SED does appear more like a Class II. The model fit appears to break down in the far-IR at the MIPS point, which is much lower than the model suggests. This is the wavelength where the envelope dominates the emission. Therefore, the envelope mass in the best fit model, $0.5 M_{\odot}$, may be an overestimate of the envelope mass. The disk mass in the best fit model is $0.008 M_{\odot}$.

8.4.3 DOAR44

The same model fits the SED with both the 3.3 mm point included and not included. This model provides a very good fit, reduced $\chi^2 = 15$, with no clear outlying points. An interstellar extinction of 2.12 is applied to this model. The model appears to be a Class II source but still contains a significant, but small, envelope. The disk has a mass of $0.01 M_{\odot}$, while the envelope mass is $0.0004 M_{\odot}$. The sources stellar parameters indicate a pre-main sequence star with a mass of $0.36 M_{\odot}$, which is comparable to that of the expected spectral type of K3.

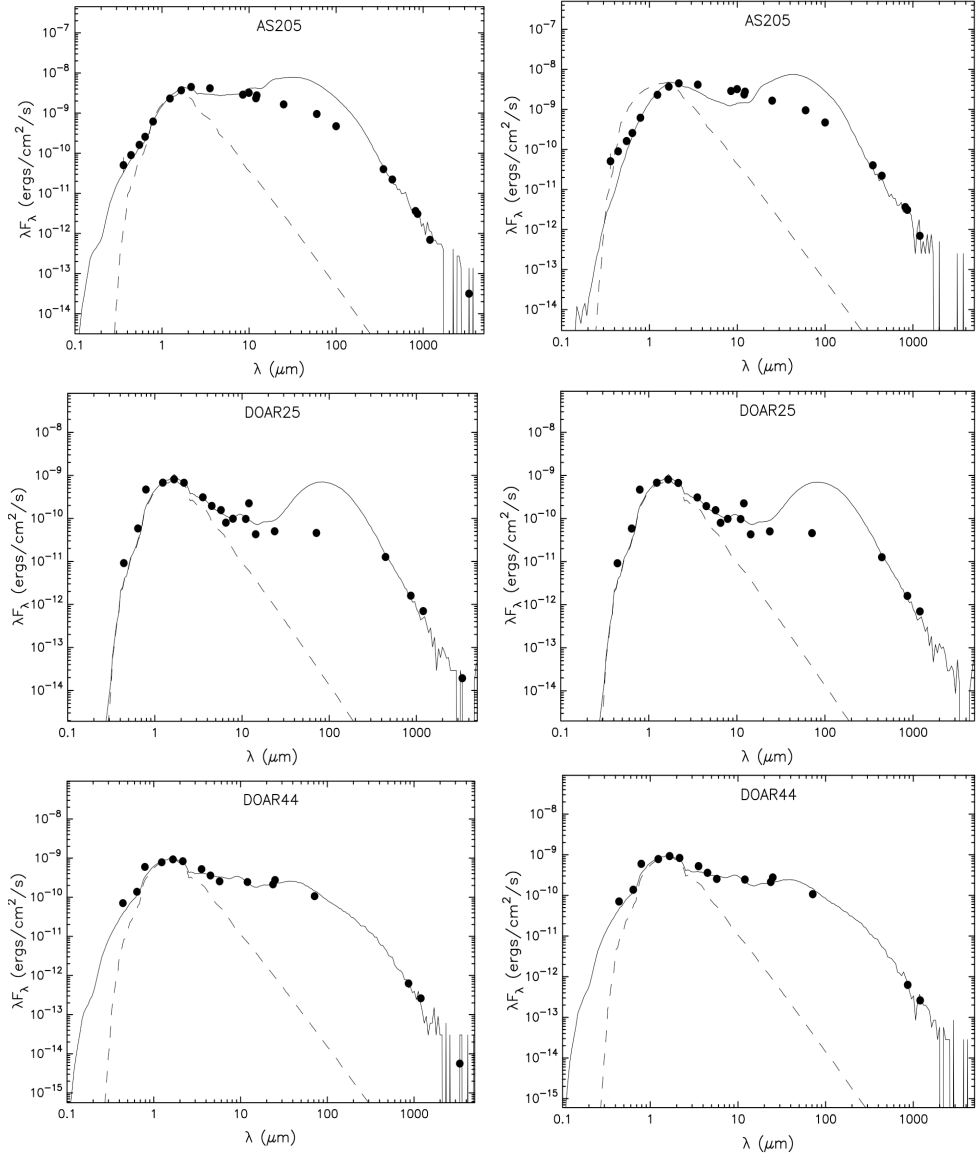


Figure 8.8: Left: The best fit SEDs including the 3.3 mm point for the Class II sources. Right: The best fit SEDs not including the 3.3 mm point for the Class II sources. Top: AS205, Middle: DOAR25, Bottom: DOAR44.

8.4.4 EL24

The best fit model to this source is a clear Class II source. Although the model indicates an envelope mass of $0.003 M_{\odot}$, the lack of other envelope parameters indicate that no envelope is considered, (Robitaille et al. 2007). The model system is viewed through an interstellar extinction of 11.92, and is viewed at $\sim 45^{\circ}$. The disk is relatively large, ~ 300 AU, and massive, $0.1 M_{\odot}$. However, this model has a very high central star mass of $3 M_{\odot}$, which does not fit with the known spectral type of K6. These stellar parameters introduce some doubt as to the reliability of the best fit model.

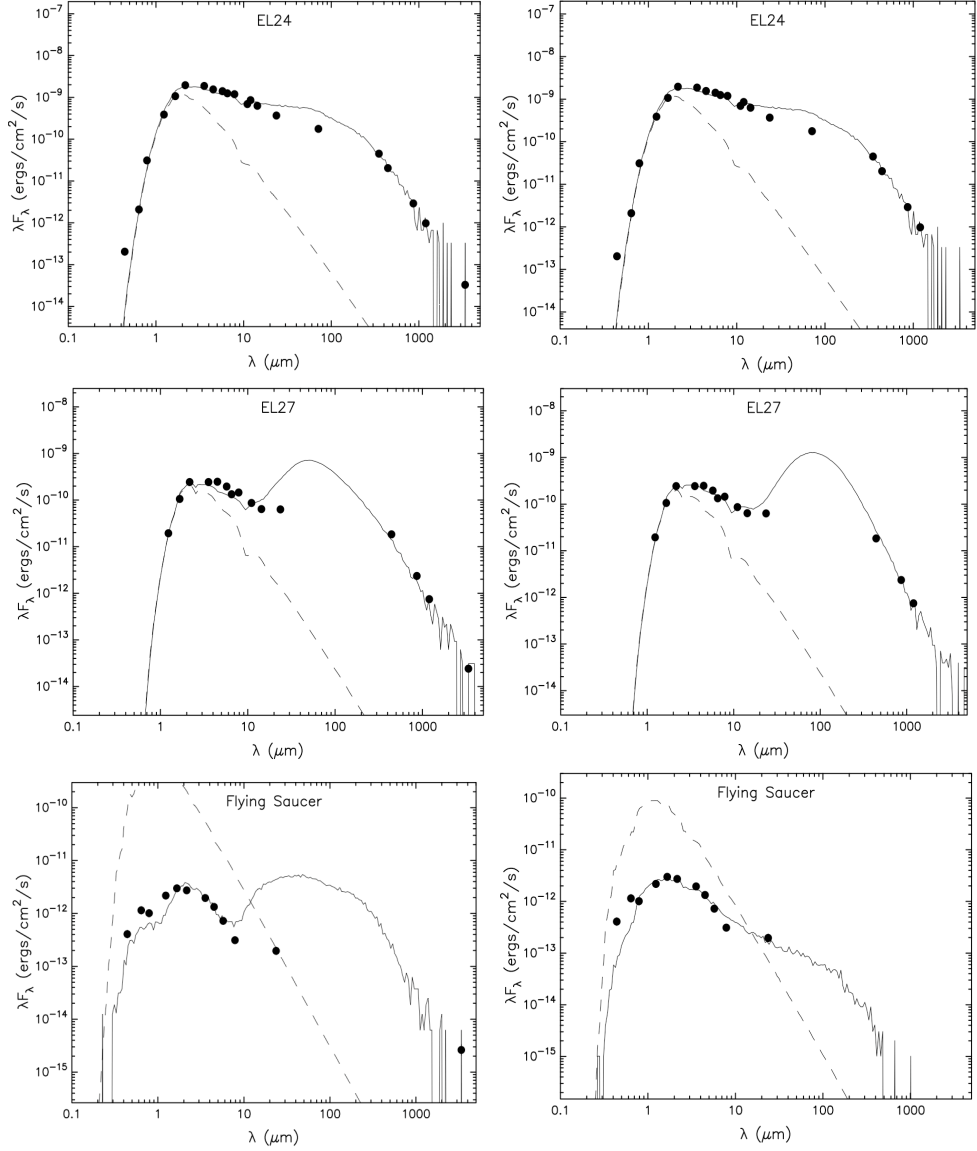


Figure 8.9: Left: The best fit SEDs including the 3.3 mm point for the Class II sources. Right: The best fit SEDs not including the 3.3 mm point for the Class II sources. Top: EL24, Middle: EL27, Bottom: Flying Saucer.

8.4.5 EL27

There is a large difference between the two best fit models depending on whether the 3.3 mm data is included. When including the 3.3 mm data the system appears more like a Class II system although there is still a great deal of envelope material. When this data-point is not included the model system has parameters that are more like a Class I source. Not including the 3.3 data the χ^2 is lowered by a factor of 3. Therefore, although the non 3.3 mm model does not appear to fit a Class II source it is taken as the more reliable model. This model is best fit with an A_V of 17.68, which is comparable to the measured A_V , 18.0, from COMPLETE. The envelope mass in the model is much higher

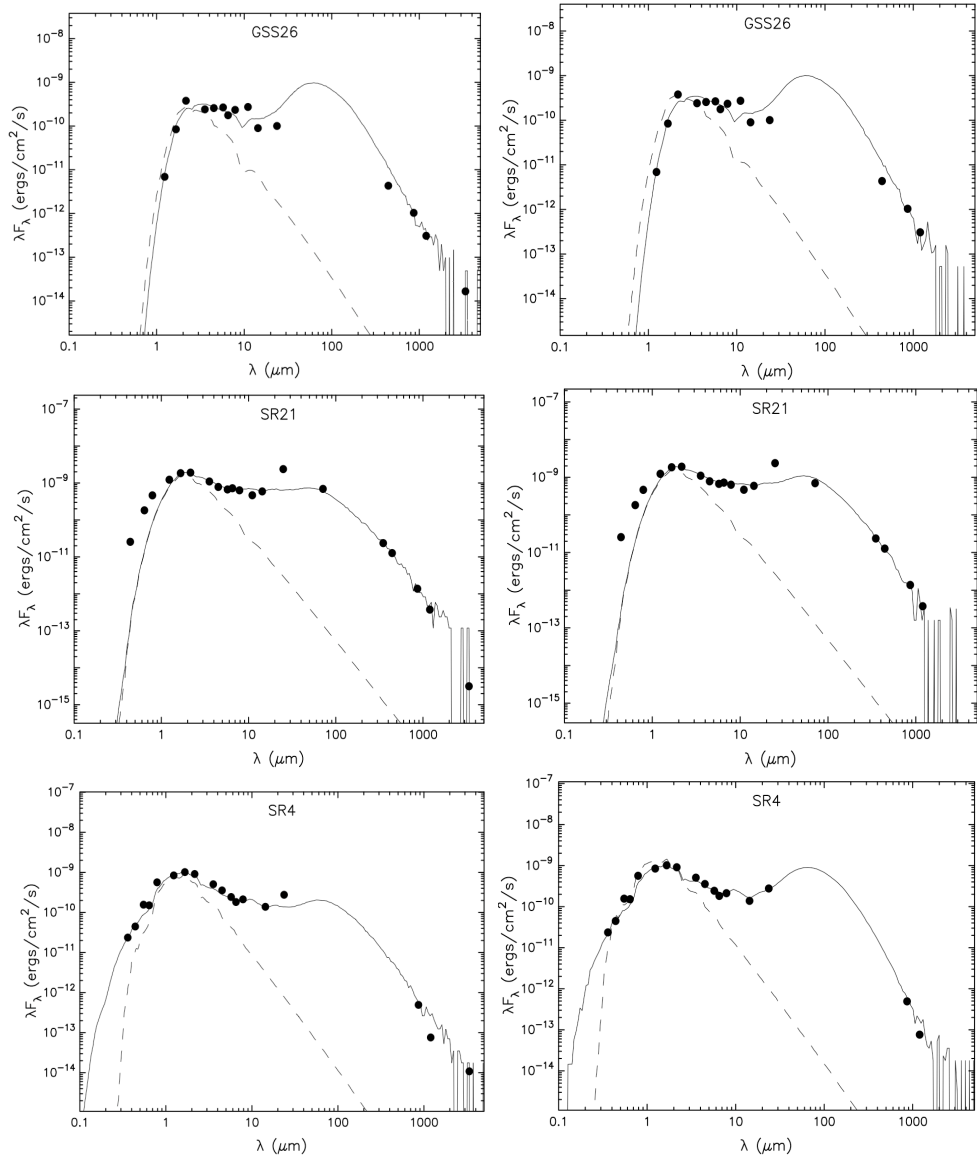


Figure 8.10: Left: The best fit SEDs including the 3.3 mm point for the Class II sources. Right: The best fit SEDs not including the 3.3 mm point for the Class II sources. Top: GSS26, Middle: SR21, Bottom: SR4.

than the disk mass, $0.3 M_{\odot}$ compared to $0.02 M_{\odot}$. However, this shows the system has a great deal of circumstellar material. Given that there is a great deal of circumstellar material modeled and the low dust opacity measured in Section 7, it would seem this system is a prime candidate for a possible planet forming system.

8.4.6 Flying Saucer

The 3.3 mm datapoint in this SED greatly constrains the possible best fit models for this source. Without the 3.3 mm point the best fit SEDs are all Class III, with little or no disk and envelope. Adding the 3.3 mm point requires a disk and so the best fit models are Class

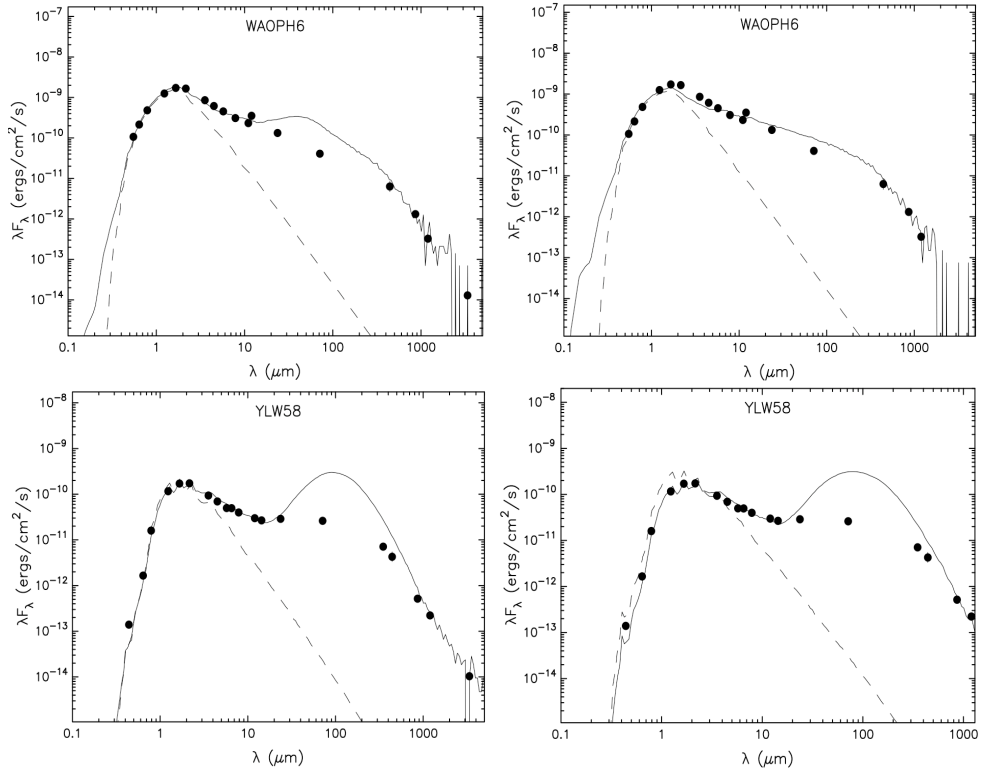


Figure 8.11: Left: The best fit SEDs including the 3.3 mm point for the Class II sources. Right: The best fit SEDs not including the 3.3 mm point for the Class II sources. Top: WAOPH6, Bottom: YLW58.

II. However, the detection of the Flying Saucer in this survey is marginal. Therefore, in order to further constrain this source many more far IR and submillimetre observations are required. Even without these data a decent fit, reduced $\chi^2 = 54$, can be achieved to a Class II model. This model fit a of an edge on disk, which the Flying Saucer is known to be, and an interstellar extinction of 0.64. The model has a disk mass of $0.01 M_{\odot}$, with no envelope.

8.4.7 GSS26

GSS26 is best fit by the same model whether or not you include the new 3.3 mm data. However, the best fit A_V changes greatly between the two models, from 18.2 to 15.8, neither of which are very close to the 21.3 measured by Barsony et al. (2005). The model has an acceptable reduced χ^2 of 61.6. This source lacks a far-IR point that would greatly constrain the envelope emission from this source as the best fit model appears to be a Class I source. The envelope and disk are comparable in mass, $0.07 M_{\odot}$ and $0.03 M_{\odot}$ respectively. The central stellar source has a mass of $0.55 M_{\odot}$, which appears to be slightly larger than the current spectral type suggests, K8.

8.4.8 SR21

The best fit including the 3.3 mm data for this source does not have a low enough reduced χ^2 , 103, for the best fit model to be considered reliable. By not including this data-point the reduced χ^2 is lowered sufficiently to produce an acceptable fit, $\chi^2 = 75$. This model is created assuming an $A_V = 8.00$, which is slightly lower than that measured by Prato et al. (2003), $A_V = 9.0$. This model continues to retain a large amount of envelope material, $0.04 M_\odot$, although the model SED does appear flatter than most that include envelopes. The best fit disk mass in this model is $0.02 M_\odot$.

8.4.9 SR4

This source produces one of the best χ^2 fits of all with a reduced χ^2 value of 12.8, when including the 3.3 mm data, and 10, when not including the 3.3 mm data. By eye, the model when not including the 3.3 mm data fits better. The MIPS $24 \mu\text{m}$ point appears to be an outlier in the best fit model when the 3.3 mm data are included, while it is clearly well fit in the other model. The model has a larger envelope than disk, which is surprising given the class of this source. The envelope has a mass of $0.1 M_\odot$, while the disk mass is $0.001 M_\odot$. The central star in this best fit model has a mass of $0.33 M_\odot$, which is reasonable for a star of K5 spectral type.

8.4.10 WAOPH6

WAOPH6 is another source that these models appear to fit very well with or without the new data. However, by eye the fit without the 3.3 mm data looks much better and so I take this to be the best fit model, reduced $\chi^2 = 8$. This model is produced using an A_V of 3.4, which is very close to that measured by Andrews & Williams (2007b), $A_V = 3.6$. This model requires a high mass central star, $1.78 M_\odot$, which at this stage in the pre-main sequence does not correspond to this sources spectral type of K6. The model is clearly a Class II model with a disk but no envelope. The best fit disk is $\sim 100 \text{ AU}$ in size and $0.04 M_\odot$ in mass.

8.4.11 YLW58

Although the best fit models when both including and not including the 3.3 mm data have reduced χ^2 values below the cut off level, they both seem to greatly over estimate the envelope emission in the far-IR. This results in the best fit models having high envelope masses, $0.2 M_\odot$, where perhaps the source would not have this massive an envelope. The best fit model contains very little circumstellar material in their disks, $0.0002 M_\odot$. Therefore, the best fit model is a Class I but due to the models clear over estimate of the far-IR flux this may not be reliable. The estimated stellar mass for the best fit model is $0.11 M_\odot$.

8.5 Class III

The Class III sources should be best fit with either a simple stellar blackbody or a stellar blackbody with a very small IR excess. The fitting routine failed to fit any model to the SED to the source GY29. All the models predict that the 3.3 mm point would have too low a flux to detect. Therefore, the 3.3 mm data from this survey does not change any of the best fit models. The best fit SEDs and their parameters calculated using the grid are shown in Fig. 8.12. There is a possible interesting transition system, GY12, and a system that should perhaps be a Class II system, ISO-Oph26.

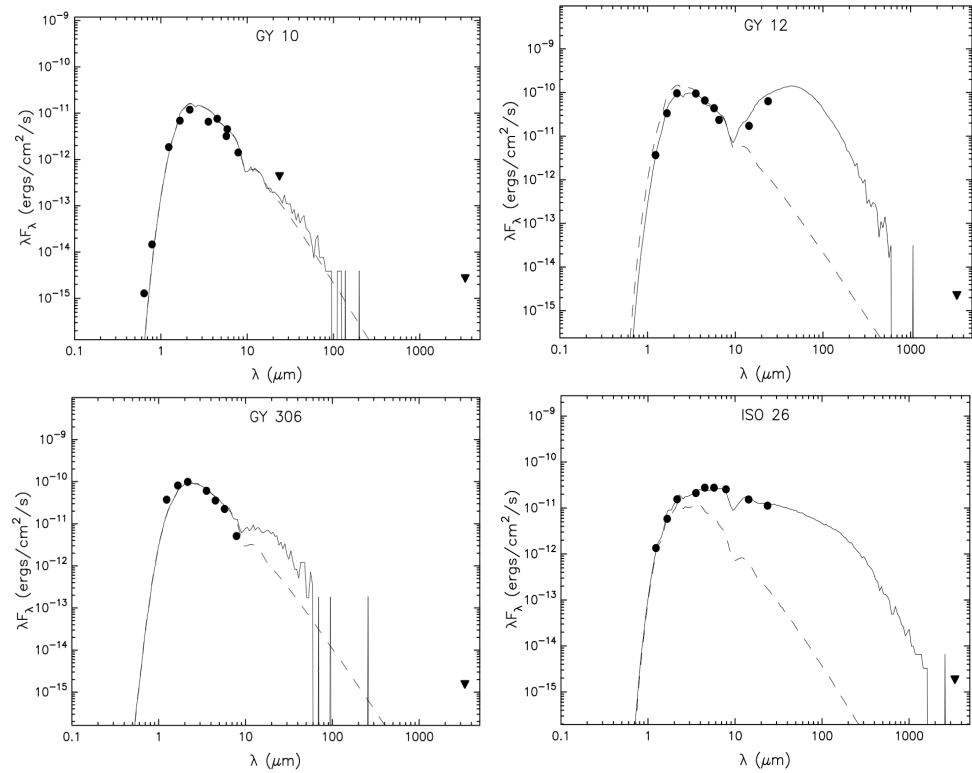


Figure 8.12: The best fit SEDs of the Class III sources. Top left: GY10, top right: GY12, bottom left: GY306 and bottom right: ISO-Oph 26. GY29 is not included as none of the models fitted the data.

8.5.1 GY10

The best fit model, reduced $\chi^2 = 37.1$, for this source has no circumstellar material and is simple a stellar blackbody. The high interstellar extinction for this source, $A_V = 19$, means that the stellar source needs to be fairly large to reproduce the SED. The stellar mass is $0.87 M_{\odot}$, which appears to be much larger than the spectral type of M9 suggests.

8.5.2 GY12

GY12 is the binary companion of the source LFAM1. The best fit model, reduced $\chi^2 = 3.26$, appears to indicate the possible presence of some remaining circumstellar material. However, this may be contamination from the nearby LFAM1. The two sources in this system are separated by $9.4''$, which is not much greater than the $6''$ beam size of Spitzer at $24\mu\text{m}$. If this excess is not then it would suggest this is an interesting object with no near or mid-IR excess and only a far-IR excess. This would indicate a evacuated cavity around the star with little or no disk. There still appears to be an envelope present although it is low mass, $0.005 M_{\odot}$. Assuming the far-IR excesses and not simply contamination from LFAM1 this is a possible system where a planet, or planets, have formed and cleared the inner regions and the disk.

8.5.3 GY306

The best fit model, reduced $\chi^2 = 23.7$, for this source does not exclude the possibility of there being a very small amount of remaining circumstellar material. However, the model is basically a blackbody fit of a $1.97 M_{\odot}$ central star through an interstellar extinction of 19. As for GY10, the stellar mass is much larger than the expected spectral type. This is likely to be due to the high value of interstellar extinction.

8.5.4 ISO-Oph 26

This source appears more like a Class II source with a disk and almost no remaining envelope. The best fit model, reduced $\chi^2 = 1.89$, has a disk mass of $0.001 M_{\odot}$ and a very low mass envelope, $0.000005 M_{\odot}$. This system is modeled as being face-on with an interstellar extinction = 19.45. The central star has a mass of $0.14 M_{\odot}$, which fits well with the known spectral type of M5.

Chapter 9

Conclusions

This work draws together a complete 1.3 mm flux-limited sample of the star formation evolution in ρ Ophiuchus. Additionally, five Class III sources are included in this study. By combining observations of pre-stellar dust condensations with the subsequent stages of pre-main sequence stellar evolution we have shown clear trends exist in dust mass and dust opacity throughout the early stages of a star formation. These data improve the current body of knowledge by also being the first survey at millimetre wavelengths with the possibility of spatially resolving this material, and 12 of the detected sources are at least partially resolved. The new 3.3 mm data presented in this thesis are combined with literature data to form complete SEDs of the sample source. The SEDs are then compared to the grid of models established by Robitaille et al. (2007) in an attempt to gain a more complete understanding of the properties of the sources and their circumstellar material.

9.1 Detections and Fluxes

This survey has a detection frequency of 47% across all the stages of evolution. All the Class 0, I and II sources are detected, while all the Class III sources are not detected. The starless have detection frequency of 15% and the Flat Spectrum sources have a detection frequency of 40%. We detect sources down to 2.74 mJy, the flux of the Class II source Flying Saucer. The starless sources appear strong at 1.3 mm, ~ 100 mJy, most are undetected in the OVRO data. This may be the result of high dust opacity indices that cause many of the sources to remain undetected at 3.3 mm. There is also the possibility that these sources are so extended that some of their emission is resolved out by the interferometer, which would result in a lower observed flux.

Both the Class 0 systems observed were strongly detected, with IRAS16293 resolved into its two separate Class 0 components. The Class 0 systems were also both resolved by the interferometer, indicating sizes between 130 AU to 1000 AU. Despite the Class I and Class II sources having similar fluxes at 1.3 mm the Class I fluxes (Andre & Montmerle 1994) are systematically lower than the Class II sources at 3.3 mm. This could be the result of the Class I sources having a higher dust opacity index, some of the material being resolved out by the interferometer, or contamination with local environment in the

larger 1.3 mm beam. Only two of ten Class I sources are resolved compared with 4 of eleven Class II. Of the resolved sources the sizes are comparable, ~ 500 AU. This size is more consistent with a disk as opposed to an envelope. The Flat Spectrum sources show a significantly reduced detection frequency with only 2 of the 5 being detected, excluding SR24 that was the subject of a failed observation. This decrease is most likely due to the misclassification of two objects, GY11 and LFAM15, as Flat Spectrum rather than Class III as determined by other studies (Wilking et al. 2005). The other non-detected source was RNO91, which is possibly due to the higher dust opacity index of this source compared to its classification. None of the Class III sources were detected, which was expected as they were not detected at 1.3 mm by Andre & Montmerle (1994).

9.2 Dust Opacity Index

The dust opacity index, β , was calculated in combination with literature data to determine the slope of the SED at wavelengths greater than $350 \mu\text{m}$. We see a trend of decreasing β throughout the evolutionary stages. This trend indicates a possible increase in the sizes of dust grains in the circumstellar material throughout the early phases of a stars formation. In particular there is a large variation from the starless sources to the Class II sources, which could be due to the early stages of planet formation.

The starless objects have the highest mean value for β . Many of those detected at 1.3 mm were not detected at 3.3 mm, indicating a steep slope to the SED and allowing lower limits to be placed on the sources possible β values. These lower limits are then incorporated with the detected source β values to produce a mean of 2.33 ± 0.38 , which is comparable to the opacity index measured for the ISM, $\beta \sim 2$. Therefore, these sources are likely to have seen no grain growth at this early stage of evolution prior to the central star forming. The material in these condensations is sparse and extended and, although these sources were chosen as they remained unresolved in the survey of Motte et al. (1998), there is still the possibility that the interferometric observations resolve out some of the flux from these starless clumps. This would result in our reported fluxes being lower than the total. Alternatively, the 1.3 mm flux may be contaminated by the local environment of the sources. Hence, it would have the effect of artificially increasing the β value.

The Class 0 sources have a mean β of 0.77. IRAS16293B with a $\beta = 0.28$ appears to be slightly outlying from the other two measured β values. This low value for IRAS16293B could be due to contamination from its binary component IRAS16293A, leading to higher values of flux for both these objects. These higher flux values at 3.3 mm would result in a shallower slope to the SED and thus a lower value of β . Both the 1.3 mm and 3.3 mm data have similar beam size, reducing the impact of resolved out flux. It is believed all these effects result in the β value calculated here being only a lower limit for the value of β for the Class 0 objects. The lower mean β for Class 0 objects indicates that there is possible grain growth between the starless phase and the Class 0 phase.

The Class I sources show a slight decrease in mean β from the Class 0 with a mean

value of 0.63. This decline could indicate further grain growth. Again some of the flux from the outer envelope could be resolved out, leading to a higher value of β , however, this effect cannot account for the large difference between the ISM value and the Class I value.

The Flat Spectrum sources in this survey have all previously been determined to be on the boundary between Flat Spectrum and Class I. The fact they show a higher mean opacity value than the Class I sources may be due to a misclassification. The source L1719B has also been classified as a Class I source (Andre & Montmerle 1994), and our data are consistent with a Class I object.

The Class II objects give the clearest indication of grain growth, given the difference between the mean β in these sources compared to the starless objects. The mean value of 0.21 cannot be fully accounted for by uncertainties in the measured fluxes. There is expected to be little or no envelope emission to be resolved out so these fluxes should come from the same dust producing the 1.3 mm flux. Even removing an estimated amount of optically thick contamination, $\sim 20\%$ (Andrews & Williams 2007a), at the shorter wavelengths would not result in a slope similar to that of the ISM. This β value can be replicated by including larger sized dust particles than those present in the ISM. Hence, the disks within these systems appear to show strong evidence of grain growth, which could be the beginnings of planet formation. In addition to the evidence towards grain growth in these systems, the Class I and Class II values of β are shown to be drawn from statistically difference base distributions. A Kolmogorov-Smirnov test was performed and shows a large difference, $D = 0.60$, between the two datasets. The validity of this argument would be greatly helped by the additional observations of more Class I and Class II sources, which is left as possible future work.

9.3 Dust Mass

The total mass of the circumstellar material around each source was calculated with two values of β . The first calculation assumed a constant β for all sources, which was done in order to compare our results with previous work that did not include a calculation of β . The second calculation was carried out including the value of β calculated from the previous section.

The first estimation yielded a similar evolutionary trend to that observed in the mean flux of each class, with the Class 0 sources having the highest mass followed by a large decrease to the more evolved objects. The dust masses ranged between $0.006 M_{\odot}$ and $0.379 M_{\odot}$ with almost 40% of the sources having a dust mass greater than the MMSN. This indicates that these systems have at least enough mass in their circumstellar environments to produce systems similar to the Solar System.

The second calculation of dust mass appears slightly more revealing, with the starless sources now appearing more massive due to their large values of β . The three Flat Spectrum are also significantly changed by the inclusion of β in the calculation. The large

β value and high flux of L1719 result in a dust mass approaching that of the Class 0 sources. This, combined with the lower limit on β for RNO91 indicating a high β value, means the Flat Spectrum sources stand out. However, this is again thought to be simply because these sources could be classified as Class I sources. If these Flat Spectrum objects were re-classified as Class I then their high β values and high dust masses would not stand out and there would be a clear trend in dust mass through the evolutionary stages.

9.4 SED Fitting

The 3.3 mm data from this survey for 34 sources were combined with literature data to construct SEDs, which were then fit using the online tool of Robitaille et al. (2007). Of the 34 sources fitted, 27 best fit models had a reduced χ^2 of less than 100, which was the cut-off imposed. The distance was restricted to $150 \text{ pc} \pm 10$, while the interstellar extinction was restricted to within ± 5 of a value from the literature. The best fit SED models generally return more circumstellar material than the basic calculations carried out in the previous sections inferred.

The starless and Class 0 object are best fit by models with massive envelopes between 0.1 and $10 M_{\odot}$, with comparatively small disks. This indicates the systems have not had time for the infalling envelope to form much of a disk and begin accreting onto the star, or in the case of the starless objects compress to form a star.

Most the Class I sources have an envelope that is more massive than the disk, with only IRS43 having a massive disk. All the sources showed larger disks and smaller envelopes than the Class 0 sources.

The best fit models for the Class II sources do not appear to fit the standard picture of the Class II stage, as most retain envelopes based on the SED fit. Not only were envelopes present but in four of the sources the envelope was more massive than the disk. It is when modeling the Class II sources we see the limitations of the modeling. Many of the models fail to fit the far-IR data with any reliability, with the $70 \mu\text{m}$ MIPS data-point being particularly affected. For the four sources with large envelopes the observed MIPS data-point is clearly below the best fit model, indicating the best fit model is greatly overestimating the envelope emission. Overall these models provide a good first estimate of the parameters for these sources but modeling on a source by source basis is required in order to gain more reliable properties of each source.

9.5 Further work

This 3.3 mm data extends the range of current observations past the regime that the SED fitting models are accurate currently. In future these models will be improved (Whitney, private communication) and more extensive fitting can be performed using these data, which when combined with other possible new data will further constrain the emission from these very young sources.

In addition to extending the possible modeling work, observations with a more compact configuration would then allow a determination of how much flux is resolved out by the current interferometer data. This is most important for the 12 sources larger than point sources. Furthermore, observations in the more extended configuration would allow all the sources of this survey to be spatially resolved.

Finally, these data could be supplemented with much more sensitive and higher resolution observations using ALMA, the next generation submm/mm interferometer. With ALMA it will be possible to resolve these disks to provide disk sizes and inclination angles for all these sources. With the disk size and inclination fixed by ALMA the modeling becomes even more constrained resulting in disks with well known properties.

Appendices

Appendix A

Calibration and Analysis Scripts

A.1 Data Reduction Script

This shell script is an example of the reduction script used to calibrate the raw visibilities:

```
#!/bin/csh
```

```
ls
```

```
    echo "Input Raw Visibility File"
```

```
    set vis = 1
```

Baseline length calibration:

```
    uvedit vis=vis out=vis.bp apfile=antpos.071121
```

```
    set bl=vis.bp
```

Calibrate bandpass with respect to the auto-correlations:

```
    uvcal vis=bl out=autocal options=fxcal
```

```
    set auto=autocal
```

Remove autocorrelations:

```
    uvcat vis=auto select="-auto" out=auto.no options=nocal,nopass
```

```
    set data = auto.no
```

Bandpass calibrate the wide bands, need to change calibrator:

```
    mfcalf vis=data select="source(3C111),time(02:10:37.5,02:50:37.0)" interval=1.0
```

```
    refant=9
```

```
    uvcat vis=data out=data.bp options=nocal
```

```
    set bpw = data.bp
```

Gain calibrate 500MHz data:

```
    selfcal vis=bpw select="source(URANUS,0530+135)" interval=20.0 refant=9
```

```
    uvcat vis=bpw out=wbnoflux.mir
```

Determine the absolute flux value:

```
    bootflux vis=wbnoflux.mir taver=5.0 select=source"(0530+135,URANUS)"
```

```
    primary=URANUS line=chan,1,1,45,45 > flux.log
```

Insert the corrected flux from bootflux:

```
    echo "Input the gain calibrator flux from bootflux"
```

```
set flux = <
```

Absolute flux calibrate the data:

```
selfcal vis=bpw select="source(0530+135)" options=amp interval=20.0 refant=9  
flux=flux  
uvcat vis=wbnoflux.mir out=widecal.mir
```

A.2 Data Analysis Script

This shell script is an example of the mapping script used to turn the calibrated *u-v* visibilities into a source map:

Select source:

```
echo "Target to be mapped?"  
set source = iras16293  
invert vis=widecal.mir map=dm beam=bm line=chan,1,1,15 imsize=256 cell=0.5  
"select=source(source)" robust=-2.0
```

Clean and Restor map:

```
clean map=dm beam=bm out=cl niters=250 region=quarter  
restor map=dm beam=bm model=cl out=ma
```

Make contour map, offset in pixels map and RA/DEC image map:

```
cgdisp in=ma type=contour lines=3,3,3,3,3 slew=a,3.18E-3 levsl=5,10,15,20,25,30,35,40,45,50  
labtyp=hms,dms device=source.cont.ps/VCPS region=quarter beamtyp=b,l,3  
cgdisp in=ma labtyp=arcsec device=source.pix.ps/VCPS beamtyp=b,l,3 region=quarter  
cgdisp in=ma labtyp=hms,dms device=source.coords.ps/VCPS beamtyp=b,l,3 re-  
gion=quarter
```

Appendix B

Best Fit SED Parameters and Literature data

B.1 Starless

Source Name	850 μ m Flux ¹	1.1 mm Flux ²	1.2 mm Flux ³	1.3 mm Flux ⁴
A-MM1	*	50
A-MM2	964	90
A-MM3	*	55
A-MM7	450	85
A3-MM7	60	110
A-S	70	90
B2-MM7	100
B2-MM8	630	...	230	215
B2-MM10	400	280	...	160
B2-MM14	130
B2-MM15	460	530	125	90
B2-MM16	**	100
B2-MM17	...	400	2900	90

Table B.1: Table containing the literature data for the starless core objects. Fluxes are quoted in mJy. * The 1.2 mm flux for A-MM2 includes A-MM1 and A-MM3 within the beam size. ** The 1.2 mm flux for B2-MM17 also contains B2-MM16 in the beam size. 1: Johnstone et al. (2000) 2: Young et al. (2006) 3: Stanke et al. (2006), 4: Motte et al. (1998)

B.2 Class 0

Envelope Accretion Rate (Msol/yr)	2.86e-4	Envelope Accretion Rate (Msol/yr)	2.38e-4
Envelope Outer Radius (AU)	7.61e+3	Envelope Outer Radius (AU)	1.50e+3
Envelope Cavity Angle (degrees)	8.6	Envelope Cavity Angle (degrees)	15.7
Envelope Inner Radius (Rsub)	1.00e+0	Envelope Inner Radius (Rsub)	3.73e+0
Disk Mass (Msol)	4.15e-3	Disk Mass (Msol)	4.41e-2
Disk Outer Radius (AU)	5.72e+0	Disk Outer Radius (AU)	2.91e+1
Disk Inner Radius (Rsub)	1.00e+0	Disk Inner Radius (Rsub)	3.73e+0
Disk Inner Radius (AU)	3.96e-1	Disk Inner Radius (AU)	6.85e-1
Disk Scaleheight factor	0.861	Disk Scaleheight factor	0.790
Disk Flaring Power	1.123	Disk Flaring Power	1.107
Disk Accretion Alpha	2.72e-2	Disk Accretion Alpha	3.50e-3
Envelope Cavity density (cgs)	6.30e-20	Envelope Cavity density (cgs)	4.77e-20
Ambient density (cgs)	5.59e-22	Ambient density (cgs)	2.65e-22
Disk accretion rate (Msol/yr)	9.60e-7	Disk accretion rate (Msol/yr)	2.09e-7
A_v [circumstellar] (mag)	1.07e+3	A_v [circumstellar] (mag)	2.01e+3
Total Luminosity	3.58e+1	Total Luminosity	7.75e+0
Disk Scaleheight at 100AU	7.03	Disk Scaleheight at 100AU	7.17
Envelope Mass	1.08e+1	Envelope Mass	1.33e+0

Figure B.1: Left: The best fit SED's associated parameters for the source IRAS16293. Right: The best fit SED's associated parameters for the source LFAM5. The units for each parameter are given in brackets, except envelope mass that is in M_{\odot} . The main parameters to pick out are the disk mass and the envelope mass.

Source Name	4.5 μm Flux ¹	8 μm Flux ¹	24 μm Flux ¹	50 μm Flux ²	60 μm Flux ²	70 μm Flux ²	80 μm Flux ²	90 μm Flux ²	100 μm Flux ²	125 μm Flux ²
IRAS16293	0.043	0.2	615	150000	350000	640000	940000	1180000	1320000	1590000
LFAM 5	40.4

Table B.2: Table containing the literature data for observations at $\leq 125 \mu\text{m}$ used to build the SEDs for the Class 0 objects. Fluxes are quoted in mJy. 1: Spitzer Data 2: Correia et al. (2004)

Source Name	150 μm Flux ¹	175 μm Flux ¹	190 μm Flux ¹	350 μm Flux	450 μm Flux	800 μm Flux	850 μm Flux	1.1 mm Flux ²	1.2 mm Flux	1.3 mm Flux	2.7 mm Flux ⁴
IRAS16293	1590000	1360000	1100000	...	144300 ¹	...	23700 ¹	4470	...	1790 ³	1017
LFAM 5	40100 ⁵	39500 ⁵	5000 ⁵	13760 ⁵	...	1205 ⁶	1460 ⁵	72.1

Table B.3: Table containing the literature data for observations at $\geq 125 \mu\text{m}$ used to build the SEDs for the Class 0 objects. Fluxes are quoted in mJy. 1: Correia et al. (2004) 2: Young et al. (2006) 3: Bottinelli et al. (2004) 4: Looney et al. (2000) 5: Andre et al. (1993) 6: Stanke et al. (2006)

B.3 Class I

Envelope Accretion Rate (Msol/yr)	1.25e-5	Envelope Accretion Rate (Msol/yr)	3.75e-6
Envelope Outer Radius (AU)	3.25e+3	Envelope Outer Radius (AU)	1.07e+3
Envelope Cavity Angle (degrees)	23.9	Envelope Cavity Angle (degrees)	8.9
Envelope Inner Radius (Rsub)	1.00e+0	Envelope Inner Radius (Rsub)	1.00e+0
Disk Mass (Msol)	2.39e-3	Disk Mass (Msol)	5.81e-4
Disk Outer Radius (AU)	2.26e+2	Disk Outer Radius (AU)	1.46e+1
Disk Inner Radius (Rsub)	1.00e+0	Disk Inner Radius (Rsub)	1.00e+0
Disk Inner Radius (AU)	1.05e-1	Disk Inner Radius (AU)	1.94e-1
Disk Scaleheight factor	0.873	Disk Scaleheight factor	0.994
Disk Flaring Power	1.143	Disk Flaring Power	1.043
Disk Accretion Alpha	7.50e-3	Disk Accretion Alpha	1.27e-2
Envelope Cavity density (cgs)	3.13e-20	Envelope Cavity density (cgs)	2.68e-20
Ambient density (cgs)	2.25e-22	Ambient density (cgs)	1.09e-22
Disk accretion rate (Msol/yr)	2.94e-9	Disk accretion rate (Msol/yr)	4.00e-8
A_v [circumstellar] (mag)	3.97e+1	A_v [circumstellar] (mag)	9.94e+0
Total Luminosity	2.60e+0	Total Luminosity	8.69e+0
Disk Scaleheight at 100AU	10.35	Disk Scaleheight at 100AU	5.84
Envelope Mass	2.69e-1	Envelope Mass	1.23e-2
Stellar Age (yr)	1.94e+4	Envelope Accretion Rate (Msol/yr)	7.28e-7
Stellar Mass (Msol)	0.13	Envelope Outer Radius (AU)	1.04e+3
Stellar Radius (Rsol)	3.55	Envelope Cavity Angle (degrees)	16.9
Stellar Temperature (K)	2788	Envelope Inner Radius (Rsub)	1.00e+0
Envelope Accretion Rate (Msol/yr)	3.58e-5	Disk Mass (Msol)	1.49e-2
Envelope Outer Radius (AU)	1.73e+3	Disk Outer Radius (AU)	1.47e+1
Envelope Cavity Angle (degrees)	23.4	Disk Inner Radius (Rsub)	1.00e+0
Envelope Inner Radius (Rsub)	1.00e+0	Disk Inner Radius (AU)	1.22e-1
Disk Mass (Msol)	1.03e-2	Disk Scaleheight factor	0.886
Disk Outer Radius (AU)	4.00e+1	Disk Flaring Power	1.173
Disk Inner Radius (Rsub)	1.00e+0	Disk Accretion Alpha	7.59e-2
Disk Inner Radius (AU)	5.33e-2	Envelope Cavity density (cgs)	2.43e-20
Disk Scaleheight factor	0.886	Ambient density (cgs)	1.00e-22
Disk Flaring Power	1.092	Disk accretion rate (Msol/yr)	3.10e-6
Disk Accretion Alpha	1.80e-3	A_v [circumstellar] (mag)	6.81e+0
Envelope Cavity density (cgs)	7.71e-21	Total Luminosity	4.46e+0
Ambient density (cgs)	1.00e-22	Disk Scaleheight at 100AU	16.57
Disk accretion rate (Msol/yr)	1.29e-8	Envelope Mass	4.46e-3
A_v [circumstellar] (mag)	5.09e+1	Stellar Age (yr)	7.52e+4
Total Luminosity	6.99e-1	Stellar Mass (Msol)	0.12
Disk Scaleheight at 100AU	7.15	Stellar Radius (Rsol)	2.51
Envelope Mass	4.78e-1	Stellar Temperature (K)	2841
Stellar Age (yr)	1.55e+5	Envelope Accretion Rate (Msol/yr)	1.88e-5
Stellar Mass (Msol)	1.28	Envelope Outer Radius (AU)	1.56e+3
Stellar Radius (Rsol)	7.44	Envelope Cavity Angle (degrees)	9.9
Stellar Temperature (K)	4221	Envelope Inner Radius (Rsub)	1.00e+0
Envelope Accretion Rate (Msol/yr)	2.22e-5	Disk Mass (Msol)	7.75e-3
Envelope Outer Radius (AU)	6.60e+3	Disk Outer Radius (AU)	6.05e+1
Envelope Cavity Angle (degrees)	42.0	Disk Inner Radius (Rsub)	1.00e+0
Envelope Inner Radius (Rsub)	1.00e+0	Disk Inner Radius (AU)	3.92e-2
Disk Mass (Msol)	2.41e-2	Disk Scaleheight factor	0.704
Disk Outer Radius (AU)	1.47e+2	Disk Flaring Power	1.126
Disk Inner Radius (Rsub)	1.00e+0	Disk Accretion Alpha	2.20e-3
Disk Inner Radius (AU)	2.65e-1	Envelope Cavity density (cgs)	6.13e-21
Disk Scaleheight factor	0.835	Ambient density (cgs)	1.00e-22
Disk Flaring Power	1.111	Disk accretion rate (Msol/yr)	6.74e-9
Disk Accretion Alpha	3.20e-3	A_v [circumstellar] (mag)	6.56e+1
Envelope Cavity density (cgs)	4.00e-21	Total Luminosity	3.78e-1
Ambient density (cgs)	5.29e-22	Disk Scaleheight at 100AU	8.72
Disk accretion rate (Msol/yr)	1.84e-8	Envelope Mass	2.50e-1
A_v [circumstellar] (mag)	3.89e+1		
Total Luminosity	1.59e+1		
Disk Scaleheight at 100AU	5.92		
Envelope Mass	4.98e-1		

Figure B.2: The best fit SED's associated parameters of the Class I sources, from top CRBR12, EL21, GY91, IRS43, L1689 and LFAM26. The units for each parameter are given in brackets, except envelope mass that is in M_{\odot} .

Source Name	J Band Flux ¹	H Band Flux ¹	K Band Flux ¹	3.6 μm Flux ³	4.5 μm Flux ³	5.8 μm Flux ³	6.7 μm Flux ⁴	8 μm Flux ³	10 μm Flux ⁵	12 μm Flux ⁶	14.3 μm Flux ⁴
CRBR12	...	0.63	10.2	45.0	87.7	161	246	237	315	...	363
EL21	4.46 ²	49.0 ²	305 ²	184	4090	5400	8520	...	19100
GY91	0.12	0.53	7.7	30.4	44.8	60.5	89.0	82.8	157	...	158
IRS43	...	4.01	84.3	629	1240	1790	2210	2190	2060	...	4430
L1689S	0.2	3.06	34.2	299	731	1060	982	1310	1170
L1709B	1.0	19	137	589	957	1250	...	1450	...	1190	...
LFAM26	1.11	6.1	10.9	16.6	32	29.6	64
LFAM30	4.41	32	97	127	143	140	151	99	490	...	782
YLW2	0.32	3.2	15.2	239	744	1610	1270	2240	1970	...	2570
YLW46A	94.6	305	618	1410	1600	4060	5870	6000	6204	6343	6490

Table B.4: Table containing the literature data for observations at $\leq 14.3 \mu\text{m}$ used to build the SEDs for the Class I objects. Fluxes are quoted in mJy. 1: Skrutskie et al. (2006) 2: Duchêne et al. (2004) 3: Spitzer IRAC data from IRSA 4: Bontemps et al. (2001) 5: Barsony et al. (2005) 6: Beichman et al. (1988)

Source Name	24 μm Flux ¹	70 μm Flux ¹	350 μm Flux ²	450 μm Flux ²	800 μm Flux ⁴	850 μm Flux ²	1.1 mm Flux ⁵	1.2 mm Flux ⁶	1.3 mm Flux ⁷	2.7 mm Flux ⁸
CRBR12	516	290 ³	...	126	85	...
EL21	...	80500	...	1403	...	222	90	...
GY91	393	340	300	...
IRS43	...	34400	...	1811	400	246	...	193	75	...
L1689S	...	66400	...	1687	...	394	190	...	150	...
L1709B	3230	10400	6703	4729	1170	1017	500	...	370	...
LFAM26	459	3490	440	...	433	100	...
LFAM30	816	15700	...	400	...	182	47	12.9
YLW2	...	8120	...	749	360	216	...	117	115	...
YLW46A	...	20800	180	60	...

Table B.5: Table containing the literature data for observations at $> 14.3 \mu\text{m}$ used to build the SEDs for the Class I objects. Fluxes are quoted in mJy. 1: Spitzer MIPS data from IRS A 2: Andrews & Williams (2007a) 3: Jørgensen et al. (2008) 4: Dent et al. (1998) 5: Young et al. (2006) 6: Stanke et al. (2006) 7: Andre & Montmerle (1994) 8: Barsony et al. (2002)

B.4 Flat Spectrum

Stellar Age (yr)	8.09e+6	Stellar Age (yr)	1.10e+3
Stellar Mass (Msol)	0.43	Stellar Mass (Msol)	0.15
Stellar Radius (Rsol)	0.87	Stellar Radius (Rsol)	5.04
Stellar Temperature (K)	3683	Stellar Temperature (K)	2847
Envelope Accretion Rate (Msol/yr)	0	Envelope Accretion Rate (Msol/yr)	9.28e-7
Envelope Outer Radius (AU)	-	Envelope Outer Radius (AU)	3.92e+3
Envelope Cavity Angle (degrees)	-	Envelope Cavity Angle (degrees)	2.5
Envelope Inner Radius (Rsub)	-	Envelope Inner Radius (Rsub)	1.00e+0
Disk Mass (Msol)	8.84e-6	Disk Mass (Msol)	1.54e-2
Disk Outer Radius (AU)	6.28e+2	Disk Outer Radius (AU)	2.68e+0
Disk Inner Radius (Rsub)	2.80e+1	Disk Inner Radius (Rsub)	1.00e+0
Disk Inner Radius (AU)	8.53e-1	Disk Inner Radius (AU)	8.75e-2
Disk Scaleheight factor	0.929	Disk Scaleheight factor	0.906
Disk Flaring Power	1.141	Disk Flaring Power	1.096
Disk Accretion Alpha	1.80e-3	Disk Accretion Alpha	1.50e-3
Envelope Cavity density (cgs)	-	Envelope Cavity density (cgs)	4.12e-20
Ambient density (cgs)	2.01e-22	Ambient density (cgs)	1.01e-22
Disk accretion rate (Msol/yr)	3.53e-13	Disk accretion rate (Msol/yr)	5.53e-7
A_v [circumstellar] (mag)	4.53e-4	A_v [circumstellar] (mag)	2.43e+1
Total Luminosity	1.26e-1	Total Luminosity	2.00e+0
Disk Scaleheight at 100AU	5.66	Disk Scaleheight at 100AU	10.37
Envelope Mass	3.51e-7	Envelope Mass	4.34e-2
Stellar Age (yr)	5.30e+4	Stellar Age (yr)	5.16e+3
Stellar Mass (Msol)	0.20	Stellar Mass (Msol)	0.15
Stellar Radius (Rsol)	3.28	Stellar Radius (Rsol)	4.64
Stellar Temperature (K)	3051	Stellar Temperature (K)	2871
Envelope Accretion Rate (Msol/yr)	2.53e-5	Envelope Accretion Rate (Msol/yr)	1.09e-5
Envelope Outer Radius (AU)	2.85e+3	Envelope Outer Radius (AU)	3.08e+3
Envelope Cavity Angle (degrees)	10.6	Envelope Cavity Angle (degrees)	8.4
Envelope Inner Radius (Rsub)	2.20e+2	Envelope Inner Radius (Rsub)	5.85e+1
Disk Mass (Msol)	2.77e-4	Disk Mass (Msol)	5.49e-5
Disk Outer Radius (AU)	2.59e+2	Disk Outer Radius (AU)	5.01e+0
Disk Inner Radius (Rsub)	2.20e+2	Disk Inner Radius (Rsub)	5.85e+1
Disk Inner Radius (AU)	1.30e+1	Disk Inner Radius (AU)	4.71e+0
Disk Scaleheight factor	0.898	Disk Scaleheight factor	0.771
Disk Flaring Power	1.089	Disk Flaring Power	1.097
Disk Accretion Alpha	4.72e-2	Disk Accretion Alpha	9.79e-2
Envelope Cavity density (cgs)	6.84e-21	Envelope Cavity density (cgs)	1.59e-20
Ambient density (cgs)	1.31e-22	Ambient density (cgs)	1.01e-22
Disk accretion rate (Msol/yr)	2.23e-9	Disk accretion rate (Msol/yr)	2.99e-7
A_v [circumstellar] (mag)	3.59e+1	A_v [circumstellar] (mag)	4.28e+1
Total Luminosity	8.41e-1	Total Luminosity	1.56e+0
Disk Scaleheight at 100AU	7.58	Disk Scaleheight at 100AU	8.64
Envelope Mass	6.46e-1	Envelope Mass	3.50e-1

Figure B.3: The best fit SED's associated parameters of the Flat Spectrum sources GY11, L1719, LFAM1 and RNO91. The units for each parameter are given in brackets, except envelope mass that is in M_{\odot} .

Source Name	V Band Flux	I Band Flux	J Band Flux ⁴	H Band Flux ⁴	K Band Flux ⁴	3.6 μm Flux ⁵	4.5 μm Flux ⁵	5.8 μm Flux ⁵	6.7 μm Flux ⁶	8.0 μm Flux ⁵
GY11	0.42	0.95	1.78	3.1	4.26	5.53	9.0	9.2
L1719B
LFAM1	10.8	15.8	45.1	37.8	66	...
RNO91	2.64 ¹	...	63.8	143	274	19	...
SR24	1.65 ²	18.7 ³	200	555	1000	838	990	...	1410	1040

Table B.6: Table containing the literature data for observations at $\leq 8 \mu\text{m}$ used to build the SEDs for the Flat Spectrum objects. Fluxes are quoted in mJy. 1: Herbig & Bell (1988) 2: Correia et al. (2006) 3: Wilking et al. (2005) 4: Skrutskie et al. (2006) 5: Spitzer IRAC data from IRSA 6: Bontemps et al. (2001)

Source Name	10 μ m Flux ¹	12 μ m Flux ²	14.3 μ m Flux ³	24 μ m Flux ⁴	25 μ m Flux ³	60 μ m Flux ³	100 μ m Flux ³	350 μ m Flux ⁵	450 μ m Flux ⁵	850 μ m Flux ⁵	1.1 mm Flux ⁶	1.2 mm Flux ⁷	1.3 mm Flux ⁸
GY11	11.9	...	17	25.6
L1719B	...	2360	5930	11330	400
LFAM1	42.9	...	119	2662	1030	1610	1060	370
RNO91	...	1500	6050	35310	64400	...	1524	365	90
SR24	2940	3500	2290	1320	6300	11000	...	1271	1263	530	...	228	280

Table B.7: Table containing the literature data for the observations between 10 μ m and 100 μ m used to build the SEDs for the Flat Spectrum objects. Fluxes are quoted in mJy. 1: Barsony et al. (2005) 2: Beichman et al. (1988) 3: Bontemps et al. (2001) 4: Spitzer MIPS from IRS A 5: Andrews & Williams (2007a) 6: Young et al. (2006) 7: Stanke et al. (2006) 8: Andre & Montmerle (1994)

B.5 Class II

Stellar Age (yr)	1.60e+5	Stellar Age (yr)	6.16e+5
Stellar Mass (Msol)	0.35	Stellar Mass (Msol)	0.36
Stellar Radius (Rsol)	3.01	Stellar Radius (Rsol)	2.81
Stellar Temperature (K)	3481	Stellar Temperature (K)	3518
Envelope Accretion Rate (Msol/yr)	2.65e-5	Envelope Accretion Rate (Msol/yr)	5.72e-8
Envelope Outer Radius (AU)	3.51e+3	Envelope Outer Radius (AU)	1.16e+3
Envelope Cavity Angle (degrees)	35.5	Envelope Cavity Angle (degrees)	30.5
Envelope Inner Radius (Rsub)	1.00e+0	Envelope Inner Radius (Rsub)	6.80e+0
Disk Mass (Msol)	8.99e-3	Disk Mass (Msol)	1.25e-2
Disk Outer Radius (AU)	5.68e+1	Disk Outer Radius (AU)	7.78e+1
Disk Inner Radius (Rsub)	1.00e+0	Disk Inner Radius (Rsub)	6.80e+0
Disk Inner Radius (AU)	7.21e-2	Disk Inner Radius (AU)	6.24e-1
Disk Scaleheight factor	0.829	Disk Scaleheight factor	0.886
Disk Flaring Power	1.103	Disk Flaring Power	1.002
Disk Accretion Alpha	1.60e-3	Disk Accretion Alpha	3.32e-2
Envelope Cavity density (cgs)	1.53e-21	Envelope Cavity density (cgs)	3.70e-21
Ambient density (cgs)	1.07e-22	Ambient density (cgs)	1.87e-22
Disk accretion rate (Msol/yr)	8.08e-9	Disk accretion rate (Msol/yr)	2.60e-7
A_v [circumstellar] (mag)	1.93e-2	A_v [circumstellar] (mag)	2.08e-1
Total Luminosity	1.22e+0	Total Luminosity	1.94e+0
Disk Scaleheight at 100AU	6.38	Disk Scaleheight at 100AU	3.14
Envelope Mass	5.08e-1	Envelope Mass	2.44e-4
Stellar Age (yr)	1.24e+6	Stellar Age (yr)	3.90e+5
Stellar Mass (Msol)	3.01	Stellar Mass (Msol)	0.46
Stellar Radius (Rsol)	4.76	Stellar Radius (Rsol)	3.40
Stellar Temperature (K)	5113	Stellar Temperature (K)	3698
Envelope Accretion Rate (Msol/yr)	0	Envelope Accretion Rate (Msol/yr)	8.77e-7
Envelope Outer Radius (AU)	-	Envelope Outer Radius (AU)	2.32e+3
Envelope Cavity Angle (degrees)	-	Envelope Cavity Angle (degrees)	20.6
Envelope Inner Radius (Rsub)	-	Envelope Inner Radius (Rsub)	1.00e+0
Disk Mass (Msol)	1.09e-1	Disk Mass (Msol)	2.02e-2
Disk Outer Radius (AU)	2.91e+2	Disk Outer Radius (AU)	6.19e+1
Disk Inner Radius (Rsub)	1.00e+0	Disk Inner Radius (Rsub)	1.00e+0
Disk Inner Radius (AU)	3.10e-1	Disk Inner Radius (AU)	9.25e-2
Disk Scaleheight factor	0.816	Disk Scaleheight factor	0.651
Disk Flaring Power	1.078	Disk Flaring Power	1.056
Disk Accretion Alpha	4.17e-2	Disk Accretion Alpha	1.70e-3
Envelope Cavity density (cgs)	-	Envelope Cavity density (cgs)	1.22e-21
Ambient density (cgs)	1.35e-21	Ambient density (cgs)	2.55e-22
Disk accretion rate (Msol/yr)	4.36e-7	Disk accretion rate (Msol/yr)	1.32e-8
A_v [circumstellar] (mag)	3.13e-2	A_v [circumstellar] (mag)	7.10e-1
Total Luminosity	2.12e+1	Total Luminosity	1.98e+0
Disk Scaleheight at 100AU	3.05	Disk Scaleheight at 100AU	3.48
Envelope Mass	2.54e-3	Envelope Mass	7.71e-3
Stellar Age (yr)	7.16e+6	Stellar Age (yr)	1.21e+5
Stellar Mass (Msol)	0.97	Stellar Mass (Msol)	0.55
Stellar Radius (Rsol)	1.28	Stellar Radius (Rsol)	4.15
Stellar Temperature (K)	4212	Stellar Temperature (K)	3826
Envelope Accretion Rate (Msol/yr)	0	Envelope Accretion Rate (Msol/yr)	4.43e-6
Envelope Outer Radius (AU)	-	Envelope Outer Radius (AU)	3.82e+3
Envelope Cavity Angle (degrees)	-	Envelope Cavity Angle (degrees)	36.2
Envelope Inner Radius (Rsub)	-	Envelope Inner Radius (Rsub)	1.00e+0
Disk Mass (Msol)	1.25e-2	Disk Mass (Msol)	3.08e-2
Disk Outer Radius (AU)	1.69e+2	Disk Outer Radius (AU)	1.59e+2
Disk Inner Radius (Rsub)	7.90e+1	Disk Inner Radius (Rsub)	1.00e+0
Disk Inner Radius (AU)	3.68e+0	Disk Inner Radius (AU)	1.21e-1
Disk Scaleheight factor	0.696	Disk Scaleheight factor	0.820
Disk Flaring Power	1.118	Disk Flaring Power	1.124
Disk Accretion Alpha	1.70e-3	Disk Accretion Alpha	2.00e-3
Envelope Cavity density (cgs)	-	Envelope Cavity density (cgs)	7.02e-21
Ambient density (cgs)	3.26e-22	Ambient density (cgs)	1.93e-22
Disk accretion rate (Msol/yr)	1.43e-9	Disk accretion rate (Msol/yr)	1.20e-8
A_v [circumstellar] (mag)	1.05e+4	A_v [circumstellar] (mag)	4.56e+0
Total Luminosity	4.88e-1	Total Luminosity	3.37e+0
Disk Scaleheight at 100AU	3.00	Disk Scaleheight at 100AU	7.12
Envelope Mass	1.11e-8	Envelope Mass	7.89e-2

Figure B.4: The best fit SED's associated parameters of the class II sources, from top DOAR25, DOAR44, EL24, EL27, Flying Saucer and GSS26. The units for each parameter are given in brackets, except envelope mass that is in M_{\odot} .

Envelope Accretion Rate (Msol/yr)	1.89e-6	Stellar Age (yr)	1.64e+5
Envelope Outer Radius (AU)	8.67e+3	Stellar Mass (Msol)	0.31
Envelope Cavity Angle (degrees)	52.2	Stellar Radius (Rsol)	2.80
Envelope Inner Radius (Rsub)	1.00e+0	Stellar Temperature (K)	3395
Disk Mass (Msol)	1.72e-2	Envelope Accretion Rate (Msol/yr)	9.26e-6
Disk Outer Radius (AU)	1.17e+2	Envelope Outer Radius (AU)	2.50e+3
Disk Inner Radius (Rsub)	1.00e+0	Envelope Cavity Angle (degrees)	27.4
Disk Inner Radius (AU)	2.13e-1	Envelope Inner Radius (Rsub)	3.12e+0
Disk Scaleheight factor	0.718	Disk Mass (Msol)	1.58e-3
Disk Flaring Power	1.161	Disk Outer Radius (AU)	6.66e+1
Disk Accretion Alpha	8.24e-2	Disk Inner Radius (Rsub)	3.12e+0
Envelope Cavity density (cgs)	3.34e-21	Disk Inner Radius (AU)	2.16e-1
Ambient density (cgs)	3.85e-22	Disk Scaleheight factor	0.978
Disk accretion rate (Msol/yr)	1.83e-7	Disk Flaring Power	1.159
A_v [circumstellar] (mag)	1.04e-1	Disk Accretion Alpha	8.00e-2
Total Luminosity	1.02e+1	Envelope Cavity density (cgs)	3.32e-21
Disk Scaleheight at 100AU	4.95	Ambient density (cgs)	1.75e-22
Envelope Mass	4.43e-2	Disk accretion rate (Msol/yr)	8.87e-8
		A_v [circumstellar] (mag)	2.50e+0
		Total Luminosity	1.13e+0
		Disk Scaleheight at 100AU	11.48
		Envelope Mass	1.32e-1
Stellar Age (yr)	6.50e+5	Stellar Age (yr)	7.41e+4
Stellar Mass (Msol)	1.25	Stellar Mass (Msol)	0.12
Stellar Radius (Rsol)	3.47	Stellar Radius (Rsol)	2.50
Stellar Temperature (K)	4399	Stellar Temperature (K)	2833
Envelope Accretion Rate (Msol/yr)	8.64e-8	Envelope Accretion Rate (Msol/yr)	3.00e-5
Envelope Outer Radius (AU)	2.32e+3	Envelope Outer Radius (AU)	1.29e+3
Envelope Cavity Angle (degrees)	33.9	Envelope Cavity Angle (degrees)	31.2
Envelope Inner Radius (Rsub)	1.00e+0	Envelope Inner Radius (Rsub)	1.00e+0
Disk Mass (Msol)	2.49e-2	Disk Mass (Msol)	2.35e-3
Disk Outer Radius (AU)	9.16e+1	Disk Outer Radius (AU)	4.70e+1
Disk Inner Radius (Rsub)	1.00e+0	Disk Inner Radius (Rsub)	1.00e+0
Disk Inner Radius (AU)	1.50e-1	Disk Inner Radius (AU)	3.98e-2
Disk Scaleheight factor	0.832	Disk Scaleheight factor	0.956
Disk Flaring Power	1.056	Disk Flaring Power	1.030
Disk Accretion Alpha	1.24e-2	Disk Accretion Alpha	8.70e-3
Envelope Cavity density (cgs)	2.03e-21	Envelope Cavity density (cgs)	1.90e-20
Ambient density (cgs)	2.71e-22	Ambient density (cgs)	1.00e-22
Disk accretion rate (Msol/yr)	1.09e-7	Disk accretion rate (Msol/yr)	2.43e-8
A_v [circumstellar] (mag)	1.69e-2	A_v [circumstellar] (mag)	8.81e-2
Total Luminosity	5.12e+0	Total Luminosity	3.96e-1
Disk Scaleheight at 100AU	3.19	Disk Scaleheight at 100AU	5.56
Envelope Mass	5.43e-4	Envelope Mass	2.45e-1

Figure B.5: The best fit SED's associated parameters of the class II sources, from top SR21, SR4, WAOph6 and YLW58. The units for each parameter are given in brackets, except envelope mass that is in M_{\odot} .

Source Name	U Band Flux	B Band Flux ²	V Band Flux	R Band Flux ²	I Band Flux ²	J Band Flux ⁶	H Band Flux ⁶	K Band Flux ⁶
AS205	6.09 ¹	13.2 ¹	29.8 ¹	55 ¹	163 ¹	955	2050	3240
DoAr25	...	1.34	...	12.5	124	279	448	484
DoAr44	...	10.4	...	29.4	157	323	515	602
EL24	...	0.03	...	0.47	8.18	160	594	1410
EL27	8	58.7	175
Flying Saucer	...	0.06	...	0.24	0.27	0.9	1.66	1.97
GSS26	2.85	46.8	272
SR21	...	3.77	...	38.8	122	506	1020	1370
SR4	2.84 ³	6.55	28.7 ⁴	32.2	149	347	565	656
WaOph6	0.92 ¹	3.98 ¹	19.5 ⁵	45.8 ⁵	127 ⁵	521	1010	1200
YLW58	...	0.02	...	0.37	4.21	47.8	94.8	125

Table B.8: Table containing the literature data for the observations at $\leq 2.2 \mu\text{m}$ used to build the SEDs for the Class II objects. Fluxes are quoted in mJy. 1: Eisner et al. (2005) 2: USNO 3: Chini (1981) 4: Herbst et al. (1994) 5: Padgett et al. (2006) 6: Skrutskie et al. (2006)

Source Name	3.6 μm Flux ¹	4.5 μm Flux ¹	5.8 μm Flux ¹	6.7 μm Flux ²	8.0 μm Flux ¹	10 μm Flux ³	12 μm Flux ⁴	14.3 μm Flux ²
AS205	4560	8200	10700	11400	...
DoAr25	367	292	299	174	258	260	914	206
DoAr44	620	540	489	...	673	...	981	...
EL24	2220	2330	2700	2730	3140	2570	3440	3020
EL27	289	372	374	291	381	320	...	307
Flying Saucer	2.32	2.0	1.39	...	0.82
GSS26	286	386	509	386	617	1010	...	430
SR21	1300	1170	1280	1570	1660	1730	2270	2840
SR4	600	534	466	400	577	...	7380	662
WaOph6	1018	924	871	...	814	861	1410	...
YLW58	111	104	95.4	108	105	...	120	128

Table B.9: Table containing the literature data for the observations between 3.6 μm and 14.3 μm used to build the SEDs for the Class II objects. Fluxes are quoted in mJy. 1: Spitzer IRAC data from IRSA 2: Bontemps et al. (2001) 3: Barsony et al. (2005) 4: Beichman et al. (1988)

Source Name	24 μm Flux ¹	25 μm Flux ²	60 μm Flux ²	70 μm Flux ¹	100 μm Flux ²	350 μm Flux ³	450 μm Flux ³	800 μm Flux	850 μm Flux ³	1.1 mm Flux	1.2 mm Flux ⁶	1.3 mm Flux ⁷
AS205	...	13850	19160	...	16070	4683	3280	998 ⁴	891	503 ⁴	...	279
DoAr25	399	1480	8240	1100	1900	450 ⁵	461	...	153	280
DoAr44	1690	2310	...	2560	181	105
EL24	2920	3800	...	4230	...	5242	3012	...	838	...	242	...
EL27	501	2737	...	678	...	291	300
Flying Saucer	1.58
GSS26	7.98	650	...	298	...	84	125
SR4	...	19810	33800	16600	...	2761	1896	...	397	...	69	150
SR21	2190	9620	142	...	102	...
WaOph6	1054	1900	...	989	6470	...	979	...	337	130
YLW58	229	220	4000	626	54000	832	651	...	149	89

Table B.10: Table containing the literature data for the observations at $\geq 24 \mu\text{m}$ used to build the SEDs for the Class II objects. Fluxes are quoted in mJy. 1: Spitzer MIPS data from IRSA 2: Beichman et al. (1988) 3: Andrews & Williams (2007a) 4: Jensen et al. (1996) 5: Dent et al. (1998) 6: Stanke et al. (2006) 7: Andre & Montmerle (1994)

B.6 Class III

Stellar Age (yr)	9.00e+6	Stellar Age (yr)	4.41e+5
Stellar Mass (Msol)	0.87	Stellar Mass (Msol)	0.56
Stellar Radius (Rsol)	1.13	Stellar Radius (Rsol)	3.66
Stellar Temperature (K)	4121	Stellar Temperature (K)	3845
Envelope Accretion Rate (Msol/yr)	0	Envelope Accretion Rate (Msol/yr)	1.28e-7
Envelope Outer Radius (AU)	-	Envelope Outer Radius (AU)	5.50e+3
Envelope Cavity Angle (degrees)	-	Envelope Cavity Angle (degrees)	24.0
Envelope Inner Radius (Rsub)	-	Envelope Inner Radius (Rsub)	1.50e+2
Disk Mass (Msol)	1.29e-8	Disk Mass (Msol)	1.24e-5
Disk Outer Radius (AU)	5.16e+2	Disk Outer Radius (AU)	2.74e+2
Disk Inner Radius (Rsub)	2.58e+3	Disk Inner Radius (Rsub)	1.50e+2
Disk Inner Radius (AU)	9.85e+1	Disk Inner Radius (AU)	1.61e+1
Disk Scaleheight factor	0.653	Disk Scaleheight factor	0.614
Disk Flaring Power	1.143	Disk Flaring Power	1.091
Disk Accretion Alpha	8.10e-3	Disk Accretion Alpha	1.80e-3
Envelope Cavity density (cgs)	-	Envelope Cavity density (cgs)	1.88e-21
Ambient density (cgs)	2.41e-22	Ambient density (cgs)	1.30e-22
Disk accretion rate (Msol/yr)	2.10e-15	Disk accretion rate (Msol/yr)	1.59e-12
A_v [circumstellar] (mag)	3.62e-4	A_v [circumstellar] (mag)	5.12e+0
Total Luminosity	3.29e-1	Total Luminosity	2.63e+0
Disk Scaleheight at 100AU	3.41	Disk Scaleheight at 100AU	4.05
Envelope Mass	2.32e-7	Envelope Mass	4.97e-3
Stellar Age (yr)	9.79e+8	Stellar Age (yr)	8.06e+5
Stellar Mass (Msol)	1.97	Stellar Mass (Msol)	0.14
Stellar Radius (Rsol)	1.76	Stellar Radius (Rsol)	1.47
Stellar Temperature (K)	8673	Stellar Temperature (K)	2991
Envelope Accretion Rate (Msol/yr)	0	Envelope Accretion Rate (Msol/yr)	1.24e-9
Envelope Outer Radius (AU)	-	Envelope Outer Radius (AU)	1.21e+3
Envelope Cavity Angle (degrees)	-	Envelope Cavity Angle (degrees)	58.9
Envelope Inner Radius (Rsub)	-	Envelope Inner Radius (Rsub)	1.00e+0
Disk Mass (Msol)	2.48e-8	Disk Mass (Msol)	1.10e-3
Disk Outer Radius (AU)	9.91e+1	Disk Outer Radius (AU)	7.91e+1
Disk Inner Radius (Rsub)	1.68e+2	Disk Inner Radius (Rsub)	1.00e+0
Disk Inner Radius (AU)	4.76e+1	Disk Inner Radius (AU)	2.94e-2
Disk Scaleheight factor	0.704	Disk Scaleheight factor	0.966
Disk Flaring Power	1.148	Disk Flaring Power	1.058
Disk Accretion Alpha	8.48e-2	Disk Accretion Alpha	4.48e-2
Envelope Cavity density (cgs)	-	Envelope Cavity density (cgs)	3.99e-22
Ambient density (cgs)	7.76e-22	Ambient density (cgs)	1.00e-22
Disk accretion rate (Msol/yr)	9.83e-13	Disk accretion rate (Msol/yr)	2.58e-8
A_v [circumstellar] (mag)	2.15e-4	A_v [circumstellar] (mag)	1.74e-3
Total Luminosity	1.57e+1	Total Luminosity	2.26e-1
Disk Scaleheight at 100AU	5.14	Disk Scaleheight at 100AU	5.42
Envelope Mass	1.01e-8	Envelope Mass	7.23e-6

Figure B.6: The best fit SED's associated parameters of the class III sources, from top left GY10, GY12, GY306 and ISO-Oph 26. GY29 is not included as none of the models fitted the data. The units for each parameter are given in brackets, except envelope mass that is in M_{\odot} .

Source Name	R Band Flux ¹	I Band Flux ¹	J Band Flux ²	H Band Flux ²	K Band Flux ²	3.6 μ m Flux ³	4.5 μ m Flux ³	5.8 μ m Flux ³	6.7 μ m Flux ⁴	8.0 μ m Flux ³	14.3 μ m Flux ⁴	24 μ m Flux ⁵
GY10	0.0003	0.004	0.77	4.3	8.47	9.4	11.4	6.12	8.9	3.72
GY12	3.29	27.8	96.4	98.8	72.9	83.9	52	...	84	508
GY29	0.49	5.88	24.8	46.3	47.6	49	...
GY306	15.5	45.2	71.8	72	53.8	43.3	...	13.5
ISO-Oph 26	0.558	3.24	11.2	25.2	41.7	53.3	...	67.4	74	89.7

Table B.11: Table containing the literature data used to build the SEDs for the Class III objects. Fluxes are quoted in mJy. 1: Comeron et al. (1998) 2: Skrutskie et al. (2006) 3: Spitzer IRAC data from IRSA 4: Bontemps et al. (2001) 5: Spitzer MIPS data from IRSA

Bibliography

- Abergel, A., Teyssier, D., Bernard, J. P., et al. 2003, *A&A*, 410, 577
- Adams, F. C., Hollenbach, D., Laughlin, G., & Gorti, U. 2004, *ApJ*, 611, 360
- Adams, F. C., Shu, F. H., & Lada, C. J. 1988, *ApJ*, 326, 865
- Akabane, K. 1983, *International Journal of Infrared and Millimeter Waves*, 4, 793
- Alves de Oliveira, C. & Casali, M. 2008, *A&A*, 485, 155
- Anathpindika, S. & Whitworth, A. P. 2008, *A&A*, 487, 605
- Andre, P. & Montmerle, T. 1994, *ApJ*, 420, 837
- Andre, P., Ward-Thompson, D., & Barsony, M. 1993, *ApJ*, 406, 122
- Andrews, S. M., Hughes, A. M., Wilner, D. J., & Qi, C. 2008, *ApJL*, 678, L133
- Andrews, S. M. & Williams, J. P. 2005, *ApJ*, 631, 1134
- Andrews, S. M. & Williams, J. P. 2007a, *ApJ*, 671, 1800
- Andrews, S. M. & Williams, J. P. 2007b, *ApJ*, 659, 705
- Artymowicz, P. & Lubow, S. H. 1994, *ApJ*, 421, 651
- Balbus, S. A. & Cowie, L. L. 1985, *ApJ*, 297, 61
- Ballesteros-Paredes, J., Hartmann, L., & Vázquez-Semadeni, E. 1999, *ApJ*, 527, 285
- Barsony, M., Greene, T. P., & Blake, G. A. 2002, *ApJL*, 572, L75
- Barsony, M., Ressler, M. E., & Marsh, K. A. 2005, *ApJ*, 630, 381
- Bate, M. R., Bonnell, I. A., & Bromm, V. 2002, *MNRAS*, 332, L65
- Beckwith, S. V. W. & Sargent, A. I. 1991, *ApJ*, 381, 250
- Beckwith, S. V. W., Sargent, A. I., Chini, R. S., & Guesten, R. 1990, *AJ*, 99, 924
- Beichman, C. A., Neugebauer, G., Habing, H. J., Clegg, P. E., & Chester, T. J., eds. 1988, *Infrared astronomical satellite (IRAS) catalogs and atlases. Volume 1: Explanatory supplement, Vol. 1*

- Beichmann, C. A. 1985, Infrared Astronomical Satellite (IRAS) catalogs and atlases. Explanatory supplement (Pasadena: Jet Propulsion Laboratory, 1985, edited by Beichmann, C.A.)
- Bontemps, S., André, P., Kaas, A. A., et al. 2001, *A&A*, 372, 173
- Boss, A. P. 1989, *ApJ*, 346, 336
- Boss, A. P. 1997, *Science*, 276, 1836
- Boss, A. P. 2000, *ApJL*, 536, L101
- Bottinelli, S., Ceccarelli, C., Neri, R., et al. 2004, *ApJL*, 617, L69
- Bouvier, J., Covino, E., Kovo, O., et al. 1995, *A&A*, 299, 89
- Burgasser, A. J. 2007, *ApJ*, 659, 655
- Burke, B. F. & Graham-Smith, F. 2002, *An Introduction to Radio Astronomy: Second Edition (Infrared Astronomy)*
- Carilli, C. L., Carlstrom, J. E., & Holdaway, M. A. 1999, in *Astronomical Society of the Pacific Conference Series*, Vol. 180, *Synthesis Imaging in Radio Astronomy II*, ed. G. B. Taylor, C. L. Carilli, & R. A. Perley, 565–+
- Cazes, Jr., J. E. 1999, PhD thesis, AA(THE LOUISIANA STATE UNIVERSITY AND AGRICULTURAL AND MECHANICAL COL.)
- Chen, X. P., Launhardt, R., & Henning, T. 2007, *A&A*, 475, 277
- Chini, R. 1981, *A&A*, 99, 346
- Christiansen, W. N. & Hogbom, J. A. 1985, *Radiotelescopes /2nd edition/* (Cambridge and New York, Cambridge University Press, 1985, 273 p.)
- Clarke, C. 1992, *Nature*, 357, 197
- Clarke, C. J. 1996, in *Astronomical Society of the Pacific Conference Series*, Vol. 90, *The Origins, Evolution, and Destinies of Binary Stars in Clusters*, ed. E. F. Milone & J.-C. Mermilliod, 242–+
- Cohen, M. & Kuhl, L. V. 1979, *ApJS*, 41, 743
- Comeron, F., Rieke, G. H., Claes, P., Torra, J., & Laureijs, R. J. 1998, *A&A*, 335, 522
- Correia, J. C., Griffin, M., & Saraceno, P. 2004, *A&A*, 418, 607
- Correia, S., Zinnecker, H., Ratzka, T., & Sterzik, M. F. 2006, *A&A*, 459, 909
- Covey, K. R., Greene, T. P., Doppmann, G. W., & Lada, C. J. 2006, *AJ*, 131, 512

- Covino, E., Alcalá, J. M., Allain, S., et al. 1997, *A&A*, 328, 187
- Cutri, R. M., Skrutskie, M. F., van Dyk, S., et al. 2003, 2MASS All Sky Catalog of point sources. (The IRSA 2MASS All-Sky Point Source Catalog, NASA/IPAC Infrared Science Archive. <http://irsa.ipac.caltech.edu/applications/Gator/>)
- de Geus, E. J., de Zeeuw, P. T., & Lub, J. 1989, *A&A*, 216, 44
- Dent, W. R. F., Matthews, H. E., & Walther, D. M. 1995, *MNRAS*, 277, 193
- Dent, W. R. F., Matthews, H. E., & Ward-Thompson, D. 1998, *MNRAS*, 301, 1049
- Dobbs, C. L., Bonnell, I. A., & Pringle, J. E. 2006, *MNRAS*, 371, 1663
- Dowell, C. D., Allen, C. A., Babu, R. S., et al. 2003, in Society of Photo-Optical Instrumentation Engineers (SPIE) Conference Series, Vol. 4855, Society of Photo-Optical Instrumentation Engineers (SPIE) Conference Series, ed. T. G. Phillips & J. Zmuidzinas, 73–87
- Draine, B. T. & Lee, H. M. 1984, *ApJ*, 285, 89
- Duchêne, G., Bontemps, S., Bouvier, J., et al. 2007, *A&A*, 476, 229
- Duchêne, G., Bouvier, J., Bontemps, S., André, P., & Motte, F. 2004, *A&A*, 427, 651
- Dullemond, C. P., Dominik, C., & Natta, A. 2001, *ApJ*, 560, 957
- Duquennoy, A. & Mayor, M. 1991, *A&A*, 248, 485
- Eisner, J. A., Hillenbrand, L. A., White, R. J., Akeson, R. L., & Sargent, A. I. 2005, *ApJ*, 623, 952
- Elmegreen, B. G. 2000, *ApJ*, 530, 277
- Estalella, R., Anglada, G., Rodríguez, L. F., & Garay, G. 1991, *ApJ*, 371, 626
- Feigelson, E. D. & Montmerle, T. 1999, *ARA&A*, 37, 363
- Feigelson, E. D. & Nelson, P. I. 1985, *ApJ*, 293, 192
- Field, G. B. & Saslaw, W. C. 1965, *ApJ*, 142, 568
- Fischer, D. A. & Marcy, G. W. 1992, *ApJ*, 396, 178
- Gagné, M., Skinner, S. L., & Daniel, K. J. 2004, *ApJ*, 613, 393
- Gammie, C. F. 2001, *ApJ*, 553, 174
- Genzel, R. & Stutzki, J. 1989, *ARA&A*, 27, 41
- Georgelin, Y. M. & Georgelin, Y. P. 1976, *A&A*, 49, 57

- Ghez, A. M., Neugebauer, G., & Matthews, K. 1993, *AJ*, 106, 2005
- Girart, J. M., Rodríguez, L. F., & Curiel, S. 2000, *ApJL*, 544, L153
- Glass, I. S. 1999, *Handbook of Infrared Astronomy* (Highlights of Astronomy)
- Goodman, A. A., Benson, P. J., Fuller, G. A., & Myers, P. C. 1993, *ApJ*, 406, 528
- Gras-Velázquez, À. & Ray, T. P. 2005, *A&A*, 443, 541
- Grosso, N., Alves, J., Wood, K., et al. 2003, *ApJ*, 586, 296
- Guenther, E. W., Esposito, M., Mundt, R., et al. 2007, *A&A*, 467, 1147
- Gullbring, E., Hartmann, L., Briceno, C., & Calvet, N. 1998, *ApJ*, 492, 323
- Haisch, Jr., K. E., Barsony, M., Greene, T. P., & Ressler, M. E. 2002, *AJ*, 124, 2841
- Haisch, Jr., K. E., Barsony, M., Ressler, M. E., & Greene, T. P. 2006, *AJ*, 132, 2675
- Hayashi, C. 1966, *ARA&A*, 4, 171
- Herbig, G. H. 1978, *Can Post-T Tauri Stars Be Found? (Problems of Physics and Evolution of the Universe)*, 171–+
- Herbig, G. H. & Bell, K. R. 1988, *Catalog of emission line stars of the orion population : 3 : 1988* (Lick Observatory Bulletin, Santa Cruz: Lick Observatory, —c1988)
- Herbst, W., Herbst, D. K., Grossman, E. J., & Weinstein, D. 1994, *AJ*, 108, 1906
- Hildebrand, R. H. 1983, *QJRAS*, 24, 267
- Hillenbrand, L. A. 2005, *ArXiv Astrophysics e-prints*
- Hills, J. G. 1976, *MNRAS*, 175, 1P
- Högbom, J. A. 1974, *A&AS*, 15, 417
- Hollenbach, D. & Gorti, U. 2005, in *Protostars and Planets V*, 8433–+
- Ichikawa, T. & Nishida, M. 1989, *AJ*, 97, 1074
- Jensen, E. L. N., Dhital, S., Stassun, K. G., et al. 2007, *AJ*, 134, 241
- Jensen, E. L. N. & Mathieu, R. D. 1997, *AJ*, 114, 301
- Jensen, E. L. N., Mathieu, R. D., & Fuller, G. A. 1996, *ApJ*, 458, 312
- Johansen, A., Oishi, J. S., Low, M.-M. M., et al. 2007, *Nature*, 448, 1022
- Johnstone, D., Wilson, C. D., Moriarty-Schieven, G., et al. 2000, *ApJ*, 545, 327
- Jørgensen, J. K., Johnstone, D., Kirk, H., et al. 2008, *ApJ*, 683, 822

- Joy, A. H. 1945, *ApJ*, 102, 168
- Kazes, I., Crutcher, R. M., & Troland, T. H. 1987, in *IAU Symposium*, Vol. 115, *Star Forming Regions*, ed. M. Peimbert & J. Jugaku, 55–+
- Lada, C. J. 1987, in *IAU Symposium*, Vol. 115, *Star Forming Regions*, ed. M. Peimbert & J. Jugaku, 1–17
- Lada, C. J., Margulis, M., Sofue, Y., Nakai, N., & Handa, T. 1988, *ApJ*, 328, 143
- Lada, C. J. & Wilking, B. A. 1984, *ApJ*, 287, 610
- Larson, R. B. 1981, *MNRAS*, 194, 809
- Lay, O. P., Carlstrom, J. E., Hills, R. E., & Phillips, T. G. 1994, *ApJL*, 434, L75
- Lebovitz, N. R. 1974, *ApJ*, 190, 121
- Lee, C. W., Myers, P. C., & Tafalla, M. 2001, *ApJS*, 136, 703
- Leong, M., Peng, R., Houde, M., et al. 2006, in *Society of Photo-Optical Instrumentation Engineers (SPIE) Conference Series*, Vol. 6275, *Society of Photo-Optical Instrumentation Engineers (SPIE) Conference Series*
- Leous, J. A., Feigelson, E. D., Andre, P., & Montmerle, T. 1991, *ApJ*, 379, 683
- Liu, M. C., Leggett, S. K., Golimowski, D. A., et al. 2006, *ApJ*, 647, 1393
- Loinard, L. 2002, *Revista Mexicana de Astronomia y Astrofisica*, 38, 61
- Looney, L. W., Mundy, L. G., & Welch, W. J. 2000, *ApJ*, 529, 477
- Loren, R. B. 1989, *ApJ*, 338, 902
- Luhman, K. L. & Rieke, G. H. 1999, *ApJ*, 525, 440
- Lyttleton, R. A. 1953, *The comets and their origin* (Cambridge: University Press, —c1953)
- Mamajek, E. E. 2008, *Astronomische Nachrichten*, 329, 10
- Martín, E. L. 1997, *Memorie della Societa Astronomica Italiana*, 68, 905
- Mathieu, R. D., Myers, P. C., Schild, R. E., Benson, P. J., & Fuller, G. A. 1988, *ApJ*, 330, 385
- Mathis, J. S., Rumpl, W., & Nordsieck, K. H. 1977, *ApJ*, 217, 425
- McCaughrean, M. J. & O'Dell, C. R. 1996, *AJ*, 111, 1977
- McDonald, J. M. & Clarke, C. J. 1993, *MNRAS*, 262, 800
- Melo, C. H. F. 2003, *A&A*, 410, 269

- Michelson, A. A. 1920, *ApJ*, 51, 257
- Miyake, K. & Nakagawa, Y. 1993, *Icarus*, 106, 20
- Montmerle, T., Koch-Miramond, L., Falgarone, E., & Grindlay, J. E. 1983, *ApJ*, 269, 182
- Motte, F., Andre, P., & Neri, R. 1998, *A&A*, 336, 150
- Mouschovias, T. C. 1991, in *NATO ASIC Proc. 342: The Physics of Star Formation and Early Stellar Evolution*, ed. C. J. Lada & N. D. Kylafis, 449–+
- Napier, P. J. 1999, in *Astronomical Society of the Pacific Conference Series*, Vol. 180, *Synthesis Imaging in Radio Astronomy II*, ed. G. B. Taylor, C. L. Carilli, & R. A. Perley, 37–+
- Natta, A., Testi, L., & Randich, S. 2006, *A&A*, 452, 245
- Neuhäuser, R. 1997, *Science*, 276, 1363
- Nutter, D., Ward-Thompson, D., & André, P. 2006, *MNRAS*, 368, 1833
- Padgett, D. L., Cieza, L., Stapelfeldt, K. R., et al. 2006, *ApJ*, 645, 1283
- Papaloizou, J. & Pringle, J. E. 1977, *MNRAS*, 181, 441
- Patience, J., Akeson, R. L., & Jensen, E. L. N. 2008, *ApJ*, 677, 616
- Pollack, J. B., Hubickyj, O., Bodenheimer, P., et al. 1996, *Icarus*, 124, 62
- Portegies Zwart, S. F., Hut, P., & Verbunt, F. 1997, *A&A*, 328, 130
- Prato, L., Greene, T. P., & Simon, M. 2003, *ApJ*, 584, 853
- Pringle, J. E. 1989, *MNRAS*, 239, 361
- Reipurth, B. & Zinnecker, H. 1993, *A&A*, 278, 81
- Ressler, M. E. & Barsony, M. 2001, *AJ*, 121, 1098
- Ridge, N. A., Di Francesco, J., Kirk, H., et al. 2006, *AJ*, 131, 2921
- Robitaille, T. P., Whitney, B. A., Indebetouw, R., & Wood, K. 2007, *ApJS*, 169, 328
- Robitaille, T. P., Whitney, B. A., Indebetouw, R., Wood, K., & Denzmore, P. 2006, *ApJS*, 167, 256
- Safronov, V. S. 1966, *Soviet Astronomy*, 9, 987
- Safronov, V. S. 1969, *Evoliutsiia doplanetnogo oblaka*. (1969.)
- Sault, R. J., Teuben, P. J., & Wright, M. C. H. 1995, in *Astronomical Society of the Pacific Conference Series*, Vol. 77, *Astronomical Data Analysis Software and Systems IV*, ed. R. A. Shaw, H. E. Payne, & J. J. E. Hayes, 433–+

- Scalo, J. M. 1986, *Fundamentals of Cosmic Physics*, 11, 1
- Schaller, G., Schaerer, D., Meynet, G., & Maeder, A. 1992, *A&AS*, 96, 269
- Shu, F. H. 1977, *ApJ*, 214, 488
- Shu, F. H., Adams, F. C., & Lizano, S. 1987, *ARA&A*, 25, 23
- Skrutskie, M. F., Cutri, R. M., Stiening, R., et al. 2006, *AJ*, 131, 1163
- Snell, R. L., Loren, R. B., & Plambeck, R. L. 1980, *ApJL*, 239, L17
- Stanke, T., Smith, M. D., Gredel, R., & Khanzadyan, T. 2006, *A&A*, 447, 609
- Takeuchi, T., Clarke, C. J., & Lin, D. N. C. 2005, *ApJ*, 627, 286
- Terebey, S., Shu, F. H., & Cassen, P. 1984, *ApJ*, 286, 529
- Thompson, A. R. 1999, in *Astronomical Society of the Pacific Conference Series*, Vol. 180, *Synthesis Imaging in Radio Astronomy II*, ed. G. B. Taylor, C. L. Carilli, & R. A. Perley, 11–+
- Tsuribe, T. & Inutsuka, S.-I. 1999, *ApJ*, 526, 307
- Weidenschilling, S. J. 1977, *Ap&SS*, 51, 153
- Whitworth, A. P. & Zinnecker, H. 2004, *A&A*, 427, 299
- Wilking, B. A., Meyer, M. R., Robinson, J. G., & Greene, T. P. 2005, *AJ*, 130, 1733
- Wootten, A. 1989, *ApJ*, 337, 858
- Young, K. E., Enoch, M. L., Evans, II, N. J., et al. 2006, *ApJ*, 644, 326